Technische Universität München
TUM School of Computation, Information and Technology

Studying The Effects of Acoustic Heterogeneities on Optoacoustic Tomography

Marwan Muhammad

Vollständiger Abdruck der von der TUM School of Computation, Information and Technology der Technischen Universität München zur Erlangung eines Doktors der Ingenieurwissenschaften (Dr. -Ing) genchmigten Dissertation.

Vorsitz: Prof. Dr. Bernhard Wolfrum

Prüfer der Dissertation:

1. Prof. Dr. Vasilis Ntziachristos
2. Prof. Dr.-Ing. Werner Hemmert
3. Prof. Dr. Björn Menze

Die Dissertation wurde am 21.02.2023 bei der Technischen Universität München eingereicht und durch die TUM School of Computation, Information and Technology am 25.01.2024 angenommen.

Dedication

To my parents...

ABSTRACT

Recent advances in imaging methodologies have facilitated novel discoveries in biological and clinical research. Each imaging methodology utilizes certain physical and biological aspects of the tissue under investigation to provide specific information with a certain contrast over a wide scale of spatial resolutions. Thus, each has its own advantages and limitations.

A novel modality that emerged in the last decade is optoacoustic (OA) (photoacoustic) imaging, which combines versatile optical absorption contrast with high ultrasonic resolution and real-time imaging capabilities by capitalizing on the OA effect. Using illumination with multiple wavelengths and spectral unmixing methods, multispectral OA tomography (MSOT) has the potential to specifically resolve tissue chromophores or administered extrinsic molecular agents noninvasively in deep tissue with unprecedented resolution performance and in real-time.

Most OA reconstruction algorithms assume that the sample under investigation is acoustically homogeneous and perfectly matched to the coupling medium between the sample and the acoustic detectors. However, in *in vivo* imaging cases, the propagation of OA waves is distorted due to acoustic heterogeneities inside the imaged sample. For example, lungs, bones and other tissues with high acoustic mismatch to surrounding tissues can induce strong acoustic reflections, scattering or speed-of-sound variation artefacts in reconstructed OA images, reducing the overall image fidelity. Acoustic heterogeneities can also contribute to the appearance of artefactual

negative values in the reconstructed images with adverse effects on spectral unmixing and functional OA imaging.

In this thesis, we first discuss a couple of conventional imaging modalities. Then, we specifically overview OA techniques and applications. The physical and some technical hardware aspects for OA imaging are then presented. Afterwards, algorithmic & technical aspects of OA image reconstruction and formation are discussed. Building on such overview of the physics and technical aspects underlying general OA imaging, we then start to focus on the effects of the presence of acoustic heterogeneities in the imaged sample on the generated OA image and how to address such effects. In particular, a statistical weighted reconstruction approach was previously introduced by colleagues of our research group in order to mitigate such artefacts. However, this approach does not reliably provide high-quality reconstructions for partial-view (PV) imaging systems, which are common in preclinical and clinical optoacoustics. We overview the general concept underlying the statistical weighting in both backprojection (BP) and model-based (MB) reconstruction approaches, then we show how to extend the capability of the weighted MB algorithm to generate OA reconstructions with less distortions for PV geometry data. Afterwards, we validate the enhanced performance of the proposed PV correction on phantom and *in vivo* small-animal tomography data.

Due to its enhanced performance, the proposed partial-view-corrected weighted MB (PVc-wMB) algorithm should prove useful for improving the quality of PV MSOT, leading to enhanced visualization of functional parameters such as tissue oxygenation.

ABSTRAKT

Die letzten Fortschritte bei den Bildgebungsverfahren haben neue Entdeckungen in der biologischen und klinischen Forschung ermöglicht. Jede Bildgebungsmethode nutzt bestimmte physikalische und biologische Aspekte des untersuchten Gewebes, um spezifische Informationen mit einem bestimmten Kontrast über eine breite Skala räumlicher Auflösungen zu liefern. Somit hat jede Methode ihre eigenen Vorteile und Grenzen.

Eine neuartige Modalität, die in den letzten zehn Jahren entstanden ist, ist die optoakustische (OA) (photoakustische) Bildgebung, die einen vielseitigen optischen Absorptionskontrast mit einer hohen Ultraschallauflösung und Echtzeit-Bildgebungsmöglichkeiten kombiniert, indem sie den OA-Effekt nutzt. Die multispektrale optoakustische Tomographie (MSOT), bei der Beleuchtungen mit mehreren Wellenlängen und spektrale Unmixing-Methoden zum Einsatz kommen, hat das Potenzial, Gewebechromophore oder verabreichte extrinsische molekulare Wirkstoffe nichtinvasiv in tiefem Gewebe mit bisher unerreichter Auflösungsleistung und in Echtzeit aufzulösen.

Die meisten OA-Rekonstruktionsalgorithmen gehen davon aus, dass die zu untersuchende Probe akustisch homogen und perfekt an das Kopplungsmedium zwischen der Probe und den akustischen Detektoren angepasst ist. Bei der In-vivo-Bildgebung wird die Ausbreitung der OA-Wellen jedoch durch akustische Heterogenitäten innerhalb der abgebildeten Probe verzerrt. So können beispielsweise Lungen, Knochen und andere Gewebe mit einer starken akustischen Fehlanpassung an das umgebende Gewebe starke akustische Reflexionen, Streuungen oder Artefakte aufgrund

von Schallgeschwindigkeitsschwankungen in den rekonstruierten OA-Bildern hervorrufen, was die Bildtreue insgesamt verringert. Akustische Heterogenitäten können auch zum Auftreten artefaktischer negativer Werte in den rekonstruierten Bildern beitragen, was sich nachteilig auf das spektrale Unmixing und die funktionelle OA-Bildgebung auswirkt.

In dieser Arbeit werden zunächst einige konventionelle Bildgebungsmodalitäten diskutiert. Dann geben wir einen Überblick über die Techniken und Anwendungen der OA. Dann werden die physikalischen und einige technische Hardware-Aspekte für die OA-Bildgebung vorgestellt. Anschließend werden die algorithmischen und technischen Aspekte der Rekonstruktion und Erzeugung von OA-Bildern diskutiert. Aufbauend auf diesem Überblick über die physikalischen und technischen Aspekte, die der allgemeinen OA-Bildgebung zugrunde liegen, konzentrieren wir uns dann auf die Auswirkungen des Vorhandenseins akustischer Heterogenitäten in der abgebildeten Probe auf das erzeugte OA-Bild und auf die Frage, wie man mit solchen Effekten umgehen kann. Insbesondere ein statistisch gewichteter Rekonstruktionsansatz wurde zuvor von Kollegen unserer Forschungsgruppe eingeführt, um solche Artefakte abzuschwächen. Dieser Ansatz liefert jedoch keine zuverlässigen Rekonstruktionen von hoher Qualität für Bildgebungssysteme mit Teilansicht, wie sie in der präklinischen und klinischen Optoakustik üblich sind. Wir geben einen Überblick über das allgemeine Konzept, das der statistischen Gewichtung sowohl in der Rückprojektion als auch in den modellbasierten Rekonstruktionsansätzen zugrunde liegt. Anschließend validieren wir die verbesserte Leistung der vorgeschlagenen Teilansicht-Korrektur an Phantom- und In-vivo-Kleintier-Tomographiedaten.

Aufgrund seiner verbesserten Leistung sollte sich der vorgeschlagene Algorithmus mit gewichteter Teilansichtskorrektur als nützlich erweisen, um die Qualität von Teilansicht-MSOT zu verbessern, was zu einer verbesserten Visualisierung von funktionellen Parametern wie der Gewebeoxygenierung führt.

ACKNOWLEDGEMENT

Last but not least, I would like to express my deepest thanks & utmost gratitude to my parents, my sister, and the rest of my family & friends in Germany & my home country—Egypt—for always being supportive for my career and for their unconditional love. Research is a collaborative, but also very solitary, environment, which makes such support invaluable.

LIST OF ABBREVIATIONS

AF750	Alexa Fluor 750
BP	Backprojection algorithm
CT	Computed tomography
DOT	Diffuse optical tomography
EFR	Electrical frequency response
EIR	Electrical impulse response
FWHM	Full width at half maximum
GSVD	Generalized singular value decomposition
Hb	Oxygenated hemoglobin
HbO_2	Deoxygenated hemoglobin
ICG	Indocyanine green
IMMI	Interpolated matrix model-based inversion
LSQR	Algorithm for solving sparse linear equations
LV	Limited-view
MB	Model-based algorithm
MRI	Magnetic resonance imaging
MSE	Mean square error
MSOT	Multispectral optoacoustic tomography
NIR	Near-infrared
OPO	Optical parametric oscillator

OA	Optoacoustic
OAT	Optoacoustic tomography
PLSQR	Preconditioned LSQR
PSF	Point spread function
PV	Partial-view
PVc-wMB	Partial-view-corrected weighted model-based
ROI	Region of interest
RMSD	Root mean square deviation
SIR	Spatial impulse response
SNR	Signal-to-noise ratio
SVD	Singular value decomposition
TGSVD	Truncated generalized singular value decomposition
TIR	Total impulse response
TSVD	Truncated singular value decomposition
wBP	Weighted backprojection
wMB	Weighted model-based
XCT	X-ray computed tomography

TABLE OF CONTENTS

1. INTRODUCTION

1.1 Biomedical and biological imaging

A fundamental concept in health care is the ability to make a precise diagnosis of a patient's condition without affecting the patient or the condition itself to allow for evidence-based treatment [1], [2]. Historically, physicians used their senses to draw conclusions and decide for the treatment. Scientific inventions have driven medical advances and can sometimes be considered extensions of the physician's natural senses. However, the information value obtained is very limited and does only reflect a small fraction of the overall state of the patient [3].

As the understanding of the interactions between energy and matter grew, it became possible to extract information of the condition of matter by the observation how it interacts with energy. New detection methods became available and the type of energy used is no longer limited by the human senses. Therefore, a whole new field of study emerged for diagnosis [4]. Some form of energy may penetrate deeply into the body, undergo interactions and deliver information not accessible otherwise. The novel field of medical imaging has revolutionized diagnosis and monitoring of diseases [5]. The progress of clinical applications is strongly correlated with advances in physics and biology. Interestingly, biological research faces similar challenges as medicine: understanding the condition of a biological system, may it be a single cell or a living organism, without affecting its very condition [6].

Nowadays, a variety of medical equipment is used to deliver healthcare services. Different scientific fields contribute significantly to the development of new technologies for medically and

biologically relevant questions, making this field of research highly interdisciplinary. Visual examination of the patient may be considered the simplest and yet perhaps most relevant form of medical imaging. However, A metabolism is a highly cross-linked system. Therefore, any medical condition arising from a particular region or organ can affect the entire organism, including externally accessible body parts, such as the skin, eyes, etc. An experienced physician can draw profound conclusion on the patient's condition. However, accurate and qualitative information can only be provided by making spatially-resolved measurements, introducing the field of medical imaging [7], [8].

1.1.1 X-Ray imaging

The first modality that allowed access to areas within the body was X-ray imaging—opening radiology as a new field of medicine [9]. X-rays feature a very short wavelength (5-250pm), about 1000 times shorter than visible light. Therefore, X-rays interact with the inner electrons in the K- and L- shells of atoms (inner photoelectric effect), which feature a much lower absorption coefficient than the molecular interaction of visible light, hence penetrating far deeper. The interaction cross-section of X-rays σ is proportional to the nuclear mass of the target:

$$\sigma \propto \frac{Z^5}{E^{\frac{7}{2}}},$$

where E is the energy of the X-ray photons and Z is the atomic number of the target. X- rays can provide a contrast of the distribution of heavier elements in the body. For medical applications, they allow an accurate segmentation of calcium-containing bone tissue and soft tissue [10].

X-rays are conducted as transmission measurements, where the specimen is placed between the source and the detector such as photo-stimulated luminescence plates (PSP). An example of a human full body scan, demonstrating the penetration capabilities of X-rays is shown in Figure 1.1. The entire skeleton of the patient is visible and bone fractures in both upper legs revealed. Some inner organs in the thorax and abdomen can also be seen. The lungs are well visible as they are filled with air, which does not attenuate X-rays. As X-rays examinations are transmission measurements, they generate maximum intensity projections (MIPs) and do not provide depth information. This was addressed by introducing computer tomographic (CT) devices. By replacing the PSP plates with electric sensors such as photomultiplier tubes or image sensors, X-ray density measurements suitable for electronic processing could be generated [11], [12]. Based on a mathematical framework, a three-dimensional distribution map of X-ray absorption could be created [13]. In addition, unlike X-ray, CT allowed segmentation not only of bones, but also of soft tissue [14]. Functional information can be achieved by administering contrast agents [15]. Figure 1.2 demonstrates how CT imaging improves diagnostics compared to conventional X-ray imaging. It shows the right hip of a patient who
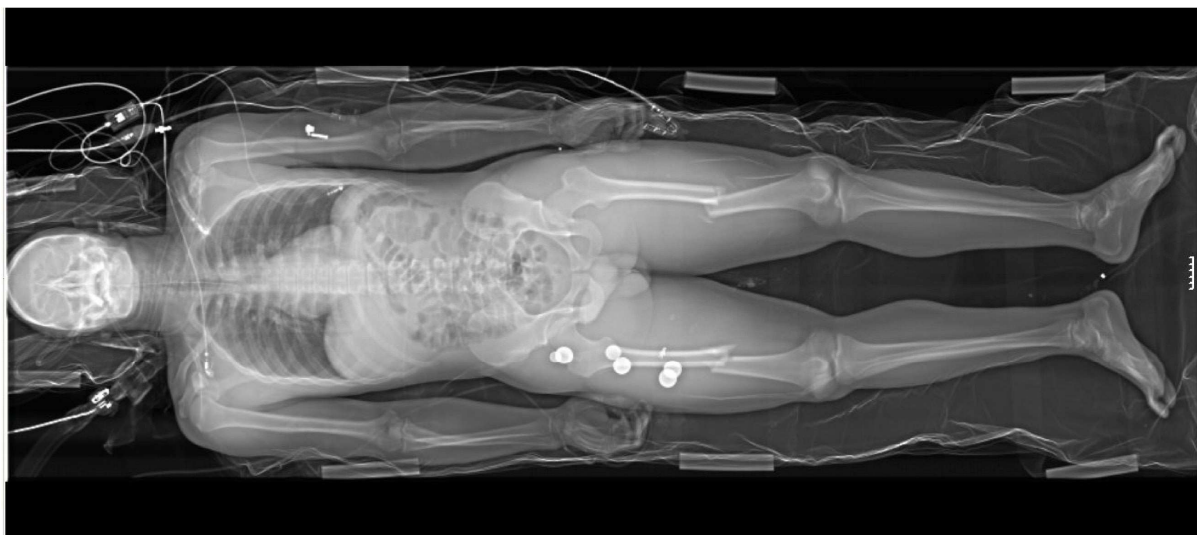
Figure 1.1 Full body X-ray scan of trauma patient [11].   As the bones contain calcium, which has a higher atomic mass than the elements of other tissues, they strongly absorb X-rays, enabling bone-tissue separation. The lungs are filled with air, which interacts even less with X-rays than soft tissue. Therefore, they are well visible in the image.

has suffered a femoral neck fracture. (a) and (b) show two X-ray images that do not reveal the fracture. A subsequent CT scan presented in (c) clearly shows the injury.
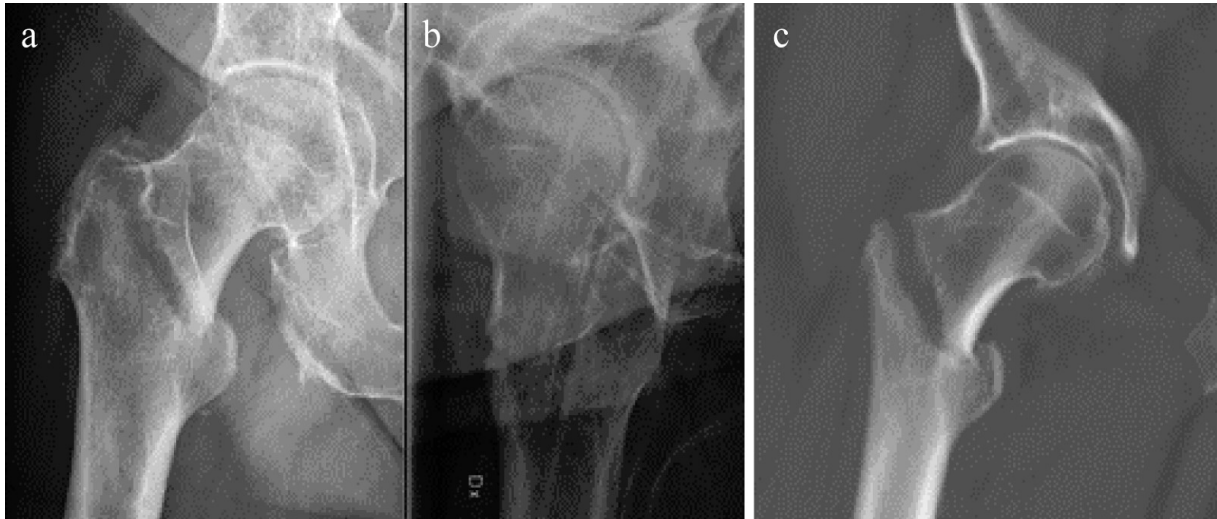
Figure 1.2 Hip fracture unresolvable by X-ray, but visible in CT-scan. (a & b): X-ray image of the hip of a 78-year-old patent after fall. A fracture has been masked by a skin fold and is therefore not visible. (c) CT-scan of the same region revealing the injury (Image licensed under Creative Common License by Mikael Häggström).

1.1.2 Magnetic resonance imaging

X-rays are ionizing radiation and pose a significant burden to the patient, reducing the frequency of diagnostic scans [16], [17]. Additionally, the contrast of different soft tissues is extremely low; making it difficult to identify abnormalities such as tumorigenesis in early stages. A fundamental improvement was introduced by magnetic resonance imaging (MRI) [18], [19]. In the presence of a magnetic field, spin-carrying nuclei like hydrogen orient themselves parallel to the magnetic field. When absorbing energy from an electromagnetic field, the nuclei may flip and orientate themselves anti-parallel to the magnetic field. After a characteristic relaxation time, the nuclei flip back to their original orientation, re-emitting the same energy they previously absorbed by flipping. The energy required for the flip to occur is proportional to the strength of the magnetic field and the magnetic moment of the nuclei. For a hydrogen atom, it is:

$$E_m = \mu \cdot B,$$

where E_m is the energy required for the spin flip to take place, B is the magnetic field and μ is the magnetic moment of the nucleus. If the amplitude of the magnetic and electromagnetic field match the formula for E_m, the spin flip may take place. The withdrawn energy from the electromagnetic field can be detected. Imaging is performed by applying magnetic field gradients in three dimensions to the sample. This way, the formula for E_m is only fulfilled one location in space at a time. By varying the gradients, this location can be scanned through the sample, creating a hydrogen density map of the sample. As this is a strong indication for the type of tissue at hand, superior soft tissue contrast can be achieved with high resolution at any point in the human body. An example presenting the soft tissue contrast inside a human head is shown in Figure 1.3. Various anatomical structure can be seen, including substructures of the human brain, which consist of the same cell type at different densities. For magnetic field strength in the order of a few Teslas, E_m is in the order of a few meV, comparable to the mean thermal energy of the hydrogen atoms at room temperature. Hence, nuclei can be flipped by their thermal energy, even if the formula for E_m is not fulfilled, causing significant noise to the MRI measurement. This can be met by using very strong magnetic fields or increasing the acquisition time. Since the formula for E_m has to be mapped over the entire sample, the magnetic field must be very homogeneous. MRI devices with strong magnetic fields are very difficult to build—highlighting the main disadvantage of MRI. In addition, only one point in space can be measured at a time, resulting in long scan times of several minutes up to hours.
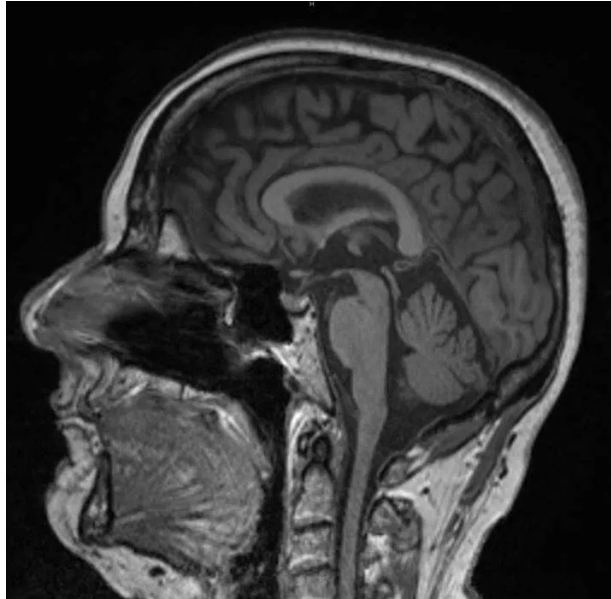
Figure 1.3 MRI scan of human head.　The scan presents a cut through sagittal plane of a human head. The grey value of the image corresponds to the hydrogen content of the tissue. The different tissue types are clearly identifiable by their hydrogen content (Image provided by LearningNeurology.com)

1.1.3 Ultrasound

Ultrasound defines acoustic waves with frequencies above 20 kHz [20]. In water, this yields a wavelength of λ = 7.5 cm and a wavelength of below λ = 1 μm is obtained for frequencies in excess of f = 1.5 GHz assuming sound velocity v_s = 1500 ms^{-1}. Being an uncharged mechanical wave, ultrasound commonly does not strongly interact with most materials and only experiences limited attenuation, depending on the material's mechanical properties. Consequentially, it is a suitable probe to detect structures in the size of its wavelength. Depending on the application, these can be macroscopic morphology, such as entire organs of human patients or much smaller skin features [21]. An example of the imaging potential of sonography is given in Figure 1.4 [22]. Due to the limited interaction between ultrasound and matter, the contrast of sonographic imaging is general very low. The backscattered ultrasound is normally caused by acoustic impedance mismatches. In living tissue, these are very high between bone tissue, soft tissue and hollow organs

(typically containing fluids or air). Other structures are typically very difficult to visualize [23]. Furthermore, ultrasound experiences an increase in attenuation at higher frequencies. This will be discussed in depth later. Consequentially, high frequencies carrying information of small structures are readily absorbed, limiting high resolution ultrasound imaging to superficial tissue [24].

Figure 1.4 Example for sonographic imaging of human fetus [22]. Abdominal sonographic scan of monoamniotic twins at age of 15 weeks.

1.2 Optical imaging

Visible light interacts with the outer electrons of molecules which determine their chemical properties. Thus, it carries information about the chemical structure of the sample [25]. Consequentially, light is an ideal probe to obtain medical information. However, it is scattered by microscopic structures in the body, such as cell cores and organelles. In addition, light is absorbed by different chromophores [26]. So, high resolution optical imaging can only be achieved close to the surface, where the penetration of light is short compared to the attenuation length. This is a viable method for skin or hollow organ examination [27]. Imaging deeper tissues requires biopsies, which pose serious stress to the patient. In recent years, optical imaging methods that allow for deeper penetration while maintaining high resolution have been investigated.

1.2.1 Optical diffuse imaging

Numerical methods to solve the scattering problem of light have been considered. Early attempts in imaging low-scattering breast tissue have been made, but have proven of little clinical value [28]–[30]. However, when utilizing time-dependent light sources and detectors, computational methods allow to measure the spatial distribution of the absorption coefficient, an approach known as optical diffusion imaging [31]. There have been various implementations, which can be split up into two main categories; time-domain systems that use short laser pulses [32], [33], and frequency-domain systems that use continuous sinusoidal modulated lasers [34], [35]. These modalities allow considerable penetration depth of several tens of centimeters. However, even the best performing systems can only offer resolutions in the order of mm to cm [31].

1.2.2 Confocal microscopy

To reconstruct the light propagation in tissue, methods based on differentiation between scattered and non-scattered photons have been considered. In biological tissue, the scattering coefficient is typically 1-2 orders of magnitude greater than the absorption coefficient—this will be discussed in detail later. Hence, some light will be able to reach deeper layers before being absorbed, but the photons will be increasingly randomized. Confocal microscopy allows to select the non-randomized photons by leading the beam path through a pin hole [36]–[38] (Figure 1.5a). The incident light (blue) originates from the source filtered by the pinhole and is guided to the sample through an objective lens. The florescence light from the focus of the objective passes back through the objective and travels back to the detector behind another pinhole. The pinhole will reject any light that does not originate from the focus of the objective. Figure 1.5b shows a biological sample that has been imaged using confocal microscopy. Figure 1.5c shows the same sample after the pinholes have been removed, so that the setup behaves like a conventional microscope.
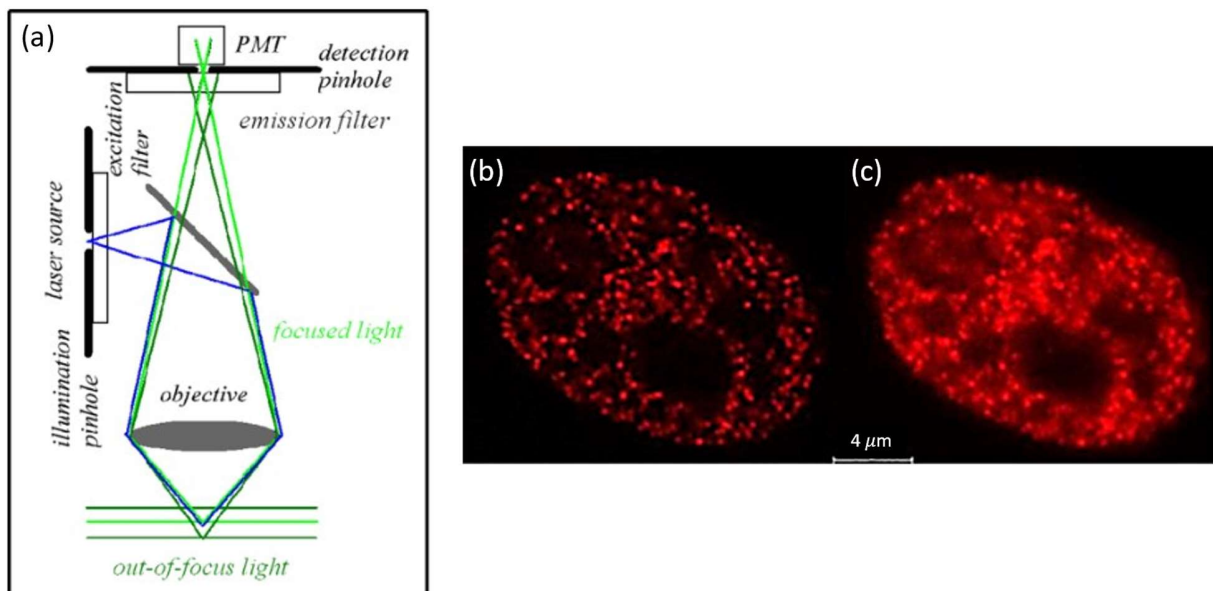
Figure 1.5 Principal of confocal microscopy and illustrative example [38].   (a) conceptional of confocal microscopy. (b) single HeLa-cell nucleus with labeled DNA acquired by confocal microscope. (c) Same image acquired with the pinhole opened completely, removing the confocal effect.

1.2.3 Two-photon microscopy

Alternatively, two-photon processes can be used to enhance the penetration depth [39] (Figure 1.6(a)). The detection wavelength is chosen to be half of the excitation wavelength. Two photons have to combine in a non-linear process to generate a detectable signal. This implies that the output signal is proportional to the photon density squared [40] (Figure 1.6(b)). This results in a more defined focus, even in the presence of scattering (Figure 1.6(c)). However, non-linear processes are highly dependent on the light flux, hence most applications require pulsed lasers to generate detectable two-photon signals. This increases the system cost and puts limits on the acquisition speed to avoid the tissue to be damaged by the high light flux.
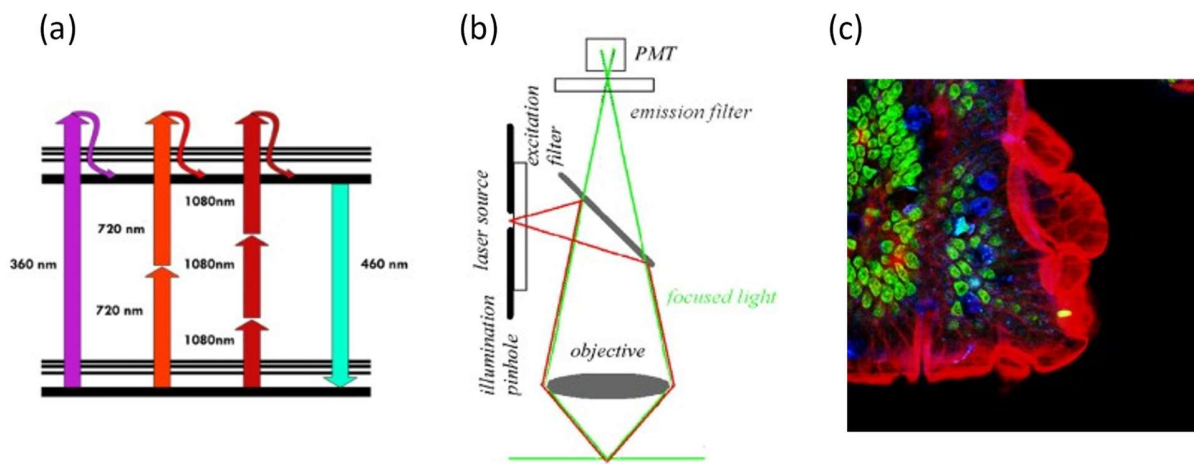
Figure 1.6 Principal of two-photon microscopy and illustrative example [39].   (a) Energy states which are excited by two low energy photons simultaneously result into a single high energy photon at a shorter wavelength. (b) Setup of a two-photon microscope: the fluorescence light is separated from the excitation light by a dichroic beam splitter. Only the fluorescence light from the focus reaches the detector. (c) Two-photon image of a cryosliced mouse intestine. Different cell features are labeled with different fluorescence agents.

1.2.4 Optical coherence tomography

Optical coherence tomography (OCT) is a method where large volumes can be acquired and allows enhanced penetration depth. The concept of OCT is to replace the pin hole of a confocal microscope with a *Michelson Morley* interferometer using a low coherence light source (Figure 1.7(a)). The sample under investigation is placed at the end of one arm of the interferometer. By scanning the mirror position on the reference arm, photons reflected from the depth within the sample corresponding to the length of the reference arm undergo constructive interference, allowing depth segmentation. Hence, depth scanning is performed in the time domain [41], [42]. Using an OCT scan of human skin, detailed anatomical features can be resolved (Figure 1.7(b)). The image also demonstrates the limited penetration depth of OCT and the inability to resolve strongly absorbing features, such as blood vessels.
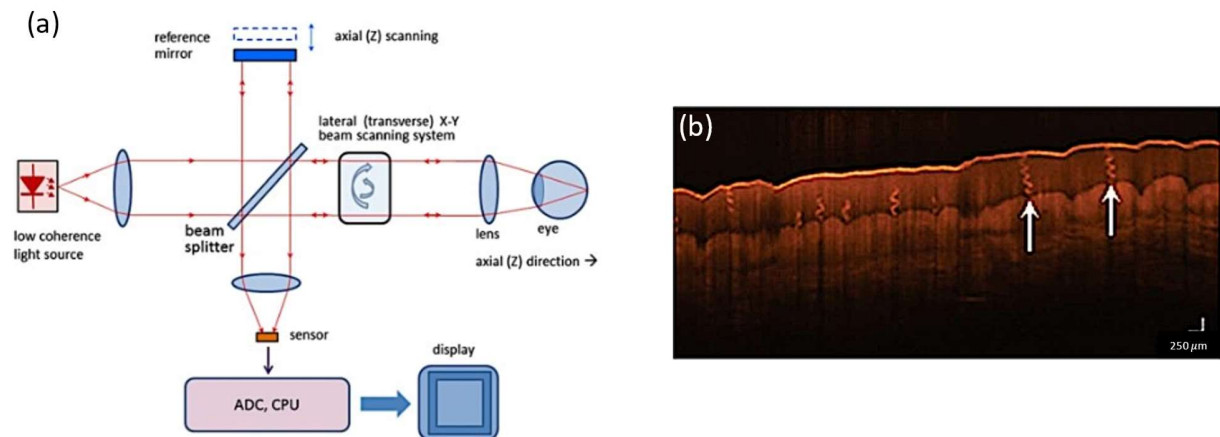
Figure 1.7 Principal of optical coherence tomography [42] and illustrative example.   (a) System setup of a time domain optical coherence tomography setup, a combination of a Michelson interferometer and a confocal microscope. (b) OCT scan of human skin. The high resolution is illustrated by various skin features, including sweat glands (white arrows).

A common problem of these microscopy technique is that the focus has to be scanned in three dimensions, which leads to long acquisition times. A solution is presented by frequency-domain (or spectral) optical coherence tomography (FD-OCT) featuring a wideband light source [43]. In

this implementation, each optical wavelength in the excitation source corresponds to a different penetration depth. Using a spectroscopic detector, depth information can be acquired without the need for scanning. Finally, another implementation of optical coherence tomography utilizes a light source with a sweep-able wavelength (swept-source OCT) [44]. As in FD-OCT, each optical wavelength covered by the source corresponds to a particular penetration depth, which is being mapped into the time domain. However, a frequency sweep can be performed extremely fast, enabling accelerated image acquisition [45].

1.3 Optoacoustic (OA) imaging

1.3.1 Single-wavelength OA imaging

As an inherently hybrid imaging modality, optoacoustic (OA) (also known in the literature as "photoacoustic") imaging capitalizes on the strengths of optical and acoustic (ultrasound) imaging for the purpose of acquiring of high-resolution images with molecular specificity from depths not accessible to any optical modality [46]–[49]. The underlying physical phenomenon is the photoacoustic effect, which describes the induction of acoustic pressure waves following the absorption of light [50]. In optoacoustics, the biological tissue is illuminated with modulated light to generate acoustic responses from optical absorbers due to the thermoelastic expansion of tissue [51]. Thus, similar to purely optical imaging methods, OA imaging illuminates the specimen with light. However, instead of collecting photons for image production, OA imaging makes use of the conversion of the light energy into ultrasound waves by optical absorbers, by detecting the latter using conventional ultrasonic transducers [52]. As a result, OA imaging combines the molecular specificity of optical imaging with the capabilities of spectral differentiation of molecular

absorbers. Since sound waves are scattered orders of magnitude less than light waves as they propagate through tissue, OA imaging enables the generation of high-resolution images at depths limited only by ultrasound diffraction. Through such merging of light and sound capabilities, OA imaging gains a great degree of imaging flexibility with fully maintained molecular specificity and spectral flexibility [53].

OA imaging as an emerging biomedical imaging modality has been widely used in preclinical and clinical research [54]–[57]. It is usually implemented in the time domain using high-energy light pulses (>10 mJ/pulse) lasting shorter than approximately 10 ns to induce acoustic responses from optical absorbers. Time-domain OA imaging generates broadband acoustic signals due to the ultrashort excitation profile, ranging from MHz up to hundreds of MHz [58], [59], generated by objects with sizes between 1.5 mm and <15 µm. OA imaging can also be implemented in the frequency domain using intensity modulated continuous wave lasers [60], which offers mainly the advantage of using economic light sources such as diode lasers which are technically simpler and more stable, as opposed to the optical parametric oscillator (OPO) based technology used in time-domain OA imaging [61], [62].

1.3.2 Multispectral OA tomography (MSOT)

As a subclass of OA imaging, multispectral OA tomography (MSOT) has been developed and applied in biomedical applications, demonstrating the ability to differentiate tissues *in vivo* and *ex vivo* in real-time with and without the application of contrast agents several millimeters deep in the biological specimen with numerous research and translational applications for biomedical imaging [63], [64]. Offering much higher resolution than diffuse optical tomography [65], MSOT

is able to resolve morphological structures and to accurately quantify tissue biomarkers, which is not possible using diffuse photons [55].

MSOT takes the advantage of multi-wavelength illumination operating in the near-infrared (NIR) spectral region, which allows deep penetration in tissue [64], and tomographic detection, which enables high signal-to-noise ratio (SNR). The illumination wavelength of MSOT is normally between 650 nm and 950 nm which is known as the first optical window. This spectral range is widely used in tissue studies, since tissue is of minimal absorption and less scattering in the first optical window than that in shorter wavelengths [66], therefore enables the delivery of sufficient optical energy to generate detectable acoustic pressure from 30–60 mm depths [54].

Different from single-wavelength OA imaging, MSOT results in at least 3D image stacks, i.e. two spatial dimensions and another spectral dimension. The spectral dimension is of particular importance for functional analysis in biological studies, since spectral information is the foundation to identify different optical absorbers, whether endogenous (oxygenated and deoxygenated hemoglobin, melanin, and lipid) [53], [55], [67], or exogenous (imaging probes, nanoparticles). For imaging intrinsic absorbers, many tissue physiology studies based on hemoglobin have been carried out. As an important indicator to tissue physiological and pathological conditions, oxygen saturation (sO_2) [68], which is the fraction of oxygenated hemoglobin to the total hemoglobin, has been studied non-invasively with MSOT. Matrix metalloproteinase activity, typically associated with atherosclerotic plaque instability, has been resolved in *ex vivo* human carotid plaques [67]. Lipids, absorbing light in the wavelength range of 1210 nm, were clearly identified and characterized in plaques within human aorta and carotid

artery samples *ex vivo* [69], [70]. For the biomedical applications based on OA contrast agents, a number of moieties that absorb light have been resolved with MSOT, including fluorescent proteins [71], [72], fluorescent dyes such as IRDye800 [73], indocyanine green (ICG) [74]–[78], Alexafluor750 (AF750) [63], carbon nanotubes [79], polymer nanoparticles [80], [81], and gold nanorods (GNRs) [78], [82], [83].

In addition, the multispectral illumination with the help of spectral unmixing algorithms can improve the detection sensitivity of the optical absorbers compared to the single-wavelength image [84]. The detection sensitivity of conventional OA tomography with a single wavelength depends purely on the SNR of the target to background, therefore, an absorber of interest can be studied only if its absorbed light energy is higher than that of the background tissue. However, with multi-wavelength illumination, an absorber of interest can be studied based on its spectral signature. Therefore, even its absorbed light energy is lower than the surrounding background, it can be differentiated from background by its spectral signature. Moreover, when multiple absorbers with distinct absorption peaks exist, they can be differentiated using spectral unmixing methods and help reduce the minimum detectable concentrations in comparison with single-wavelength optoacoustics.

1.3.3 Preclinical (small-animal) MSOT imaging

As an important stepping stone to studying and guiding clinical studies about the progression of human diseases and their corresponding therapies, small animals, especially mice, are widely used in biomedical research [85], which are classified as preclinical studies, while the studies based on humans are classified as clinical studies. For preclinical OA imaging, *in vivo* whole body small-

animal MSOT is of particular interest, since it allows longitudinal studies to follow the disease and therapy progression in a large time scale and enables the development of different human disease models in different organs or tissues on mice [64], [85]. There are several commercial preclinical MSOT systems, including the inVision256 (iThera Medical), Vevo Lazr (Visual Sonics), LOIS-3D (TomoWave Laboratories), Nexus (Endra) and a number of laboratory system designs that have been reported in the literature for imaging small animals.

If we take the inVision256 system as an example to demonstrate the experimental orientations of MSOT imaging, as Figure 1.8 shows, preclinical MSOT comprises mainly three parts: the illumination and detection system, the data acquisition system, and the image formation system [86]. The detection system features a spherically concave array spanning 270° in the xy-plane with a radius of 40 mm [87]. Each single element of the array is manufactured from the same piezocomposite material to cover a frequency band of central frequency 5MHz with -6dB of >50%. For the illumination, a wavelength-tunable pulsed laser with a pulse duration of <10ns, repetition rate of 10 Hz and peak pulse energy of 90 mJ at 750 nm is applied for multispectral measurements from 680nm to 950nm. The laser beam is coupled into a 10-arm fiber bundle next to the transducer array to establish a ring-like illumination at the imaging plane. A custom-made data acquisition (DAQ) system digitizes up to 256 channels in parallel at 10 Hz repetition rate and 40 MegaSamples/second. During *in vivo* measurements, the animal is anesthetized and positioned in an animal holder in the center of the imaging plane.
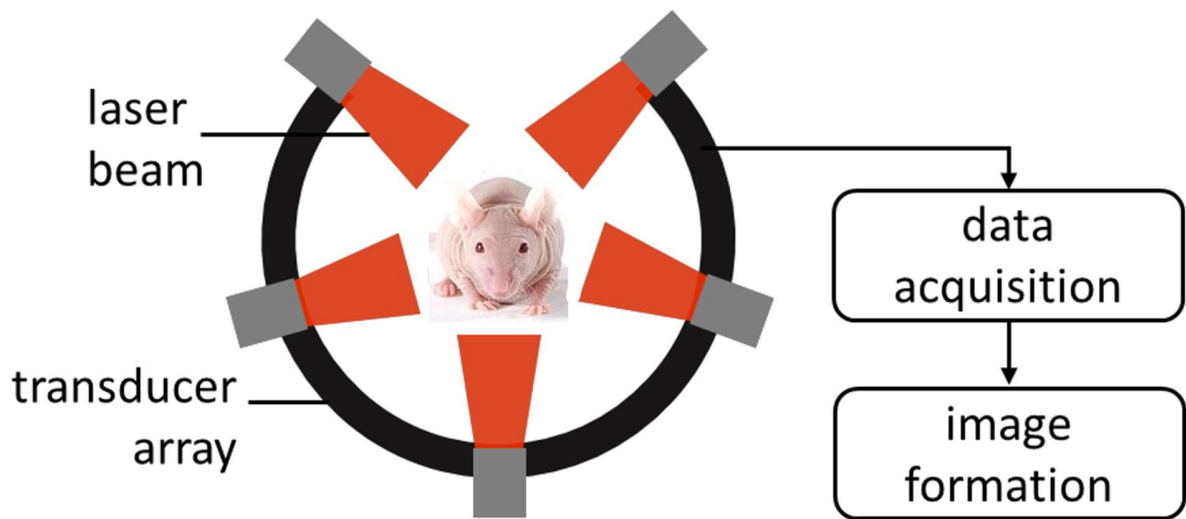
Figure 1.8. Schematic of the major components in a typical MSOT system for small-animal imaging.

1.3.4 Clinical MSOT imaging

Clinical MSOT has recently demonstrated potent clinical imaging abilities in cancer detection [88]–[91], label-free assessment of tissue inflammation [92], [93], tissue metabolism [94], and imaging of vascularization [95]–[97]. Compared to the preclinical MSOT imaging, clinical MSOT imaging has four major changes from hardware design to the imaged specimen, i.e. illumination, detection, acquisition and specimen size. The first change is the hardware design of the transducer array and illumination. In order to bring MSOT into the clinics, a handheld device which is small and portable to allow clinicians scan patients conveniently like the case in ultrasound imaging is needed, which leads to the implementation of illumination and detection in a handheld probe. Such design results in the sample to be illuminated on only one side and only part of the resulting acoustic signal to be collected, which makes clinical OA image reconstruction a very ill-posed problem and results in PV artefacts. The second change occurs in the data acquisition stage. In preclinical MSOT imaging, 10 averages or more are normally used during data acquisition to assure a good SNR of the acquired signals. However, in clinical MSOT, normally no signal

averaging is done during data acquisition at each wavelength in order to achieve real-time imaging and avoid motion artefacts introduced during measurements, which results in a lower SNR of OA signals than that in preclinical MSOT imaging. The third change is the size of the specimen. In clinical OA imaging, the specimen is a human or a tissue or a lesion inside the human body, which is of a much larger size and require deeper imaging depth than in preclinical small-animal studies.

1.4 Outline of this work

In this chapter, we overviewed a couple of mainstream imaging modalities like X-ray, MRI, and ultrasound. Afterwards, we briefly overviewed optical imaging modalities that cover spatial resolutions both in the microscopic and tomographic scales, such as optical diffuse imaging, confocal microscopy, two-photon microscopy, and optical coherence tomography. We then reviewed two OA image acquisition techniques; namely single-wavelength OA imaging and multispectral OA tomography, and their application in preclinical (small-animal) and clinical imaging.

In chapter 2, we will discuss some of the physical & hardware aspects of OA signal formation & detection. First, we will briefly review the physics of light and sound propagation in biological tissue, and how utilizing the underlying physical principles of both gives us the OA effect. Then, technical and hardware aspects of OA signal generation and detection will be discussed, such as optical excitation of media containing optical chromophores using pulsed lasers, detection of the generated OA signals using conventional piezoelectric ultrasound transducers, and the electrical and spatial impulse responses of such transducers. Moving forward, we then discuss some of the algorithmic aspects underlying the formation of OA images in chapter 3. We review two of the

widely used image reconstruction techniques in OA tomography; namely the BP algorithm, and the MB reconstruction algorithm. Effects of LV (PV) imaging scenarios on the quality of the OA reconstruction are also discussed.

Then, in chapter 4 we focus mainly on the effects of the presence of acoustic heterogeneities in the imaged sample on the generated OA image and how to address such effects. We review a statistical weighting method that was introduced by colleagues in our research group in the past to BP reconstruction, and then later to MB reconstruction, to mitigate reconstruction artefacts due to the presence of strong acoustic heterogeneities. Then, we investigate the issues of using such statistical approach in the case of PV imaging scenarios. We then introduce a correction technique that we recently published to address such artefacts in order to enhance the usability of the statistical weighting technique in PV detection geometries in the case of MB image reconstruction. The experimental validation of all the methods discussed in this chapter is also included.

We conclude this work in chapter 5 with a summary of the topics discussed and a discussion of future work.

2. PHYSICS & HARDWARE ASPECTS OF OA SIGNAL FORMATION & DETECTION

The aim of this chapter is to review the physical and some hardware aspects of OA imaging. The chapter is divided into two parts: Section 2.1 presents the physics for OA imaging. Starting with light and sound behavior in tissue, it also discusses OA signal generation, the forward solution to the equation of OA wave propagation, and related effects such as the directivity of signals. Section 2.2 presents technological requirements and general instrumentation for OA imaging as well as detection system related parameters such as the electrical and spatial impulse response. An understanding of these parameters is important since they influence reconstruction accuracy and thus should be considered in the acoustic inversion process, as will be demonstrated later in chapter 3.

2.1 Physics of OA imaging

2.1.1 Light propagation in tissue

All matter is composed of charged particles, like protons, electrons and ions. Electromagnetic waves, such as light, interact with these charged particles [98]. When light propagates through biological tissue it might therefore be scattered and/or absorbed. Scattering refers to the redirection of light and is strongest in structures whose size match the optical wavelength. In the visible and near infrared range (400 - 1000 nm), these structures are the supporting tissue like elastin or collagen, blood cells and cell organelles, such as nucleus, mitochondria or endoplasmic reticulum

[99]. Absorption means uptake of electromagnetic energy by the electronic and vibrational structures of the tissue constituents and is intrinsically sensitive to chemical composition [98]. Absorbed light can be converted into heat, consumed in a chemical reaction or re-emitted, for example as fluorescence.

Important intrinsic absorbers in biological tissue are oxygenated (HbO_2) and deoxygenated (Hb) hemoglobin, tissue pigments like melanin, water and lipids [65]. Figure 2.1 shows their absorption spectra. Absorption in tissue is strongly sensitive to the wavelength. There is an optical window between 650 - 900 nm in which the optical absorption of tissue drops two orders of magnitude, which allows penetration of light relatively deeply (up to several centimeters into biological tissue). Below 650 nm, light penetration is hindered by hemoglobin absorption, above 900 nm by water absorption. To describe the scattering, one uses the bulk scattering coefficient μ_s, which gives the probability of a scattering event per unit path length. In biological tissue, μ_s has an approximate value of 100 cm^{-1} [98]. To describe the optical absorption, an analogue expression termed the optical absorption coefficient is used with a representative value in biological tissue between 0.15 - 0.5 cm^{-1} at 750 nm [99]. Optical absorption in tissue is weak compared to scattering.
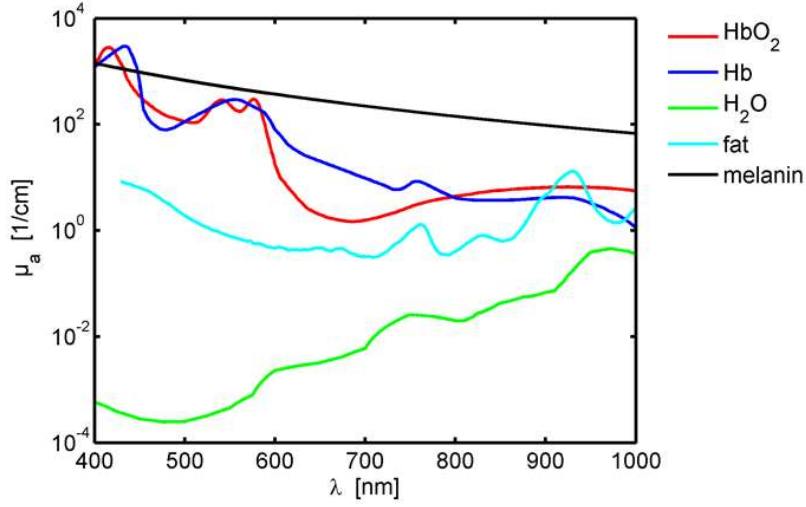
Figure 2.1 Absorption spectra of common tissue absorbers. A hemoglobin concentration of 150 mg(ml)$^{-1}$ is assumed. *Data compiled by Scott Prahl, Oregon Medical Laser Center (http://www.omlc.ogi.edu/spectra).*

The mean free path between two scattering events is only about 0.1 mm, whereas the optical absorption length can extend to 10 - 100 mm. As a consequence, light is scattered multiple times before being absorbed and progressively loses its directivity shortly after entering the tissue. With respect to light propagation in tissue, one therefore distinguishes between two regimes: the *ballistic regime* (under 1 mm), in which light is not (or hardly) scattered and therefore still preserves its original directivity, and the *diffusive regime* where light propagates omnidirectionally due to multiple scattering events. In the ballistic regime, light transport can still be described by the laws of geometrical optics and in the diffuse regime one generally uses the diffusion equation [65]:

$$\frac{1}{c}\frac{\partial \Phi(\boldsymbol{r},t)}{\partial t} - \overrightarrow{\nabla}D(\boldsymbol{r})\overrightarrow{\nabla}\Phi(\boldsymbol{r},t) + \mu_a(\boldsymbol{r})\Phi(\boldsymbol{r},t) = S(\boldsymbol{r},t), \tag{1}$$

where $S(\boldsymbol{r},t)$ is the source term, $\Phi(\boldsymbol{r},t)$ is the fluence rate in J(m³s)$^{-1}$, c in ms^{-1} is the speed of light and $D(\boldsymbol{r}) = 1/3(\mu'_s + \mu_a)$ is the diffusion coefficient. $\mu'_s = (1-g)\mu_s$ is the reduced scattering coefficient established to describe the light scattering as an isotropic phenomenon, although each individual scattering event is anisotropic. In other words, it is a measure to describe

directive scattering in an isotropic scattering environment. g is the anisotropy factor which takes into account this loss of directivity and has a value between 0.8 and 0.99 in biological tissue [99].

In optoacoustics, light fluence inside tissue is often estimated under continuous-wave illumination. This is possible because photon propagation through the region of interest is significantly shorter than the duration of the laser pulse used for excitation [100]. In this case, the diffusion equation (1) simplifies to

$$\nabla^2 \Phi(\boldsymbol{r}) + \frac{\mu_a}{D(\boldsymbol{r})} = \frac{S(\boldsymbol{r})}{D(\boldsymbol{r})}. \tag{2}$$

For uniform broad beam illumination, the light fluence within the object can be approximated by the 1D solution of the diffusion equation. It follows the Beer's law and is given by [65]:

$$\Phi(r) = \Phi_0 e^{-\sqrt{\frac{\mu_a}{D}}r}, \tag{3}$$

where r represents the distance from the surface. To get a realistic idea about the effect of the light attenuation in tissue, one has to consider tissue-realistic values ($\mu_s' = 10\text{cm}^{-1}$ and $\mu_a = 0.3\text{cm}^{-1}$). Using these values in Eq. (3), we see that 1 cm below the surface, the light fluence has already dropped to about 5% of its initial value. As will be shown later, the OA signal strength is proportional to the light fluence. Signals from deep inside the mouse are therefore weaker than signals from the directly illuminated surface. In this respect, light attenuation is a major challenge in OA tomography which—from an instrumentation point of view—has as a consequence that the detection system has to be very sensitive with a large dynamic range to detect both the weak signals from deep inside the mouse and the strong signals from superficial structures [64]. Moreover, special attention should be paid to optimizing the light delivery, for instance by illumination from several directions, in order to maximize the light deposition in deep tissue structures.

2.1.2 Sound propagation in tissue

Acoustic waves at frequencies higher than 20 kHz are referred to as ultrasound. Ultrasound travels through tissue in form of a longitudinal compression wave. The propagation speed v_s [ms^{-1}] of acoustic waves in tissue depends on the density ρ [g/cm^3] and compressibility κ [Pa-1] of the material:

$$v_s = \sqrt{\frac{1}{\rho\kappa}}, \tag{4}$$

i.e. the denser or more rigid the material, the higher the propagation speed. In soft tissue or water, the velocity is about 1500 ms^{-1}. Variations are typically in the order of 5%. The sound speed for bones is approximately 3500 ms^{-1} and in air around 330 ms^{-1} [99]. The product of sound speed and material density is called the acoustic impedance:

$$Z = v_s\rho. \tag{5}$$

The unit of the acoustic impedance is Rayl, corresponding to kg.m^{-2}.s^{-1}. The pressure generated by these acoustic waves depends on the displacement velocity of the particles v_d:

$$P = Zv_d. \tag{6}$$

If a sound wave hits an interface between areas with different acoustic impedances at normal incidence, a fraction of the intensity of the incident wave will be reflected back into the first medium according to

$$R = \left(\frac{Z_2 - Z_1}{Z_2 + Z_1}\right)^2 \quad \& \quad T = \frac{4Z_1Z_2}{(Z_1 + Z_2)^2}, \tag{7}$$

where R is the reflection and T is the transmission coefficient describing the percentage of the reflected and transmitted energy, respectively [101]. Reflection of ultrasonic waves by tissue structures is the basis of ultrasound imaging, where these reflected waves are detected and used to

form an image. Since the difference in acoustic impedance in soft tissue is rather small (between 1.38 and 1.63 MRayl), ultrasound imaging only provides limited soft tissue contrast but a good penetration depth [99]. On the other hand, the acoustic mismatch between tissue and air ($Z = 416$ Rayl) is quite high. Therefore, whenever acoustic waves are to be detected outside the tissue (e.g. in OA imaging), a matched coupling medium (e.g. water) has to be used to enable propagation of the acoustic waves to the detector; otherwise they would remain confined in the tissue. If the ultrasound wave arrives upon a boundary at an angle, it is refracted. The change of the angular direction of the transmitted wave depends on the speed of sound of the two materials according to Snell's law:

$$n = \frac{\sin(\theta_i)}{\sin(\theta_t)} = \frac{v_{s_1}}{v_{s_2}}, \tag{8}$$

where n represents the index of refraction. In soft tissue $n \approx 1$, thus ultrasound is little refracted and generally preserves its direction of propagation. When an ultrasound wave encounters a surface roughness or particles much smaller or approximately equal to the acoustic wavelength, it is scattered. However, the scattering coefficient for ultrasound in tissue is 2-3 orders of magnitudes less than for light and can be ignored in OA imaging [98]. Due to the reduced scattering and little refraction of the acoustic waves in soft tissue, ultrasound imaging can achieve much higher resolution in deep tissue than optical imaging methods.

When propagating through tissue, acoustic waves are also attenuated. This is mainly due to friction losses when tissue particles are displaced and can be described phenomenologically by [39]

$$p(r) = p_0 e^{-\alpha(f)r}, \tag{9}$$

where p_0 is the initial amplitude, r is the propagated distance [cm] and $\alpha(f) = Af^m$ is the attenuation coefficient [dB.cm^{-1}] in which $1 \leq m \leq 2$. A is a tissue-dependent constant with a

typical value of 0.5 dB.MHz^{-1}.cm^{-1} and f is the frequency of the wave [MHz]. Hence, biological tissues act as a low-pass filter, attenuating high frequencies more than low frequencies. Since resolution depends on the availability of high frequencies, imaging depth scales with resolution loss. Nevertheless in all that follows, acoustic attenuation is neglected because we are dealing with macroscopic imaging in the frequency range up to 7 MHz and depths up to 2.5 cm. For such frequencies, signal attenuation and distortion due to acoustic attenuation is small compared to the signal distortion and filtering due to the transducer properties and light attenuation [58].

2.1.3 *Light + ultrasound = the OA effect*

OA imaging is based on a phenomenon called the photoacoustic (or OA) effect. It was discovered more than a century ago by Alexander Bell [102] and describes the conversion of electromagnetic radiation into acoustic waves via thermoelastic expansion.

OA signal generation and wave propagation

The process of the OA signal generation can be understood as follows: when an object is irradiated with a short laser pulse, and the light is then absorbed by the object, some of the absorbed energy is converted into heat. This induces a temperature rise (in the order of millikelvins) and pressure builds up. The tissue then relaxes by heat diffusion and emission of the OA waves.

Two important timescales exist for OA signal generation:

- The thermal relaxation time τ_{th} defined as the time it takes for the heat to dissipate into the neighbouring volume elements

46

$$\tau_{th} = \frac{d_c^2}{D_T}, \tag{10}$$

where d_c is the size of this elementary volume (resolution-limited voxel) and $D_t \sim 1.4 \times 10^{-3}~cm^2 s^{-1}$ (in soft tissue) is the thermal diffusivity. If the exciting laser pulse is shorter than the thermal relaxation time, the heating, and also the generation of the OA signal, is localized. This is known as the condition of *thermal confinement* [65].

-   The stress relaxation time defined as the time the pressure takes to propagate through a resolution-limited voxel d_c:

$$\tau_s = \frac{d_c}{v_s}, \tag{11}$$

where v_s is the speed of sound. If the laser pulse is shorter than the stress relaxation time, then pressure relaxation during the initial pressure rise is avoided and the OA signal generation is optimized. This condition is known as *stress confinement* [65].

Generation and propagation of the OA signals is described by the OA equation. Under thermal and stress confinement it is [14]:

$$\frac{\partial^2 p(\boldsymbol{r}, t)}{\partial t^2} - v_s^2 \nabla^2 p(\boldsymbol{r}, t) = \Gamma \frac{\partial H(\boldsymbol{r}, t)}{\partial t}, \tag{12}$$

where $p(\boldsymbol{r}, t)$ denotes the photoacoustic pressure [Pa] at location $\boldsymbol{r}$ and time t. $H(\boldsymbol{r}, t)$ in J(m³s)⁻¹ is the heating function defined as the energy per unit volume and unit time deposited by the electromagnetic radiation and converted into heat. $\Gamma = \beta v_s^2 / C_p$ is the dimensionless and temperature-dependent *Grüneisen* parameter which describes the conversion properties of the

medium, in which C_p is the isobaric heat capacity in J(kgK)$^{-1}$ and β is the isobaric volume expansion coefficient [K^{-1}]. The heating function is proportional to the fluence rate $\Phi(\boldsymbol{r}, t)$ of the excitation radiation, as well as the optical absorption $\mu_a(\boldsymbol{r})$ of the medium. Thus,

$$H(\boldsymbol{r}, t) = \mu_a(\boldsymbol{r})\Phi(\boldsymbol{r}, t). \tag{13}$$

Since propagation of light can be considered instantaneous, the heating function is generally separable, *i.e.* it can be decomposed as $H(\boldsymbol{r}, t) = H_r(\boldsymbol{r})H_t(t)$. In most biological tissues, except from bones, lungs and other air-containing body cavities, Γ as well as v_s vary only slightly and can therefore be considered as being spatially independent [103]. The left-hand side of Eq. (12) describes the wave propagation, whereas the right-hand side gives the source of the OA signal generation. The first-order derivative in the source term shows that the heating has to be time-variant, otherwise it is not possible to generate an OA signal.

For impulse heating, *i.e.* $H_t(t) = \delta(t)$, the temperature rise within the sample is given by

$$T(\boldsymbol{r}) = \frac{H_r(\boldsymbol{r})}{\rho C_v}. \tag{14}$$

where C_v in J(kg.K)$^{-1}$ is the specific heat capacity at constant volume [65]. The corresponding initial pressure at point $\boldsymbol{r}$ in 3D space can be expressed as:

$$p_0(\boldsymbol{r}) = \Gamma H_r(\boldsymbol{r}) = \Gamma \mu_a(\boldsymbol{r})\Phi(\boldsymbol{r}). \tag{15}$$

The forward solution to the equation of OA wave propagation

The OA equation (12) can be solved with the Green function approach [65]. Under stress confinement and for delta heating $H_t(t) = \delta(t)$, the expression for the acoustic field can be written as [98]

$$p_\delta(\boldsymbol{r}, t) = \frac{\Gamma}{4\pi v_s^2} \frac{\partial}{\partial t} \left(\frac{1}{v_s t} \int_V H_r(\boldsymbol{r}') \delta \left(t - \frac{|\boldsymbol{r} - \boldsymbol{r}'|}{v_s} \right) d\boldsymbol{r}' \right), \tag{16}$$

where the integration is done over the whole illuminated object V and $\boldsymbol{r}'$ is a point within this object. From the expression we see that a detector at the location $\boldsymbol{r}$ and at time t will sense the integrated pressure, originating from OA point sources on a spherical shell with the radius $v_s t$ and centered at $\boldsymbol{r}$ as shown in Figure 2.2(a). For a homogenous spherical absorber with radius a positioned at $\boldsymbol{r}_s$, it is possible to derive an analytical solution to Eq. (16). It writes as [65]

$$p_\delta(\boldsymbol{r}, t) = p_0 U(a - |R - v_s t|) \frac{(R - v_s t)}{2R}, \tag{17}$$

where U is the Heaviside step function, $R = |\boldsymbol{r} - \boldsymbol{r}_s|$ is the distance of the source from the detection point, and p_0 is the amplitude of the initial pressure. Panel (b) displays the time resolved OA signal from three spheres with the radius $a = 500$ μm, 1 and 1.5 mm, positioned at 36, 38 and
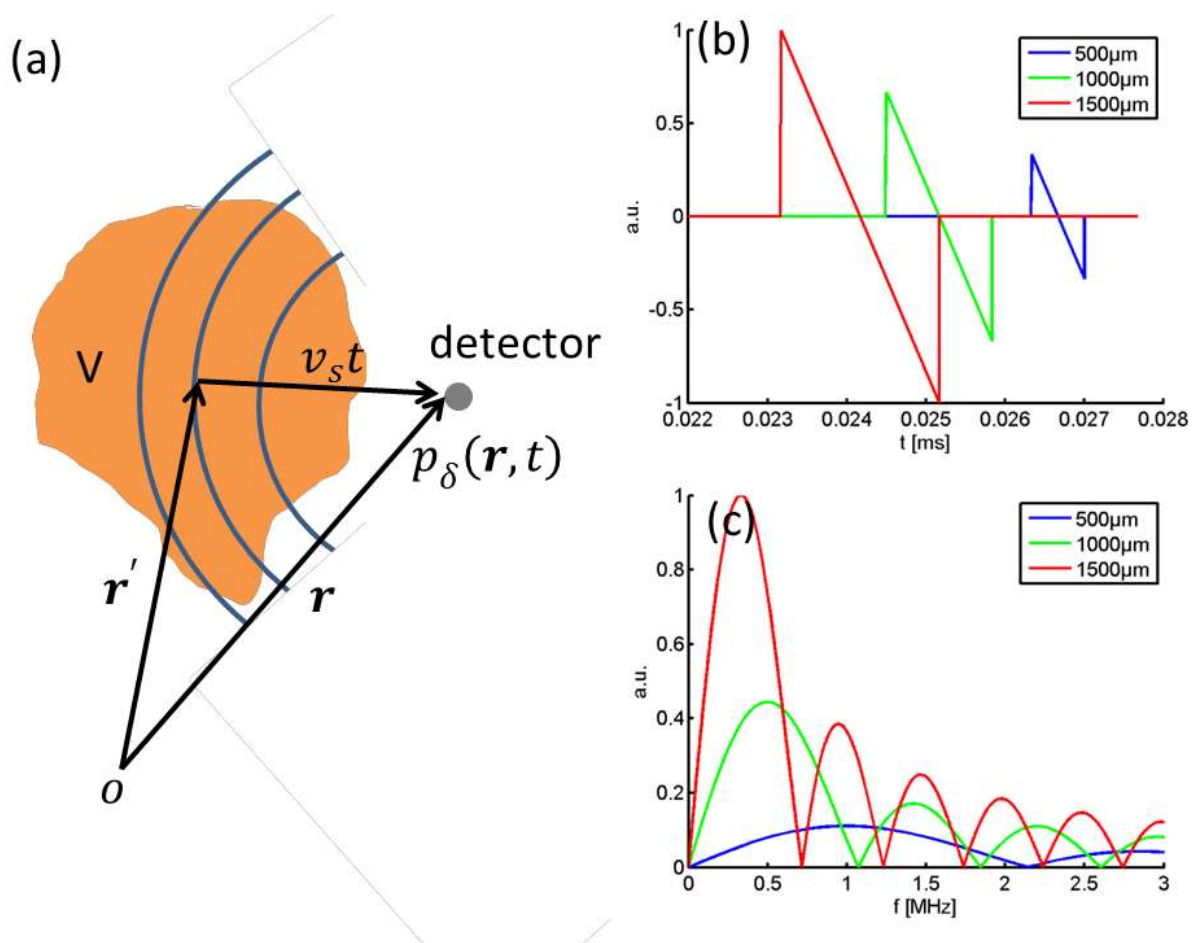
Figure 2.2 Optoacoustic signal propagation & detection.   (a) The optoacoustic signal, detected at a certain time t, by a point detector at $\boldsymbol{r}$, comes from optoacoustic sources located on a spherical shell centered at the detector position with the radius $v_s t$. (b) Optoacoustic signal from spherical sources with a diameter of 1, 2 and 3 mm displays the characteristic bipolar shape. (c) Corresponding frequency spectra.

40 mm, respectively, in front of the detection device. We see the OA signal has a characteristic bipolar shape. The duration of the OA pulse represents the time the sound needs to propagate along the sphere diameter, thus scales with the size of the sphere. The positive peak indicates a pressure rise due to compression followed by a pressure drop due to rarefaction. The pressure amplitude is proportional to the size of the sphere and inversely proportional to the propagated distance. Panel (c) displays the frequency spectrum of the signals obtained by a fast Fourier transformation of the OA signals. The spectra are very broad, ranging from low ultrasonic frequencies which correspond to the dimensions of the acoustic source, to high frequencies from the object boundaries. The

maximal amplitude of the spectra defines the central frequency f_c of the source, which is approximately $\frac{0.8v_s}{2a}$ for a sound speed v_s within the object [104]. The full width at half maximum of the lobe defines the bandwidth B_w of the signal for which the ratio $\frac{B_w}{f_c}$ is constant. We see that frequency and bandwidth scale with the size of the OA source. The smaller the object, the higher is the central frequency and the broader the frequency spectrum. Anatomical structures within tissue span from centimeter-sized objects (e.g. organs), to several micrometers (e.g. microvasculature), thus emit OA waves ranging from frequencies of several kilohertz to tens of Megahertz. With respect to instrumentation, this means that broadband detection devices are required to accurately detect these signals.

In experimental conditions, the OA signals are broadened due to the finite temporal width of the laser pulse. The broadening is described by a temporal convolution between the solution for impulse heating $p_\delta(\boldsymbol{r}, t)$ and shape of the laser pulse $H_t(t)$:

$$p(\boldsymbol{r}, t) = p_\delta(\boldsymbol{r}, t) * H_t(t) = \int_{-\infty}^{\infty} p_\delta(\boldsymbol{r}, t - \tau) H_t(\tau) d\tau, \qquad (18)$$

where $*$ denotes the temporal convolution operator [105].

Signal strength in an experimental scenario (small-animal imaging)

Next, an estimate of the OA signal strength expected in a small animal imaging experiment is derived. A spherically shaped absorber, located within the cylinder, is considered as the source of the OA signal. Furthermore, constant and uniform illumination onto the surface of the cylinder is assumed. A diagram explaining this geometry is shown in Figure 2.3(a). The OA signal from a spherical absorber is given by Eq. (17). It depends on the initial pressure p_0, which is proportional

to the light fluence and local absorption coefficient. An estimate of the light fluence Φ can be derived from the homogenous form of the light diffusion equation (2). In cylindrical coordinates and taking into account the symmetry of the problem ($\frac{\partial \Phi}{\partial z} = 0$ & $\frac{\partial \Phi}{\partial \varphi} = 0$), it writes as follow [106]:

$$r^2 \frac{\partial^2 \Phi(r)}{\partial r^2} + r \frac{\partial \Phi(r)}{\partial r} - \frac{\mu_a}{D} r^2 \Phi(r) = 0. \tag{19}$$

This is a modified Bessel equation of the first kind, and has a solution of the type

$$\phi(r) = A I_0 \left(\sqrt{\frac{\mu_a}{D}} r \right), \tag{20}$$

where A is a constant and I_0 is the modified Bessel function of the first. Using (20) into (19) for the initial condition $\phi(R) = \phi_0$ yields

$$A = \frac{\phi_0}{I_0 \left(\sqrt{\frac{\mu_a}{D}} R \right)}. \tag{21}$$

Under assumption that the observation point lies outside the spherical absorber and the acoustic attenuation is negligible, it is possible to derive an expression for the OA pressure amplitude at position $\boldsymbol{r}$ generated by a spherical absorber with the radius a positioned at $\boldsymbol{r}_s$ within a tissue mimicking cylinder with the radius d, so that:

$$p(\boldsymbol{r}, t) = \Gamma \mu_a^s \frac{\phi_0}{I_0 \left(\sqrt{\frac{\mu_a}{D}} d \right)} I_0 \left(\sqrt{\frac{\mu_a}{D}} r_s \right) \frac{(R - v_s t)}{2R}, \tag{22}$$
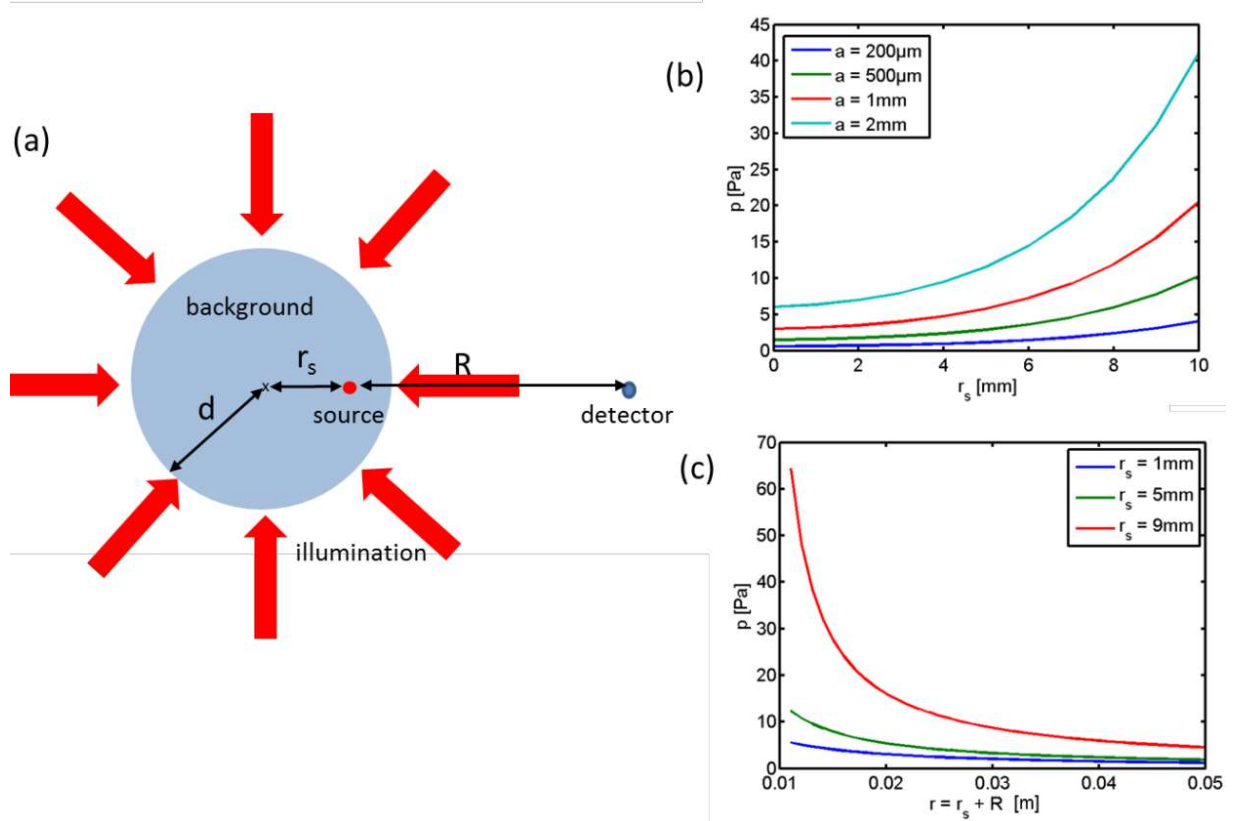
Figure 2.3 A scenario for the estimation of optoacoustic signal strength.   (a) Diagram explaining the geometry of the model: An infinite cylinder (top view) with tissue mimicking properties is uniformly illuminated from the sides. Signals are generated by a spherical absorber inside the phantom. (b) Optoacoustic pressure amplitude from the spherical optoacoustic source, detected 4 cm away of the center from the cylinder as a function of target size and distance from the center of the phantom. (c) Optoacoustic pressure amplitude for the microsphere (500 μm), for three different target positions as a function of the detector location.

Where μ_a^s is the absorption coefficient of the spherical OA source, ϕ_0 [Jm^{-2}] is the initial light fluence on the surface of the object, I_0 is the modified Bessel function of the first kind and order zero, $D(r) = \frac{1}{3(\mu_s'+\mu_a)}$ is the diffusion constant, μ_s' & μ_a are the optical absorption and reduced scattering coefficient of the background, respectively, d is the radius of the cylinder, v_S is the sound velocity and $R = |\boldsymbol{r} - \boldsymbol{r}_s|$ is the distance between the source position and detection point. We can see that the magnitude of the detected OA signal is directly related to its absorption coefficient, the thermo-acoustic efficiency given by the Grüneisen coefficient, its size and the

initial light fluence, but inversely related to the distance from the transducer and attenuated with respect to the depth.

Numerical estimations have been performed for realistic experimental values: $\Gamma = 0.25$, μ'_s=10 cm^{-1}, μ_a=0.3 cm^{-1}, μ_a^s=0.5 cm^{-1}, ϕ_0=20 mJ.cm^{-2}, $r = 4$ cm, $0.2 \leq a \leq 2$ mm, and $d = 1$ cm. Figure 2.3(b) displays the OA signal strength as a function of the distance between source and center of the phantom for different source sizes. Figure 2.3(c) displays the OA pressure amplitude for the microsphere with a diameter of 500 μm and for different detector distances. Since the OA signals are relatively weak, only a few to a few tens of Pascals are available for detection, depending on the exact location within the phantom. Signals from deep inside the phantom are approximately 8 times smaller than close to the surface. With respect to instrumentation this means that it is important to have a sensitive detection device with a sufficiently large dynamic range to be able to detect both the signals from the surface of the animal as well as the weak signal from the inside. We also see that it is important to do multisided illumination, since this increases the signal strength from structures deep inside the object (about 16%) compared to single side illumination (around 4%).

Directivity of OA signals

Due to the high velocity of light compared to sound, all of the optical absorbers in the tissue can be considered excited simultaneously, thus produce coherent pressure waves. Since ultrasound scattering in tissue is low, the coherence is preserved over long distances, causing diffraction phenomena due to the interference of the wavefronts originating at neighboring points of the source. Objects with a high aspect ratio, like blood vessels for example, emit directive radiation.

To demonstrate this behavior, the directivity pattern for OA sources with the aspect ratios of 1, 2, and 10, respectively, was calculated. The resulting wave forms were obtained by the superposition of the bipolar signals from OA point sources (see Eq. (17)). The results are displayed in Figure 2.4. The OA source is located in the image center at the coordinate (0,0). It has to be considered rotationally symmetric around its longitudinal axis. Each point in the image of the first row represents the energy of the emitted acoustic wave. The second row depicts the polar plots of the energy emitted for a distance of 2 and 40 mm. The graph was normalized to the 0° direction. Obviously, OA sources with an aspect ratio greater than 1 emit directive pressure waves. The directivity increases with increasing aspect ratio. In small animals, anatomical structures (e.g. blood vessels) are arbitrarily shaped and oriented. Therefore, depending on the shape, aspect ratio and orientation of the structure, the OA signals are emitted in a different direction. In order to be able to capture the OA signals from all the absorbers, a closed detection surface is required. With respect to designing a practical small-animal imaging system, this means that if the object is not completely surrounded with detection elements, structures may be invisible, because their emitted signals are not captured by any detection element. This is known as the *LV (PV) problem* and will be discussed in more detail later.
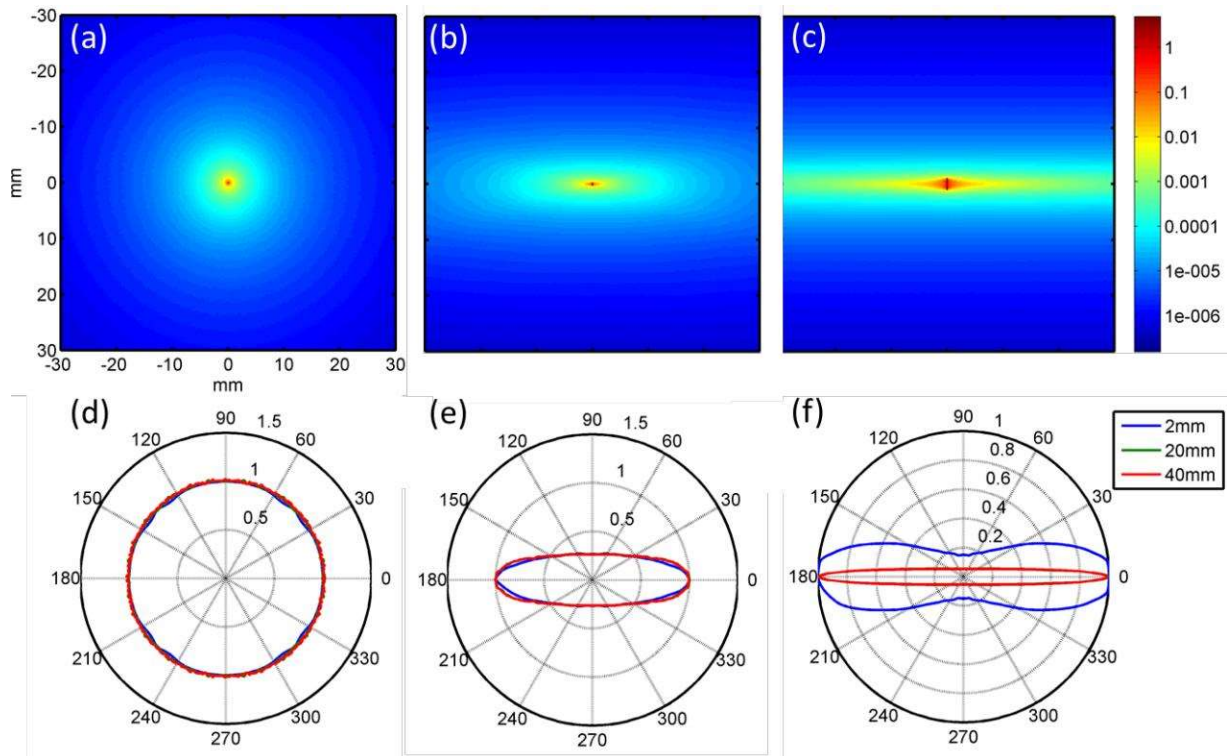
Figure 2.4 Directivity of optoacoustic signals.   Directivity maps for an optoacoustic source with an aspect ratio of 1 (a), 2 (b) and 10 (c). Each point represents the emitted energy detectable at this position. The corresponding polar plots, normalized to the value at the 0° position, are shown in the second row for distances of 2 and 40 mm, respectively.

2.2 Technical aspects of OA signal detection

2.2.1 Optical excitation

Pulse duration

The previous description of the OA phenomena has been derived under the assumption that heat and stress propagation during the excitation pulse is negligible. To ensure that these equations are valid and that the OA signals are generated efficiently, the pulse duration of the laser employed in the imaging system has to be shorter than the thermal and stress relaxation time of the sample. Expressions to estimate these thresholds have been presented (see Eqs. (10) and (11)). They depend on the targeted resolution of the system and the thermal diffusivity of the tissue. To give a

numerical example, we calculate the thermal and stress relaxation time for a previously developed system. It aims for a maximal resolution of $d_c = 150\mu m$. A typical value for the thermal diffusivity in soft tissue is $D_T = 1.3 \times 10^{-3}\text{cm}^2\text{s}^{-1}$ [65]. The corresponding values for the thermal and stress relaxation time are then $\tau_{th} \approx 170ms$ and $\tau_s \approx 100ns$, respectively. Such time-scale values can easily be achieved with modern nanosecond laser technologies. Pulse durations exceeding these thresholds would compromise the spatial solution of the system by broadening the photoacoustic signal.

Laser technologies

Various nanosecond pulsed laser technologies are available. For tomographic imaging, deep tissue penetration is desirable. Since light attenuation in tissue severely hinders the penetration of light, high pulse energies are preferential. Q-switched solid state lasers based on neodymium-doped laser crystals (e.g. Nd:YAG) can deliver 10 ns pulses with pulse energies of multiple joules in the 1 μm spectral region at a repetition rate of several Hertz [107] and are therefore very attractive for deep tissue OA imaging [103]. Since the MSOT technology employs multi-wavelength illumination, the output wavelength of the laser has to be tunable. For deep tissue imaging, the tuning range should be in the near-infrared region to benefit from the spectral window in tissue. Conversion stages, such as optical parametric oscillators (OPOs), can be employed for this purpose. The OPO technology is particularly attractive for MSOT because wavelength tuning can be done fast. It depends only on the speed with which the orientation of the parametric oscillator crystal can be changed and it allows wide tuning ranges. For the imaging of superficial structures, lower pulse energies are sufficient and additional technologies like diode-pumped dye lasers, laser diodes or

fiber lasers become suitable. With pulse repetitions rates in the order of several kilohertz, these lasers provide the potential to design fast scanning-based imaging systems [103].

Maximum permissible exposure

The key parameter for yielding good signal-to-noise ratio (SNR) is the per-pulse energy. For *in vivo* applications, however, laser safety standards have to be respected. The American National Standards Institute (ANSI) defines the maximal permissible skin exposure (MPE) for nanosecond lasers up to a repetition rate of 10 Hz as 20 mJ.cm^{-2} per pulse for wavelengths in the visible range (400 - 700 nm), which gradually increases through the near-infrared region (NIR) according to the formula [98]

$$MPE = 20 \times 10^{2^{\frac{\lambda - 700}{1000}}} \tag{23}$$

to 100 mJ.cm^{-2} at 1050 nm. For repetitive laser pulses onto the same area, the exposure limits for the average power deposition have to be met. They are 200 mW.cm^{-2} in the visible range, and gradually increase to 1 W.cm^{-2} in the NIR.

2.2.2 Detection of OA signals

Detection of OA signals is a critical component in OA imaging. For accurate detection, the detection device requires a high sensitivity; a broad detection bandwidth and a large dynamic range. Various approaches to detect the OA signals have been explored in the literature. They can be divided into two categories: piezoelectric detection and optical [103].

Piezoelectric detection

Piezoelectric detection is adopted from the well-established field of ultrasound medical imaging. It is based on the piezoelectric effect, i.e. the property of certain materials to generate a voltage difference at its surface due to a reorientation of its electrical dipoles after mechanical deformation. The voltage difference is proportional to the deformation, which enables to detect pressure variations and thus measure an acoustic field. On the other hand, since the piezoelectric effect is a reversible process, it can also be used to generate pressure waves by applying a voltage to the material [104], [108]. In ultrasound imaging this is used to send an acoustic pulse. The efficiency of the material to convert one form of energy to the other is defined by the electromechanical coupling coefficient k_t defined as the ratio of stored mechanical energy in thickness resonance mode and the total stored energy [109]. The advantage of piezoelectric detection is the high sensitivity, the flexibility to manufacture arbitrary shapes and the possibility of parallelization [110].

Piezoelectric materials

Piezoelectric materials used for OA imaging should have a high electromechanical coupling coefficient k_t (i.e. sensitivity) and acoustical impedance matched to soft tissue. Three major types of piezocomposites are generally available: ceramics, polymers and composites [104].

Ceramics, with lead-zirconate-titanate (PZT) as the most prominent representative, have a good electromechanical coupling ($k_t = 0.55$) but an acoustical impedance (Z 34 MRayl) badly matched to soft tissue (Z ~ 1.6 MRayl) [109]. As a consequence, when applied for tissue imaging, there is little energy transfer between tissue and piezoelectric material. Therefore, for tissue imaging, piezoceramics are usually used in form of a composite, i.e. piezocomposite rods embedded in a

polymer matrix to adjust the acoustic impedance to the one of tissue. By varying the ratio between the ceramic and polymer content, piezo-composites can be designed flexibly attaining high coupling efficiencies. Drawbacks are the higher production costs due to the complicated fabrication process [109].

Piezoelectric polymers such as polyvinylidene fluoride (PVDF) have also been found to be useful for biomedical applications. They have the advantage of being better matched (Z ~ 3.6 MRayl) to tissue and can easily be produced in thin layers necessary for high frequency applications. However, the electromechanical coupling is low (k_t = 0.11) which limits the transducers' sensitivity.

The Ultrasound detector

Ultrasound transducers are highly sophisticated and complex electronic instruments. The basic components of a simple single element ultrasound transducer are depicted in Figure 2.5. The most important component is the piezoelectric element. It is a resonating device which converts the pressure wave into an electrical signal. The resonance frequency is determined by the thickness material [109]

$$f_R = \frac{n v_T}{2L},$$
(24)

where v_T is the acoustic wave velocity in the piezoelectric material, L its thickness and n is an odd integer. The thinner the piezoelectric material, the higher is the resonance frequency. The two surfaces of the piezoelectric material are connected to electrodes to measure the generated voltage difference. The matching layer in front of the piezoelectric material has intermediate acoustic impedance between the one of the piezoelectric crystals and the one of tissue. Its purpose is to reduce the impedance mismatch between tissue and piezoelectric material in order to improve the transfer of acoustic energy into the transducer. The backing material serves to damp the reverberations of the piezoelectric material after excitation and therefore determines the bandwidth of the transducer. The better it is matched to the impedance of the piezoelectric material, the better is the absorption of acoustic energy and thus the better the damping of the oscillations and wider the bandwidth of the transducer. Conversely, with a mismatched backing, acoustic energy is be reflected back into the piezoelectric material, thus little acoustic energy is lost yielding ringing and a narrow bandwidth of the transducer. To increase the bandwidth of the transducer it is therefore necessary to match the backing material to the acoustic impedance of the piezoelectric material.
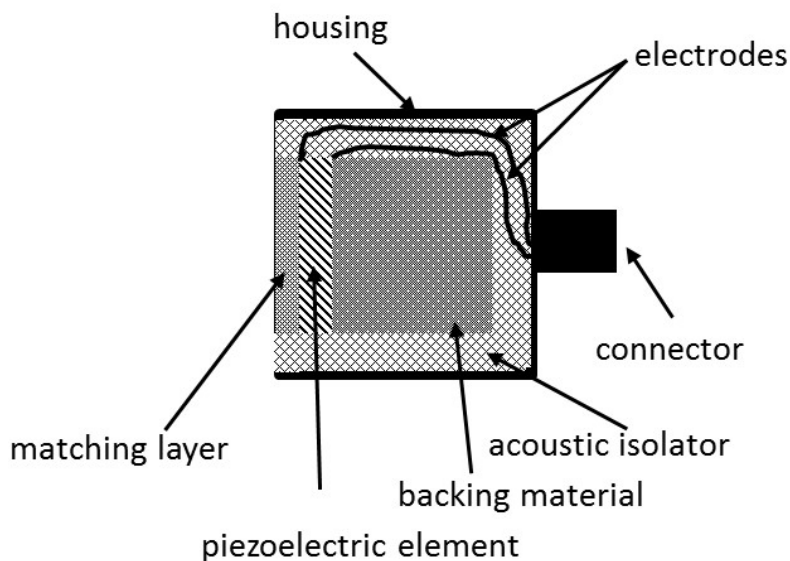
Figure 2.5 Components of a typical ultrasound transducer.

The trade-off of increasing the bandwidth is however a loss of sensitivity because most of the acoustic energy is absorbed in the backing [108], [109]. With respect to designing an OA imaging system, the technical challenge consists of finding the right balance between sensitivity and bandwidth of the transducer, in order to be able to detect the weak OA signals without much signal distortion.

The frequency characteristics of an ultrasound transducer are described in terms of central frequency [MHz] and fractional bandwidth of the central frequency [%]. A transducer with a central frequency of 5 MHz and a bandwidth of 60% has its main sensitivity between 3.5 and 6.5 MHz. Outside this spectral region, the frequency amplitude is lower than -6 dB of its maximal sensitivity.

Optical detection

Optical detection, based on optical interferometry to probe the ultrasonic displacement [111], [112] provides wide and uniform detection bandwidth and small size, which is highly interesting for OA imaging since signals distortions due to the element size and bandwidth of the detection element is significantly reduced. However, they also have a low sensitivity level, which is two orders of magnitudes less compared to piezoelectrical detection devices [113]. For that reason, optical approaches are currently only applied for imaging superficial structures [103]. Additional drawbacks are difficulties in parallelization which is desirable in order to increase the imaging speed. Optical detection devices might however be very useful for minimal-invasive imaging devices, such as intravascular imaging, where size plays an important role.

2.2.3 Electrical impulse response (EIR) of ultrasound detectors

As shown before, OA signals are generally broadband. Ultrasound detection devices on the other hand generally have a relatively limited spectral bandwidth and non-uniform frequency characteristics, resulting from the resonance properties of the piezo-element, backing and the electronics utilized [104]. They act as a band-pass filter and thus distort the OA signals. The distortion of the OA signals is a linear process and can be modeled with the electrical impulse response (EIR) of the system according to [114]:

$$p_d(\boldsymbol{r}, t) = p(\boldsymbol{r}, t) * EIR(t), \tag{25}$$

where $*$ stands for a temporal convolution, $p_d(\boldsymbol{r}, t)$ is the distorted and $p(\boldsymbol{r}, t)$ the undistorted OA signal, respectively. $EIR(t)$ represents the electrical impulse response of the detection system [115]. It describes how the detection system reacts to an impulse excitation, i.e. a source with constant frequency spectrum and infinite bandwidth. It is spatially invariant, thus the same for each OA signal and independent of the location of the source.

The distortion of OA signals due to the electrical impulse response is shown in Figure 2.6 for a spherical absorber with diameter 200 µm and 2 mm. The electrical frequency response is assumed to have a Gaussian shape, characteristic for piezoelectric detection elements [58], with a central frequency of 3 MHz and a fractional bandwidth of 90%. The distortion effect of the OA signals due to the influence of the electrical impulse response is clearly visible. Obviously, the detection bandwidth is insufficient to detect the sharp edges of the N shape of the OA signal resulting in a broadening of the signals. The part of the OA signal that decreases linearly, is associated with low-frequencies. For a small object the detection bandwidth is suited to accurately detect this part
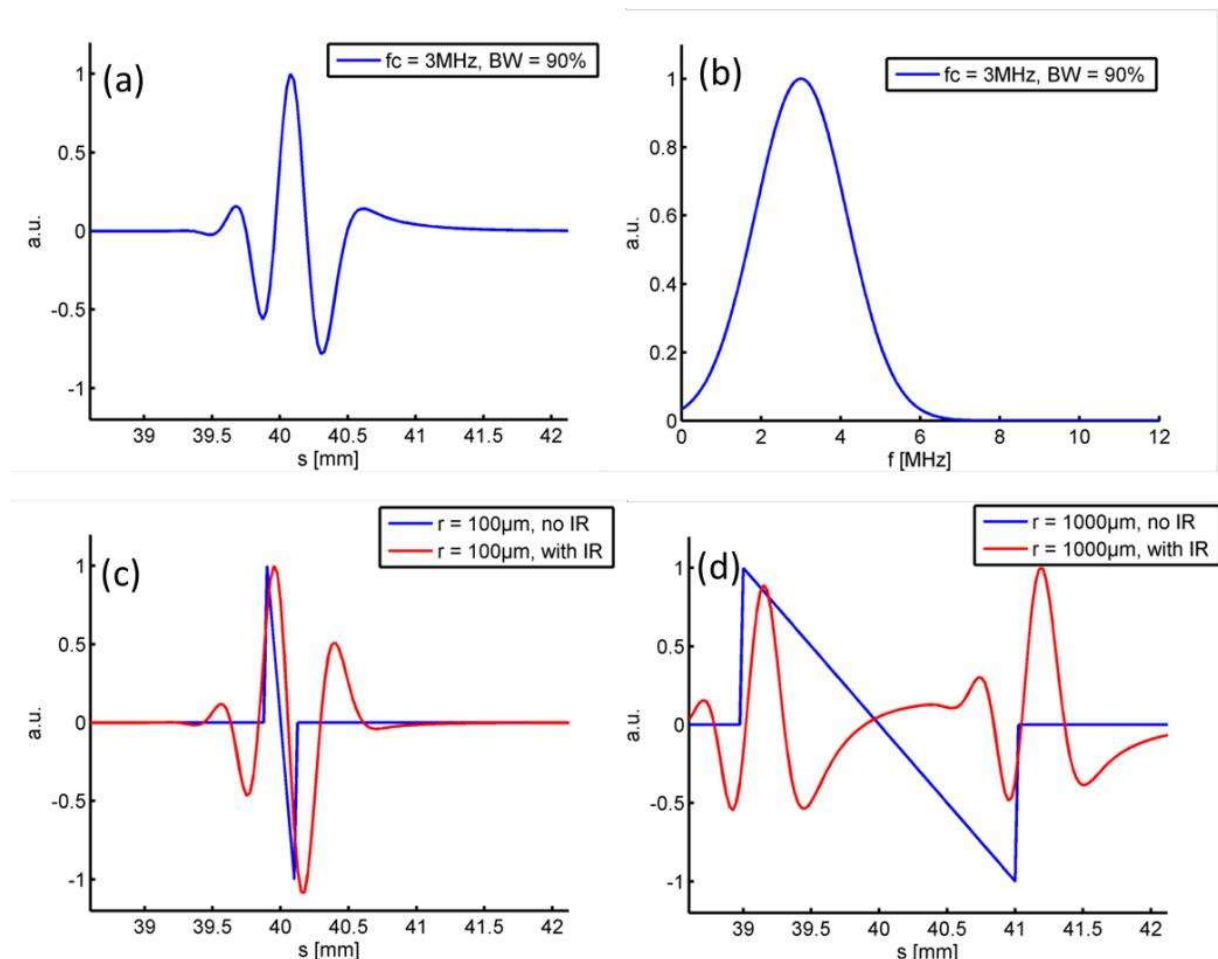
Figure 2.6 Distortion of the optoacoustic signal due to the electrical impulse response of the detection system. (a) Electrical impulse response utilized in this simulation study. (b) Depicts the Fourier transform of the electrical impulse response, which is the electrical frequency response, having a Gaussian shape with a central frequency of 3 MHz and a fractional bandwidth of over 90%. (c) Effect of the electrical impulse response on the optoacoustic signal from a spherical source with a 200 µm diameter. (d) The same on a spherical source with a 2 mm diameter.

(Figure 2.6(c)), which is however not the case for a big object (Figure 2.6(d)), where a lack of low frequencies leads to a completely erroneous representation of this part of the signal. A deconvolution approach to correct for the distortion of the OA signals due to the electrical impulse response will be discussed later.

An example for measuring the EIR experimentally

To measure the EIR of the system, the approach presented by Rosenthal *et al.* [114] was followed. It consists of generating a wideband OA signal in the focal point of the transducer, which can be achieved either by illuminating a point-like absorber with dimensions much smaller than the achievable resolution of the OA system, or by focusing the laser beam to a small spot on a highly absorbing black agar slap. The pressure wave $p_d(\boldsymbol{r}_d, \boldsymbol{r}, t)$ from a point source located at $\boldsymbol{r}$ and detected with a transducer at position $\boldsymbol{r}_d$ is given by

$$p_d(\boldsymbol{r}_d, \boldsymbol{r}, t) = p(\boldsymbol{r}_d, \boldsymbol{r}, t) * TIR(\boldsymbol{r}_d, \boldsymbol{r}, t) = p(\boldsymbol{r}_d, \boldsymbol{r}, t) * EIR(t) * SIR(\boldsymbol{r}_d, \boldsymbol{r}, t), \qquad (26)$$

where $*$ denotes the temporal convolution operator, $TIR(\boldsymbol{r}_d, \boldsymbol{r}, t)$ the total impulse response, $SIR(\boldsymbol{r}_d, \boldsymbol{r}, t)$ the spatial impulse response (discussed in more detail later), and $EIR(t)$ the electrical impulse response of the system. If the source is located at the focal point, each point of the detector surface is excited simultaneously, i.e. $SIR(\boldsymbol{r}_d, \boldsymbol{r}, t) = \delta(t)$. Moreover, the OA signal from a point source is proportional to the derivative of a delta function as seen by substituting $H_r(\boldsymbol{r}) = \delta(\boldsymbol{r})$ in the OA forward solution Eq. (16). It then directly follows from Eq. (26) that

$$p_d(\boldsymbol{r}_0, t) = \frac{\partial \delta(t)}{\partial t} * EIR(t) = \frac{\partial EIR(t)}{\partial(t)}. \qquad (27)$$

Hence, the measured photoacoustic signal from an OA point-source corresponds to the derivative of the electrical impulse response of the measurement system. To retrieve the electrical impulse response, the measured OA signal has to be integrated over time so that:

$$EIR(t) = \int\limits_0^t p_d(\boldsymbol{r}_0, t')dt'. \tag{28}$$

For the experimental measurement, a 50 μm black polyethylene microsphere (*Cospheric LLC, Santa Barbara, California*) embedded in a scattering agar phantom was used as a source to generate the impulse-like OA signal. The microsphere was black, which ensures high absorption and thus a strong OA signal. In order to avoid reflections, due to strong impedance mismatches, the phantom was made of agar with matching acoustic properties to water and had scattering properties to achieve homogeneous illumination. The microsphere was positioned in the center of rotation of the transducer array of the MSOT system so that it had the same distance from each transducer element. This enabled the simultaneous measurement of the electrical impulse response of all elements. The signals were averaged over 1000 laser pulses to increase the SNR.

Figure 2.7(a) depicts the simulated signal of a 50 μm microsphere and (b) its frequency spectrum obtained from the fast Fourier transform. Panel (c) depicts the signal after integration and (d) the
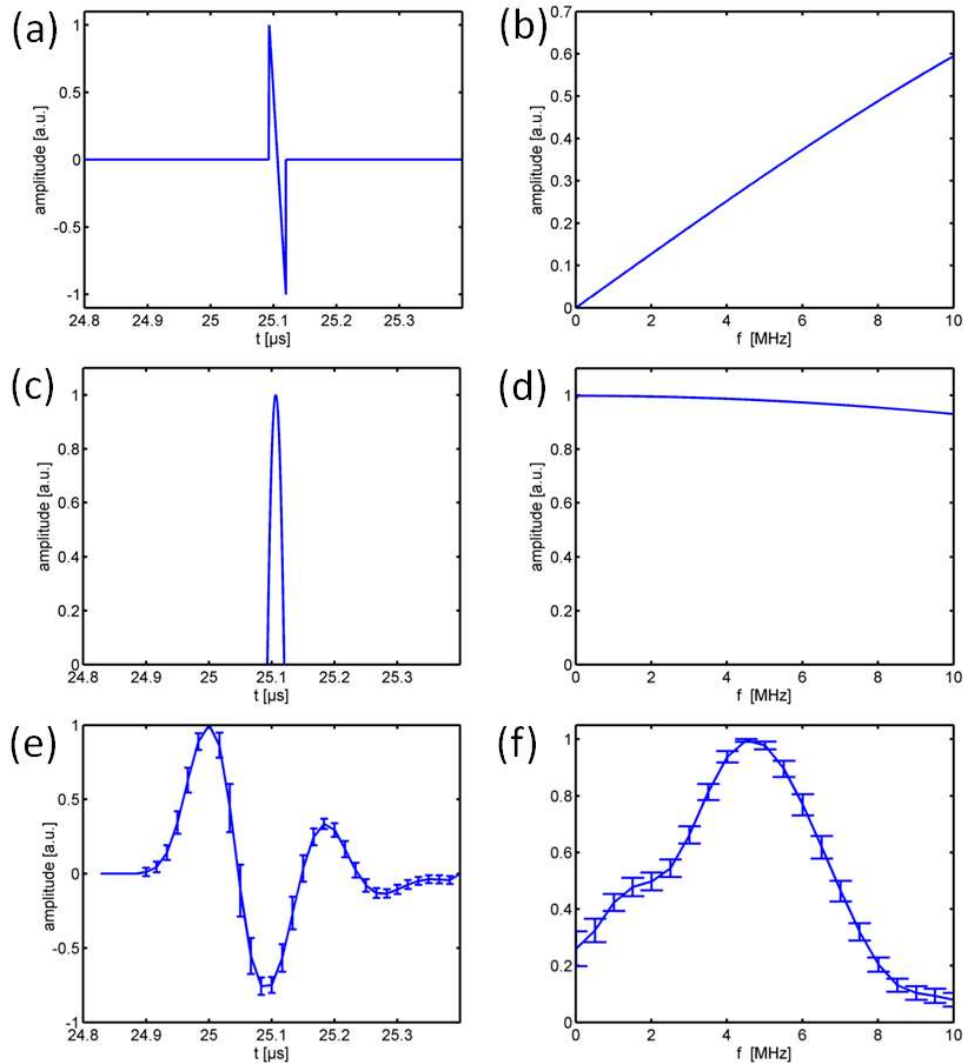
Figure 2.7 Measuring the EIR experimentally.   (a) Simulated signal of a 50 µm big spherical absorber and (b) its amplitude spectrum. (c) Simulated signal after integration and (d) corresponding amplitude spectrum. (e) Experimentally determined electrical impulse response of the detection system and (f) corresponding amplitude spectrum of the electrical frequency response.

corresponding frequency spectrum being constant within a standard deviation of 3% for frequencies up to 10 MHz. Hence for determining the EIR the microsphere is considered small enough. Panel (e) shows the mean electrical impulse response (EIR) of the system obtained by averaging the impulse responses from the 256 different transducer elements and (f) the corresponding amplitude spectrum of the electrical frequency response (EFR). The error bars describe the standard deviation between the 256 channels. The array has a central frequency of 4.7

67

MHz and a -6 dB reception bandwidth between 2.1 and 6.9 MHz, which translates into a fractional bandwidth of 97%. The -3 dB cutoff frequency is at 7.8 MHz. The variation of frequency response between the individual elements is about 3% increasing to 6% towards the low frequencies.

The retrieved values are in good correspondence with the specifications of the manufacturer (f_c = 5 MHz, BW = 55%). Differences between the individual elements are due to fabrication inaccuracies as characterized by the manufacturer. The inter-element differences are higher in the low frequency range because low frequency noise is amplified by the integration. Low frequency components in the signal are actually more prone to errors because they are weaker for small sources as seen in Figure 2.7 (b). The difference in bandwidth stems from the pulse-echo method utilized by the manufacturer. As explained in [104], the spectral bandwidth determined by the pulse-echo method is the convolution of the send-and-receive spectra, which are the same, i.e. $EIR_{p-e} = EIR * EIR = EFR^2$. The convolution of EIR with itself, effectively squares the frequency of the transducer. On the other hand, the method employed here considers only the receive spectrum, thus the difference in the measured OA bandwidth and the one determined by the manufacturer. This also shows the importance of determining the EIR in receive mode when it is to be used to correct signal distortions in OA imaging scenarios.

Correction for the electrical impulse response

To reverse the signal distortion due to the detection system, the detected signals have to be deconvolved with the EIR. Theoretically, this can be done in the Fourier domain by division with the electrical frequency response (EFR) which is the Fourier transform of the EIR. Using experimental data this might be problematic. Due to the limited detection bandwidth, noise in the

signal can be increased significantly. To avoid the amplification of noise, *Wiener* deconvolution can also be used. In the frequency domain, Wiener deconvolution is defined as

$$P(f) = \left[\frac{1}{EFR(f)} \cdot \frac{|EFR(f)|^2}{|EFR(f)|^2 + N} \right] P_d(f), \tag{29}$$

where $P(f)$ is the Fourier transform of the deconvolved OA signal, $P_d(f)$ the Fourier transform of the detected signal, $EFR(f)$ the frequency response, and N the noise floor of the detection system. The noise term in the denominator attenuates the scaling of noise in the data due to low system sensitivity [98]. Alternatively, for IMMI reconstruction (discussed in more detail later), it is possible to include the EIR into the forward model by convolving the individual columns of the model matrix with the EIR [116]. This has the advantage that no additional preprocessing of the signals is necessary when the forward matrix is calculated (except from signal filtering). However, the Wiener deconvolution approach has the advantage that it can be used for both BP reconstructions and IMMI inversions. In addition, convolving the forward model with the electrical impulse response reduces its sparseness, thus increases the matrix size and slows down the inversion, which is faster for sparser matrices.

2.2.4 Spatial impulse response (SIR) of finite-size ultrasound detectors

Detection of OA signals with detectors having a finite size leads to a spatial averaging and a distortion of the OA signals because different points $\boldsymbol{r}_d$ on the surface S of the transducer detect the OA signal $p_d(\boldsymbol{r}, t)$ at different time points [117], according to

$$p_d(t) = \int_S p(\boldsymbol{r}'_d, t) dS(\boldsymbol{r}_d'). \tag{30}$$

It was shown in [118] for an OA point source $p_{ps}(r'_d, r, t)$ located at r and detected with a detector located at r_d, the surface integral in Eq. (30) can be expressed in form of a 1D convolution

$$\int_S p_{ps}(r'_d, r, t)dS(r'_d) = SIR(r_d, r, t) * p_{ps}(r_d, r, t) \tag{31}$$

where

$$SIR(r_d, r, t) = \frac{1}{2\pi}\int_S \frac{\delta\left(t - \frac{|r'_d - r|}{v_s}\right)}{|r'_d - r|}dS(r'_d) \tag{32}$$

is the spatial impulse response (SIR) of the transducer element located at r_d [104]. The SIR characterizes the distortion of the pressure profile from an OA point source induced by the detector aperture. Convolved with the electrical impulse response (EIR), the spatial impulse response is termed total impulse response (TIR). TIR can be used to visualize the anisotropic detection sensitivity of the transducer (i.e. its sensitivity field), arising from its finite detection surface and finite detection bandwidth. Generally this is accomplished by plotting the amplitude of the total impulse response as a function of the geometrical coordinates [104].

Figure 2.8 displays the OA signals from three spherical absorbers measured with a focused transducer as well as the corresponding spatial impulse response. The relative location of the sources is shown in (a). The size and curvature radius of the focused transducer was 15 mm x 1 mm and 40 mm, respectively. The positions of the point sources are the following, in each case with coordinates given in mm: P1 (0,0,0), P2 (0,0,-20) and P3 (0,-5,0). The mechanical focal point
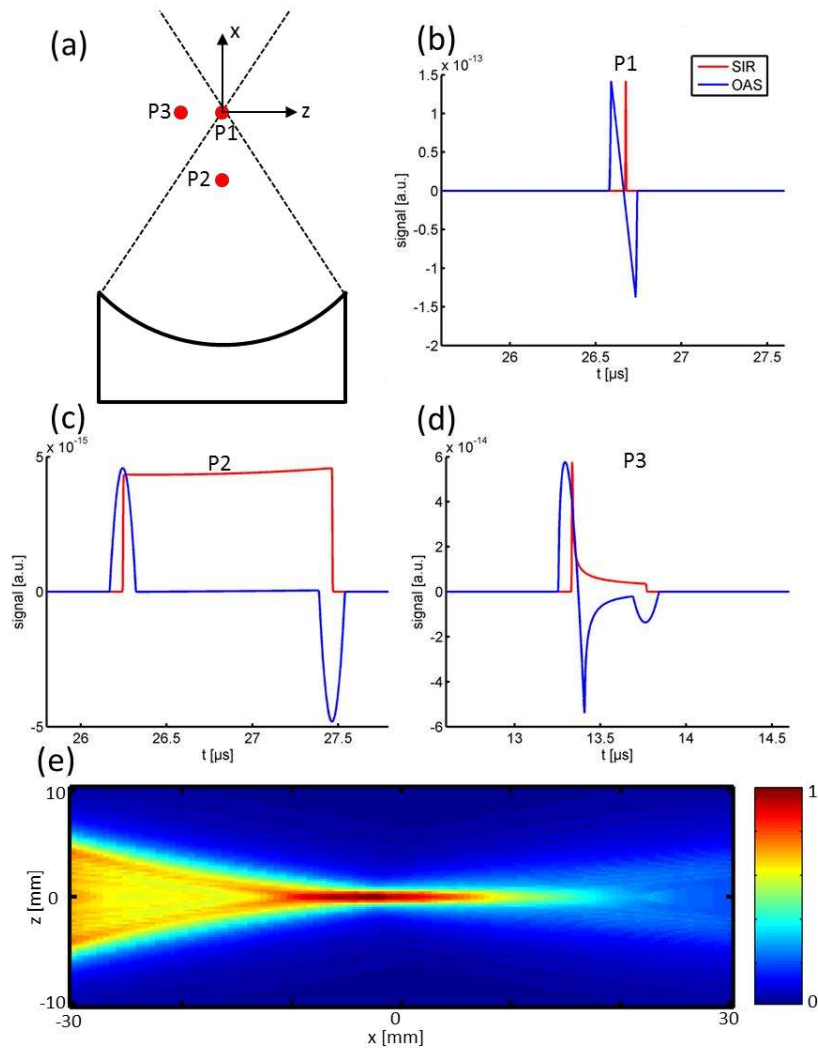
Figure 2.8 Optoacoustic signals measured with a focused detector for different source positions. (a) Source positions for which the signal was calculated. (b) Optoacoustic signal (blue line) and spatial impulse response (red line) for the source position "P1". (c) Source position "P2" and (d) source position "P3": The influence of the spatial impulse response distorts the optoacoustic signal outside the focal point. (e) Depicts the sensitivity field of the transducer.

of the transducer is located at (0,0,0). If the source is located in the focal point (i.e. P1) then the acoustic wave arrives at each surface point of the transducer at the same time. Thus, the measured signal is not distorted and duration of the measured signal the shortest. The spatial impulse response in that case is a delta function, like shown in (b). For source positions outside the focus, the detected signals are stretched in time and distorted, which is due to the asynchronous arrival of the pressure wave at the individual points of the transducer surface, as in panels (c) and (d). The

71

sensitivity field of the transducer is depicted in (e). It was obtained by plotting the amplitude of the TIR versus its geometrical coordinates. The EIR assumed had a Gaussian shape with a central frequency of 3 MHz and a bandwidth of 90%, as depicted before in Figure 2.6(b).

2.2.5 Signal-to-Noise ratio (SNR) of an OA imaging system

When designing an OA imaging system, it is important to achieve high signal-to-noise ratio (SNR), since it determines the system sensitivity and thus the detectability of an OA absorber. The SNR depends on various parameters. An expression to estimate the SNR in an OA image as a function of the individual parameters writes as [64]:

$$SNR \sim \frac{S \gamma A \sqrt{PM}}{N},$$ (33)

where S is the magnitude of the OA signal arriving at the detector, γ the ultrasonic detector sensitivity, A the detection aperture of the detector, P the number of tomographic projections used in the reconstruction, M the number of signal averages, and N the noise floor of the system. To achieve high SNR, it is therefore important to increase the magnitude of the OA signal arriving at the detector. On the one hand, this can be achieved by optimizing the light delivery, since the generated OA signal is proportional the light fluence. On the other hand, by minimizing the source-detector distance, the OA signals are attenuated as a function of the distance propagated.

Another way to improve SNR is increasing the detector sensitivity, enlarging the detection element and decreasing the noise floor of the system. Further improvements can be achieved by signal averaging and increasing the number of tomographic projections used in the reconstruction. However, this increases the SNR only as a function of their square root. It has to be noted that

some of these measures have a negative effect on the imaging performance and are therefore less desired. For instance, signal averaging prolongs the imaging time and hinders real-time applications. Large detectors compromise the lateral resolution when standard reconstruction methods that do not take the shape of the detector into account are used (e.g. the BP algorithm). Hence, from a practical imaging perspective, it is more desirable to maximize the OA signal arriving at the transducer, to reduce the noise floor of the system and/or to increase the detection sensitivity, than it is to average signals or use large detectors.

3. ALGORITHMIC & TECHNICAL ASPECTS OF OA IMAGE FORMATION

3.1 Focused-transducer-based reconstruction techniques

The goal of OA imaging is to reconstruct the absorbed energy distribution based on a set of measured OA signals. The easiest way to achieve this is using a spherical focused detection element. It has a narrow acceptance angle and can in first approximation be considered as being only sensitive to signals originating within a 1D line along its acoustic axis. Figure 3.1 (a (first column)) depicts the sensitivity field of such a spherical transducer. Since the detected signals are time-resolved, they can be regarded as 1D depth images (A-scan). Thus, the 3D reconstruction problem is reduced to 1D. The location of the OA source along the acoustic axis of the detector can be identified exactly from the time of arrival of the OA signals, if the sound speed in the propagation medium is known. To form an OA image, the transducer is scanned over the sample to acquire a set of 1D depth images which are then combined to obtain a 2D or 3D image. This image formation technique is frequently used in the field of photoacoustic microscopy. Implementation where this technique is applied can be found in [49], [119], [120]. It has the advantage that the detected pressure signals can be directly mapped onto the image space without computational reconstructions.

Similarly, the reconstruction problem can be reduced in first approximation to 2D by using cylindrically-focused transducers. These kinds of transducers have a wide reception angle in one direction and a narrow one perpendicular to it, along the focused direction. In first approximation, they can be considered as only being sensitive to signals originating from a 2D plane. Although the detected signals are time resolved, it is not possible to identify the exact location of the OA source. It can be located everywhere on the arc with the radius $r = ct$, surrounding the detector position. To form an image, multiple projections need to be acquired on a circle around the object and inverted using 2D reconstruction algorithms, two of which are presented in the next section. Different slices can be reconstructed individually. A 3D image is then obtained by stacking these 2D slices. An example of such implementation can be found in reference [64]. The advantage of this quasi-2D approach is that for a small number of detectors it can achieve high in-plane
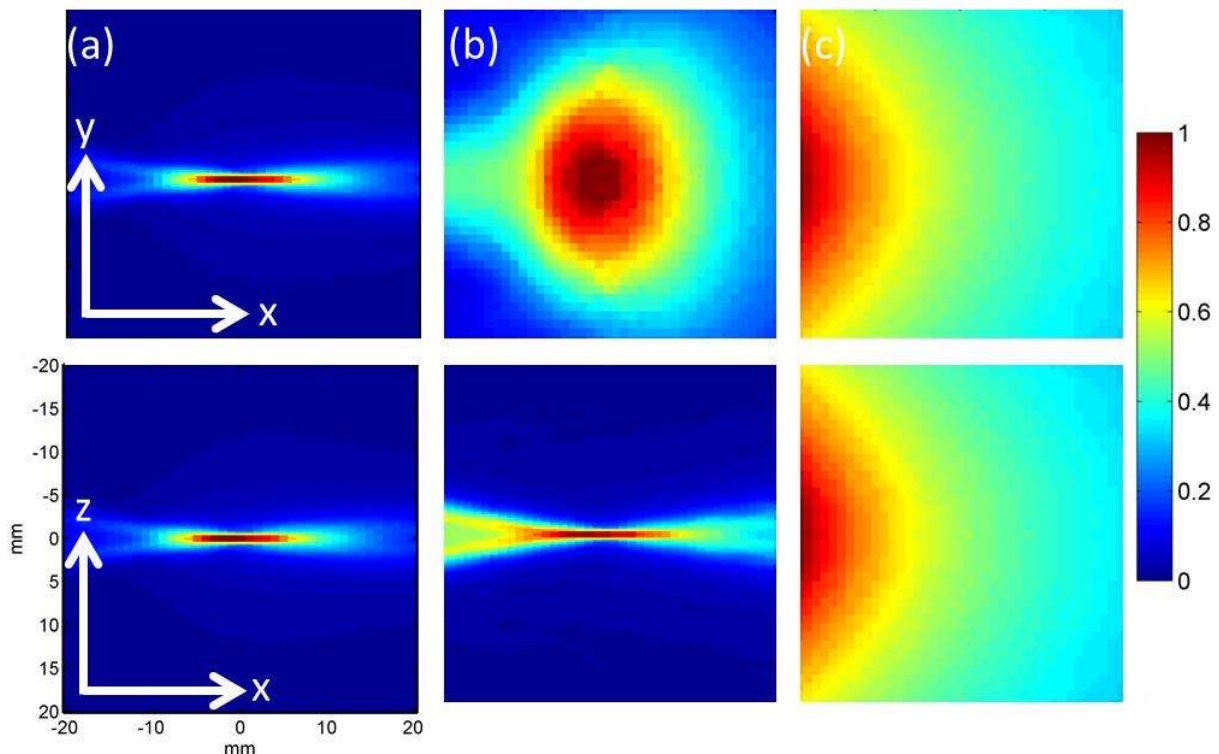
Figure 3.1 Sensitivity fields for different focus types.   (a (*first column*)) a spherically-focused transducer with an element size of 15 mm x 15 mm, (b (*second column*)) a cylindrically-focused transducer with an element size of 0.5 mm x 15 mm, and (c (*third column*)) an unfocused transducer with an element size of 0.5 mm x 0.5 mm. The transducer is located at position (-40,0,0) in mm; The radius of the element curvature is 40 mm.

resolution, good sensitivity due the large area of focused detectors and thus, real-time imaging performance.

Finally, unfocused transducer elements with a large angle of acceptance generally have a small element size. They detect acoustic signals originating from a large volume in the tissue. As a result, 3D computed reconstruction algorithms are needed to obtain an image. The tomographic dataset is either acquired along a cylindrical or spherical surface surrounding the sample, or along an infinitely long 2D plane (Figure 3.2(a)). An implementation of such a system can be found in [121], [122].

3.2 OAT image reconstruction approaches

Computed reconstruction techniques use mathematical techniques to reconstruct an image from the set of measured OA signals. They are typically based on simple delay-and-sum beamforming techniques [123], also known as *synthetic aperture techniques*, or on more rigorously derived analytical formulas related to the spherical Radon transform. They can be implemented in the spatio-temporal domain or the Fourier domain [124], [125], and exist for several detection geometries (planar, spherical, or cylindrical), as depicted in Figure 3.2. They are typically referred to as *the BP formula*, because they are based on back-projecting the time-resolved OA signals onto spherical shells and summing them up in order to form an image. These formulas are exact under ideal conditions, i.e. when the wavefront is detected by an infinite number of omnidirectional infinitely broadband point detectors distributed on an infinite planar, closed spherical, or infinitely long cylindrical detection surface [125]. In addition, algebraic or MB inversion schemes [116], [126], [127] have been suggested as more accurate alternatives to BP algorithms in non-ideal

detection scenarios. These methods are based on numerically modeling the OA forward problem and using that model in an inversion algorithm to reconstruct the image. In contrast to BP algorithms, MB schemes can explicitly take into account experimental characteristics which deviate from ideal propagation and detection conditions and can also be applied to arbitrary detection geometries.
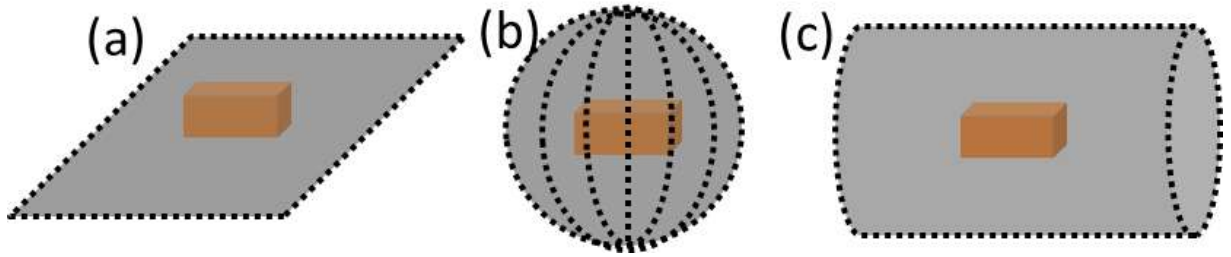
Figure 3.2 Three ideal detection geometries for optoacoustic tomography.   (a) a planar detection geometry in which the optoacoustic signals are detected along an infinitely long planar detection surface, (b) a spherical detection geometry in which the optoacoustic signals are detected on a spherical surface completely enclosing the sample and (c) a cylindrical detection geometry in which the optoacoustic signals are detected along an infinitely long cylindrical surface enclosing the sample.

3.2.1 The BP algorithm

The BP algorithm [125] is a closed-form time-domain solution to the OA equation (12) under assumption of thermal and stress confinement and delta heating. For a spherical or cylindrical detection geometry, it writes as

$$H_r(\boldsymbol{r}) = \frac{1}{\Gamma \Omega_0} \int_{\Omega_0} b(\boldsymbol{r}_0, \bar{t} = |\boldsymbol{r} - \boldsymbol{r}_0|) d\Omega_0, \tag{34}$$

where

$$b(\boldsymbol{r}_0, \bar{t}) = 2p(\boldsymbol{r}_0, \bar{t}) - 2\bar{t}\frac{\partial p(\boldsymbol{r}_0, \bar{t})}{\partial \bar{t}} \tag{35}$$

is the BP term for detection position $\boldsymbol{r}_0$ which is backprojected onto spherical shells centered at $\boldsymbol{r}_0$ and

$$d\Omega_0 = \frac{dS_0}{|\boldsymbol{r} - \boldsymbol{r}_0|^2} \frac{\boldsymbol{n}_0^S(\boldsymbol{r} - \boldsymbol{r}_0)}{|\boldsymbol{r} - \boldsymbol{r}_0|} \tag{36}$$

is the solid angle element subtended by the detection element dS_0 with respect to the reconstruction point P at position $\boldsymbol{r}$. $H_r(\boldsymbol{r})$ is the deposited energy, $\boldsymbol{n}_0^S$ is a vector pointing outwards perpendicular to the detection surface S_0. Ω_0 is the solid angle of the whole measurement surface, and for spherical and cylindrical geometries $\Omega_0 = 4\pi$.

The preclinical imaging system used frequently in our research group (*MSOT inVision*) uses a 2D circular detection geometry where the detectors are cylindrically-focused and lie in the imaging plane. To reconstruct in this scenario, a modified 2D BP formula is used [128] which is defined as

$$H_r(\boldsymbol{r}) = \frac{r_0^2}{2\pi\Gamma v_s^2} \int_{\theta_0} d\theta_0 \frac{1}{t^2} \left[p(\boldsymbol{r}_0, t) - t\frac{\partial p(\boldsymbol{r}_0, t)}{\partial t} \right]_{\left\{ t = \frac{|\boldsymbol{r} - \boldsymbol{r}_0|}{v_s} \right\}}. \tag{37}$$

The t^{-2} weighting comes from the solid angle term which is proportional to the square of the distance between the receiving element dS_0 and the point P, thus leads to a compensation factor of t^{-2}. The solid angle weighting is neglected because it had no visible effect on the reconstruction and only increased the reconstruction time.

The BP formulae are very convenient for OA image reconstruction. Due to their simplicity they are easy to implement, memory efficient and fast. In the real-time MSOT system, these formulas are used for real-time reconstructions. Although not being exact in the presented conditions, they are very useful for detecting the shape and position of the absorbers and for assessing parameters such as speed of sound and radius of rotation. On the downside, for 2D geometries, i.e. where all detectors and OA sources are located in one plane, they suppress slowly-varying image

components associated with the light fluence or big objects and accentuate fast changes in the image, i.e. object boundaries. In addition, BP reconstructions in non-ideal detection geometries often show negative optical absorption values which have no physical meaning [116]. Such drawbacks are largely overcome by the 2D MB reconstruction algorithm discussed in the next section.

3.2.2 The interpolated matrix MB inversion (IMMI)

This inversion method [116] is a MB reconstruction technique for OA image reconstruction in a 2D geometry, i.e. where all the OA sources and detectors are located in one plane. It employs a discretized semi-analytical time domain solution of the OA wave equation (12) and can be written in form of a matrix relation as:

$$\boldsymbol{p} = \boldsymbol{M}\boldsymbol{z}, \tag{38}$$

where $\boldsymbol{p}$ represents the OA signals measured at different positions (projections) and instants arranged as a column vector. The column vector $\boldsymbol{z}$ contains the originating OA image on the defined grid, i.e. values of the heat deposition. $\boldsymbol{M}$ is the acoustic forward-model matrix, it is sparse and does not depend on the imaged object, but only on the experimental acquisition geometry. $\boldsymbol{M}$ is calculated by interpolating for coordinates in-between the grid points in order to be able to integrate over arcs, according to formula (16). For a fixed acquisition geometry, $\boldsymbol{M}$ has to be calculated only once and can be reused for consecutive reconstructions.

The OA image is obtained by inverting the matrix relation in (38). A common method of doing this is the minimization of the *mean square error (MSE)*:

$$z = argmin\|\boldsymbol{p} - \boldsymbol{M}\boldsymbol{z}\|_2^2, \tag{39}$$

where $\| \ \|_2^2$ is the l_2 norm. In Ref. [116], two methods could be used to solve Eq. (38): the *Moore-Penrose pseudoinverse* [129] and *the LSQR algorithm* [130]. The pseudoinverse of the matrix $\boldsymbol{M}$ is given by

$$\boldsymbol{M}^{\dagger} = (\boldsymbol{M}^T\boldsymbol{M})^{-1}\boldsymbol{M}^T. \tag{40}$$

To reconstruct the image, the measured OA signal is then multiplied with the pseudoinverse matrix, i.e.

$$\boldsymbol{z}_{sol} = \boldsymbol{M}^{\dagger}\boldsymbol{p}^T. \tag{41}$$

The advantage of using the pseudoinverse approach is that it does not depend on the measured data but is determined only by parameters of the experimental setup, e.g. the position of the sensors employed with respect to center of rotation, the sampling resolution, etc. Therefore, given a rigid measurement configuration, the pseudoinverse $\boldsymbol{M}^{\dagger}$ may be pre-calculated, thus leading to a real time inversion procedure which involves only the product operation of Eq. (41). The disadvantage of this approach is that in order to perform the inversion, the entire matrix $\boldsymbol{M}$ needs to be stored in the computer's memory, which could lead to challenging memory utilization, especially for high resolution reconstructions.

The computational requirements for image inversion faced when using the pseudoinverse approach can be mitigated by the LSQR algorithm [130], which capitalizes on the sparse nature of $\boldsymbol{M}$. This algorithm avoids matrix-matrix operations, but instead multiplies vectors by the matrix and operates on the resulting vectors. In this way, a sequence of approximate solutions $\boldsymbol{z}_1, \boldsymbol{z}_2, \ldots, \boldsymbol{z}_n$ to the problem is attained which minimize the residual error

$$R = \|\boldsymbol{Mz} - \boldsymbol{p}\|. \tag{42}$$

As the number of iterations increases, the algorithm converges to a solution which is expected to be close to the original image.

The high accuracy achieved by the forward model allows data inversion without regularization when full 360° tomographic views are available. More importantly, the model eliminates a variety of image artefacts associated with conventional BP algorithms, such as negative image values and other quantification artefacts, and overall provides superior accuracy and image fidelity in a 2D reconstruction scenario [116].

3.3 Spatial resolution of an OAT system

The width of OA signals in the time domain scales with the size of the OA source. Ultimately, the limiting factor for the achievable resolution is the maximally detectable frequency. But it also depends on other factors such as duration of the laser pulse, detection geometry, size, shape and number of the transducer elements and image formation technique [123]. The preclinical MSOT imaging system uses a cylindrically focused transducer array for 2D cross-sectional imaging. Volumetric images can be obtained by stacking the individual 2D slices. The in-plane resolution therefore depends mainly on the reconstruction technique, while the in-elevation resolution depends on acoustic focusing.

3.3.1 In-plane resolution achieved by the reconstruction technique

The resolution of an imaging system can be assessed by the point spread function (PSF) which describes how the system represents an elementary volume. Xu *et al.* [131] derived an expression to estimate the bandwidth-limited resolution of an imaging system in an idealized detection scenario (i.e. full view detection, point detectors, continuous spatial sampling and constant sound speed), based on the full-width half-maximum (FWHM) of such a point spread function (PSF):

$$R_{bw} \approx \frac{0.8 v_s}{f_{co}}, \tag{43}$$

where R_{bw} is the bandwidth-limited resolution, v_s the sound speed, and f_{co} the cut-off frequency of the transducer. This resolution is spatially invariant. Real ultrasound transducers however have a finite-size detection aperture rather than a point. As shown before, this adds an extra spatially-variant broadening of the OA signals, which is generally not taken into account in standard OA reconstruction algorithms, like the BP algorithm. Hence, the spatial resolution of the OA imaging system gets additionally degraded perpendicular to the acoustic axis of the transducer, which is referred to as the lateral direction. Xu *et al.* also derived an expression to estimate this degradation by the lateral extension of the PSF. The axial extension of the PSF is negligible compared to the lateral blurring. In a spherical or circular scanning geometry for an unlimited detection bandwidth and a detector with the same curvature properties as the detection surface, it is given by

$$R_{ap}(r) \approx \frac{r}{r_0} D, \tag{44}$$

where R_{ap} is the aperture-limited resolution, r the distance between the point source and the center of the scan circle, r_0 the radius of the scan circle, and D the dimension of the detector.

To characterize the spatial resolution in a tomographic system, one distinguishes therefore between the axial and the lateral resolution. The axial resolution is the resolution along the acoustic axis of each transducer intersecting the center of rotation of the detection surface (or arc in 2D). It depends principally on the detection bandwidth of the transducer, i.e.

$$R_{ax} = R_{bw}. \tag{45}$$

The lateral resolution is the resolution perpendicular to the acoustic axis of the transducer. It is spatially variant, and depends both on the bandwidth and the aperture of the transducer element

$$R_{lat}(r) = \sqrt{R_{bw}^2 + R_{ap}(r)^2}. \tag{46}$$

The more the source approaches the center of rotation of the transducer array, the more the lateral resolution improves until it is only bandwidth limited. An example of spatially-variant PSFs is shown in Figure 3.3.
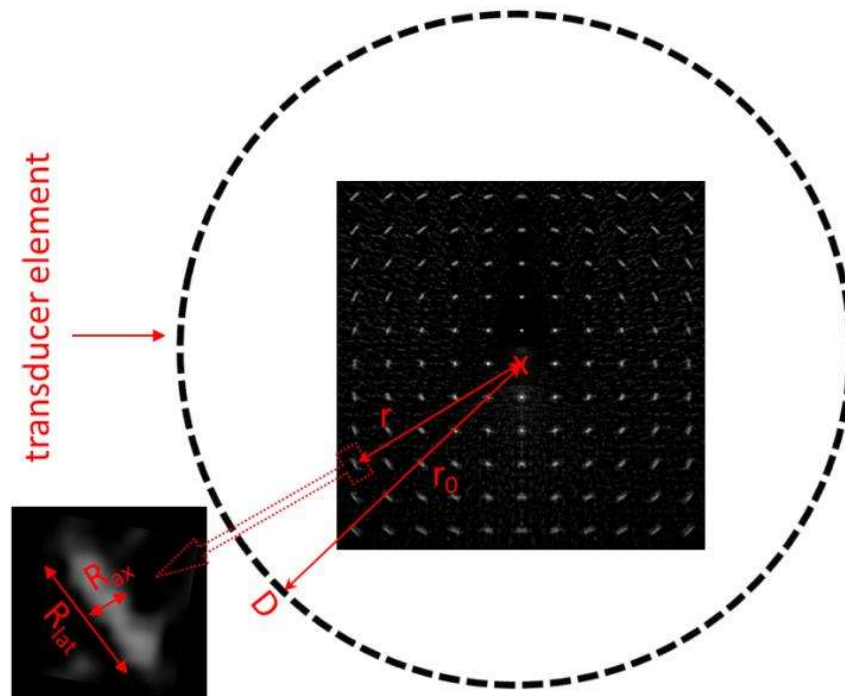
Figure 3.3: Point spread functions (PSFs) in an OAT system. The dimension of the PSF in axial direction, i.e. along a radial line through the center of the detection arc, is constant for each position. Perpendicular to it, the PSFs elongates the farther it is located from the center of the detection arc.

3.3.2 Elevation resolution achieved by acoustic focusing

The spatial resolution in a focused detector-based setup is determined by the focusing capacities of the detector which, beside the shape of the detection aperture, depends on the frequency of the detected signal. The sensitivity fields of the transducers could be obtained by calculating the SIR with the ultrasound simulation package *Field II* [132], filtering it to the desired frequency range and plotting the amplitude as a function of its spatial coordinates. Figure 3.4 depicts the sensitivity field of a cylindrically-focused transducer for three different frequencies (1, 3 and 5 MHz). The point with the coordinates (0,0) mm corresponds to the geometrical focus of the transducer. Focusing restricts the sensitivity of the transducer to a smaller area. The area of maximized sensitivity is stretched along the acoustic axis of the transducer. To characterize the sensitivity field one refers to the -6 dB focal zone, i.e. the area within which the pressure amplitude drops to half its value. This defines the area of effective imaging. The width of the focal area determines the slice thickness which can be achieved; the length determines the monitoring depth. We see the strong frequency dependence of the focusing ability of the transducer. The higher the frequency of the signal, the better is the focusing and therefore the achievable resolution.

A formula to estimate the width W and length L of the sensitivity field for cylindrically-focused transducers as a function of the characteristic frequency f_c, defined as the $1/e$ level in the spectrum of the detected signals and the aperture angle θ, was derived in [133]. The formulae are

$$L = \frac{1.1 v_s}{f_c(1 - \cos(\frac{\theta}{2}))}, \tag{47}$$

and

$$W = \frac{0.5v_s}{f_c \sin(\frac{\theta}{2})}, \tag{48}$$

where v_s is the sound velocity in the medium. The formulae show that the width and length of the focal region decrease with an increasing aperture angle and increasing characteristic frequency. This trade-off between resolution and monitoring depth is generally a major challenge in designing a focused detector-based imaging system.
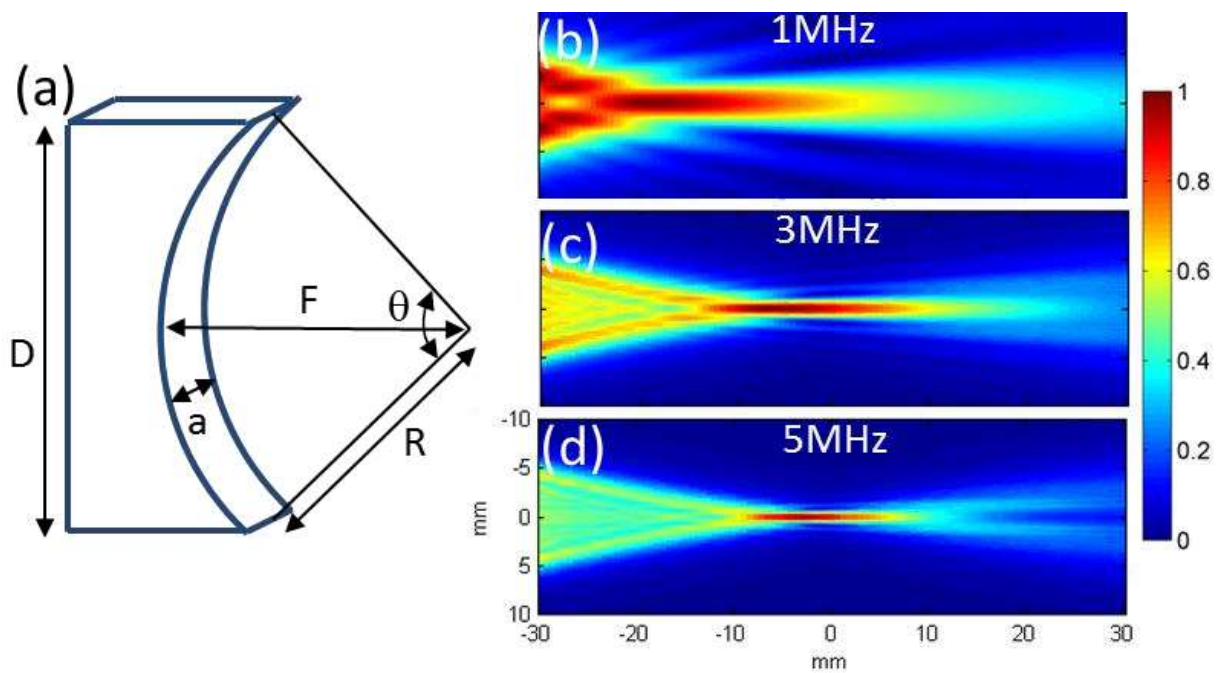
Figure 3.4 Sensitivity fields for cylindrically-focused detection elements.   (a) Illustration of the geometry. (b) Sensitivity field for a frequency f = 1 MHz, a focal length F = 40 mm and an aperture size of D = 15 mm and a = 1 mm. Sensitivity field of the same detector geometry at (c) a frequency of 3 MHz and (d) at 5 MHz. The focal point is located at (0,0) mm.

3.4 Effects of a LV detection geometry

Exact OA reconstructions require detection of the photoacoustic signals on a closed detection surface around the object [123]. In many practical imaging implementations, this cannot be achieved due to constraints like limited access or cost. OA imaging systems, for instance, generally

employ water as matching medium between the surface of the imaged object and the acoustic detector. In order to be able to acquire a complete data set, the object has to be entirely immersed in water. Some *in vivo* imaging applications however, especially whole-body small-animal imaging, might allow only partial immersion of the animal into water, resulting into a restricted detection surface. This, combined with the directivity of OA signals, might render some structures within the object undetectable (invisible), while other structures are highly defined. This is known as the *limited-view* (LV) or *partial-view* (PV) problem. The condition, under which an object is visible in a given detection geometry, has been derived before in [134]. Accurate boundary detection requires that, for each boundary point, the normal line to the boundary's defining curve intersects the detection curve (or line for scanning geometries) in at least one point. Points without such a normal line intersecting the detection curve are invisible to such detection geometry, because the wavefront is not detected and therefore will be blurred in the reconstruction.

The blurring effect is demonstrated in Figure 3.5(a) for a 2D circular detection geometry, in which a simulated round phantom with rectangular insertion is imaged. For this demonstration, OA signals were simulated using the *k-wave* OA simulation toolbox [135]. The simulation grid had a size of 802x802x5 voxels and each voxel a size of 100x100x100 μm^3, thus supporting frequencies up to 7.5 MHz. Images were reconstructed with the 2D IMMI algorithm using 720 tomographic projections uniformly distributed on the detection arc. The detection arc, denoted by the blue solid curve, defines a "visibility zone", shown in gray, in which the boundary of the imaged object always fulfills the detection criterion, and thus can be accurately reconstructed [134]. Sections of the boundary lying outside the detection region, i.e. in the "invisibility zone", may be still reconstructed subject to fulfilling the detection criterion. The boundary sections which can be

accurately reconstructed are marked with a solid red line. Figure 3.5(b) to (f) show the IMMI reconstruction obtained for the phantom for different detection arcs (360°, 240°, 180°, 140°, 90° respectively). The reconstructions clearly show the blurring effect of the object's boundary segments which do not fulfill the detection criterion. The blurring is worse for smaller detection arcs. So, MB reconstructions require specific regularization techniques to address such problem (as discussed later). With respect to designing an imaging system, the LV problem implies that the detection arc should be as long as possible and the sample should be positioned in the "visibility zone" to maximize the accuracy of the reconstruction.
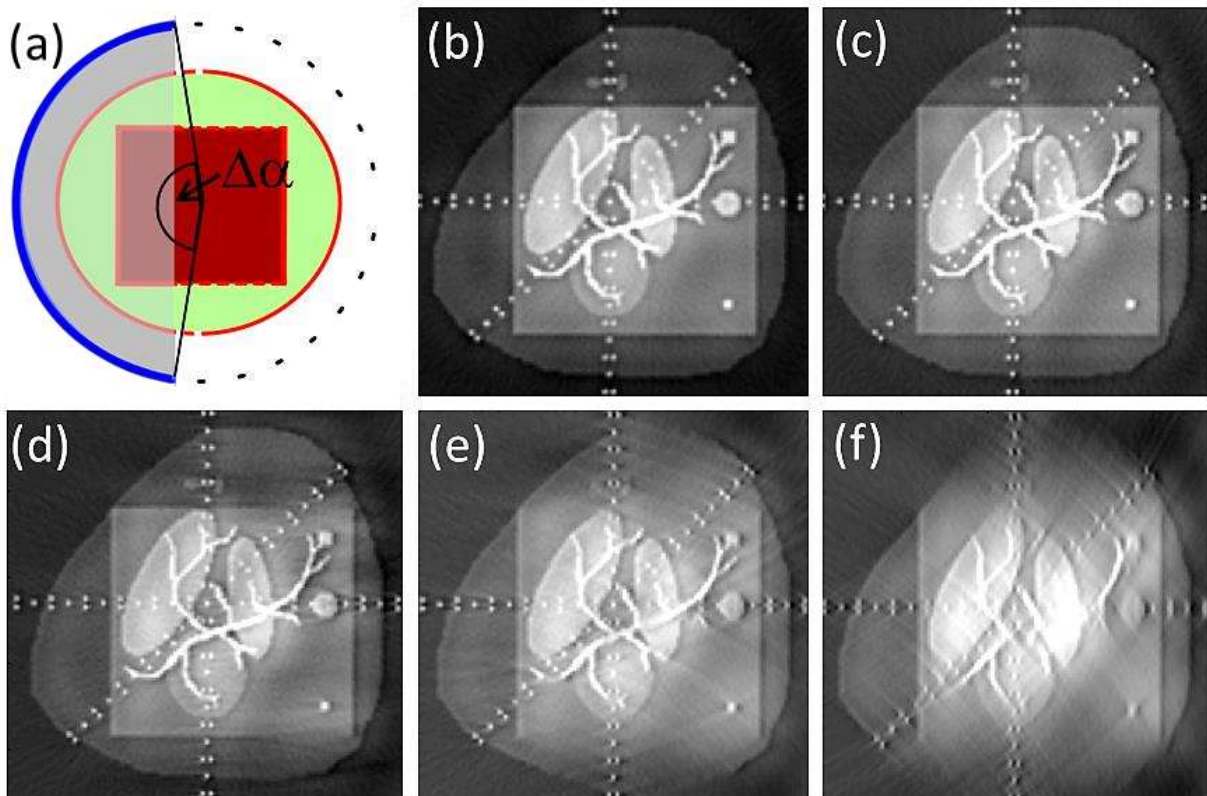
Figure 3.5 Demonstration of the limited-view problem for a simulated imaging scenario. (a) Reconstruct-able (red solid line) and "invisible" (red dashed line) boundaries of a round object with a square insertion partially lying in the "visibility region" (grey area) and the "invisibility domain" for a detector array (blue solid arc). Dashed boundaries suffer blurring since they do not fulfill the detection criterion, i.e. they do not have a normal passing at least through one detector position. (b) IMMI reconstruction of the numerical phantom using full-view ($\Delta\alpha = 360°$) data, and partial view data with (c) $\Delta\alpha = 240°$, (d) $\Delta\alpha = 180°$, (e) $\Delta\alpha = 140°$, and (f) $\Delta\alpha = 90°$, showing that boundaries not fulfilling the detection criterion suffer blurring.

3.5 MB OA reconstruction in LV scenarios

A small-animal imaging problem can be addressed as a 2D problem with light-sheet illumination, to selectively generate OA signals in a narrow volume, and a collection of OA responses with detectors cylindrically-focused onto the same small volume and arranged on an arc surrounding the animal. *Rosenthal et al.* developed a 2D interpolated matrix MB inversion algorithm for image reconstruction in such a 2D scenario, and they showed that, for full view (360°) detection geometries, this method has substantial advantages over the standard BP algorithms by not suppressing low frequency information and avoiding negative value artefacts [116]. Yet, in many imaging implementations, full-view detection cannot be achieved, due to mechanical and practical constraints such as limited access to the imaging plane or cost. Consequently, the lack of a complete (360°) tomographic dataset imposes inversion challenges and might compromise the accuracy of the reconstruction by rendering some parts of the object invisible. The IMMI approach was shown in a later study that it suffers from ill-conditioned forward matrices leading to error-prone reconstructions. In this section, it is shown that the reconstruction errors follow a distinct pattern. Moreover, two algorithms that were presented in [136] to minimize such errors in the IMMI framework are discussed.

3.5.1 LV artefacts

LV reconstructions pose a particular challenge in OA tomography. The boundary of an object may be invisible in the reconstruction if the detection view is not sufficiently comprehensive. As mentioned in the previous section, this happens when there is no normal line orthogonal to the boundaries intersecting the detection curve [134], because in such a situation the wavefront is not

detected. IMMI, which yields artifact-free reconstructions under ideal full view conditions [116],

suffers from an additional difficulty when employed in LV scenarios.

As the detection curve is reduced (blue line in Figure 3.6(a)), the inversion of the matrix relation

in (38) becomes increasingly ill-conditioned and therefore more prone to errors. This effect was

illustrated in Figure 3.6(b), where the condition number of the matrix is given for different arc

lengths. In the specific scenario of LV reconstruction, the errors are manifested in stripe artefacts,

as shown in Figure 3.6(c) for a 170° detection arc. The artefacts are independent of the method

used to solve (38), and are generated for both the LSQR algorithm as well as for the pseudo-inverse

method. The stripes appear in the invisibility zone of the reconstructed image and do not fulfill the

detection condition. The smaller the detection arc is, i.e. the more ill-conditioned the problem is,

the stronger the stripes are. In addition, the stripes are more accentuated in deeper parts of the

region not covered by ultrasound detectors. Thus, regularization is necessary.

3.5.2 Regularization approaches

The reconstruction artefacts due to LV geometry can be significantly reduced by regularizing the

inversion in IMMI. The regularization is performed by exploiting the specific stripe shape of the

artefacts. The stripes involve large variations in the direction perpendicular to their orientation;

therefore, it would be beneficial to introduce a constraint that limits variations in this direction, i.e.

$$min_{\boldsymbol{z}} \|\boldsymbol{D}\boldsymbol{z}\|_2 \tag{49}$$

where $D \in \mathfrak{R}^{(n-1) \times n}$ stands for a discrete approximation of the first derivative operator

perpendicular to the ripple orientation. Without the loss of generality, it is assumed that we have a

detection arc like the one shown in Figure 3.6(a). In this case, the stripe artefacts are horizontal.

This side constraint penalizes strong variations in the pixel intensities along vertical lines (perpendicular to the stripe artefacts).
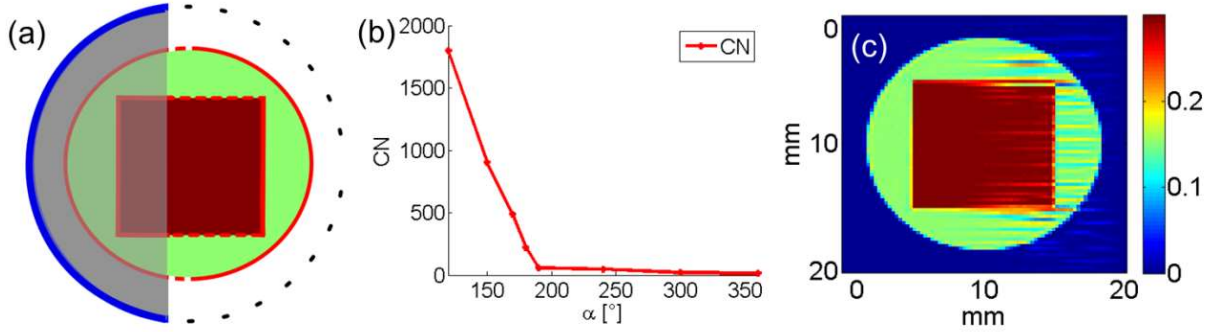
Figure 3.6: Another Example of LV artefacts. (a) Reconstruct-able (solid red line) and "invisible" (dashed red line) boundaries of a round object with a square insertion partially lying in the "visibility region" (gray-shaded area) and the "invisibility domain" for a detector ring (solid blue arc). Dashed boundaries suffer blurring since they do not fulfill the detection criterion, i.e. they do not have a normal passing at least through one detector position. (b) The condition number of the model-matrix M as a function of the detection arc. The higher the condition number, the more error-prone the inversion of M becomes. (c) IMMI reconstruction of the phantom. IMMI reconstructions show stripe artefacts in the invisibility domain. *(Source:* [136]*)*

Two methods for performing the regularization were investigated in [136]. A direct method, which regularizes the pseudo-inverse of M by using truncated generalized singular value decomposition (TGSVD), and a preconditioned iterative method (PLSQR) which searches the solution iteratively in a constrained subspace. The direct approach has the advantage of enabling a fast image reconstruction because, for a given imaging geometry, the regularized pseudo-inverse can be computed in advance and reused for consecutive reconstructions. The iterative method is appropriate for significantly larger matrices because in each iteration step only one column vector of the matrix is kept in the computer's working memory.

Truncated generalized singular value decomposition (TGSVD)

Truncated singular value decomposition (SVD) [137]–[140] is a common method for regularizing ill-conditioned inversion problems. The SVD of a matrix M is given by

$$M = U\Sigma V^T = \sum_{i=1}^{n} u_i \sigma_i v_i^T, \tag{50}$$

where U, V are orthonormal matrices ($V^T V = U^T U = I_n$) with the column vectors u_i and v_i ($i = 1 \ldots n$) and Σ is the diagonal matrix containing the singular values σ_i of M in descending order ($\sigma_1 > \sigma_2 \ldots > \sigma_n$). From (50), it follows that

$$\|M v_i\|_2 = \sigma_i. \tag{51}$$

Given that the matrix M connects the image vector z to the acoustic-signal vector p, the vectors v_i can be considered as *eigen-images*, whose corresponding normalized acoustic signals u_i can be considered as *eigen-signals*. The eigen-images are arranged such that the energy of their corresponding acoustic signal σ_i decreases with the index i. Using SVD, the solution to (38) can be written as a superposition of the eigen-images

$$z = \sum_{i=1}^{n} \frac{u_i^T p}{\sigma_i} v_i, \tag{52}$$

where $u_i^T p$ are the coefficients of the projection of p to the space spanned by $\{u_i\}$. The effect that a certain eigen-signal has on the reconstruction is inversely proportional to its singular value σ_i. In ill-conditioned problems, $\frac{\sigma_i}{\sigma_n} \gg 1$, therefore small variations or even noise in p values corresponding to high index eigen-signals can lead to perceived artefacts. Regularization can be achieved by truncation of (52), i.e.

$$z_k = \sum_{i=1}^{k} \frac{u_i^T p}{\sigma_i} v_i \quad with \quad k < n, \tag{53}$$

which can improve the stability of the inversion, since high index eigen-images, whose contribution to the solution in (52) is determined mostly by modeling errors and noise, are omitted in (53).

Ideally, the eigen-images that are cut off would contain only stripe artefacts. However, since the singular values usually decay gradually to zero, it is not possible to find an accurate cut-off value. For ensuring that stripe artefacts are not contained in the truncated solution, it is possible instead to employ the generalized singular value decomposition (GSVD) [139]. In GSVD, the orthonormality of the eigen-images is discarded in order to generalize the decomposition to include the quality measure $\|\boldsymbol{L}\boldsymbol{z}\|_2$, where $\boldsymbol{L}$ stands for a generalized discrete derivate operator of order p ($\boldsymbol{L} \in \Re^{(n-p)\times n}, m \geq n \geq p$). The GSVD of the matrix pair $\boldsymbol{M}$ and $\boldsymbol{L}$ can be written as:

$$\boldsymbol{M} = \boldsymbol{U} \begin{bmatrix} \boldsymbol{\Sigma} & \boldsymbol{0} \\ \boldsymbol{0} & \boldsymbol{I}_p \end{bmatrix} \boldsymbol{X}^{-1}, \qquad\qquad \boldsymbol{L} = \boldsymbol{V}(\boldsymbol{W},\boldsymbol{0})\boldsymbol{X}^{-1}, \qquad (54)$$

where $\boldsymbol{U} = [\boldsymbol{u}_1, \boldsymbol{u}_2, \ldots, \boldsymbol{u}_n]$, and $\boldsymbol{V} = [\boldsymbol{v}_1, \boldsymbol{v}_2, \ldots, \boldsymbol{v}_p] \in \Re^{(n-p)\times(n-p)}$ are orthonormal matrices and $\boldsymbol{X} = [\boldsymbol{x}_1, \boldsymbol{x}_2, \ldots, \boldsymbol{x}_p] \in \Re^{n\times n}$ is non-singular. Further $\boldsymbol{\Sigma} = diag(\sigma_1, \ldots, \sigma_{n-p})$ and $\boldsymbol{W} = diag(\mu_1, \ldots, \mu_{n-p})$, such that $0 \leq \sigma_1 \leq \cdots \leq \sigma_{n-p} \leq 1, 1 \geq \mu_1 \geq \cdots \geq \mu_{n-p} \geq 0$, and $\mu_i^2 + \sigma_i^2 = 1$. The generalized singular values are defined as $\gamma_i = \frac{\sigma_i}{\mu_i}$. For practical solutions, only the first derivative ($\boldsymbol{L} = \boldsymbol{D}, \ p = 1$) was considered in [136], leading to the following set of equations:

$$\boldsymbol{M}\boldsymbol{x}_i = \sigma_i\boldsymbol{u}_i \ (i = 1, \ldots, n-1), \quad \boldsymbol{M}\boldsymbol{x}_n = \boldsymbol{u}_n, \quad \|\boldsymbol{M}\boldsymbol{x}_i\|_2 = \sigma_i \ (i = 1, \ldots, n-1), \quad \|\boldsymbol{M}\boldsymbol{x}_n\|_2 = 1, \quad (55)$$

and

$$\boldsymbol{D}\boldsymbol{x}_i = \mu_i\boldsymbol{v}_i \ (i = 1, \ldots, n-1), \qquad \boldsymbol{D}\boldsymbol{x}_n = 0, \qquad \|\boldsymbol{D}\boldsymbol{x}_i\|_2 = \mu_i \ (i = 1, \ldots, n-1). \quad (56)$$

It has to be noted that in GSVD, the vectors $\boldsymbol{x}_i$ play the role of eigen-images and that the eigen images are ordered according to the energy of their corresponding normalized eigen-signals $\boldsymbol{u}_i$. In addition, the eigen-images are also organized according to the l_2–norm of their derivatives $\|\boldsymbol{D}\boldsymbol{x}_i\|_2$.

For GSVD with $p = 1$, the solution to (39) could be written as a superposition of the eigen-images in the following compact form:

$$z = \sum_{i=1}^{n-1} \frac{u_i^T p}{\sigma_i} x_i + (u_n^T p) x_n. \tag{57}$$

The regularized solution was achieved by using the "truncated" generalized singular value decomposition (TGSVD):

$$z_k = \sum_{i=n-k}^{n-1} \frac{u_i^T p}{\sigma_i} x_i + (u_n^T p) x_n. \tag{58}$$

Because the cut-off eigen-images correspond to large μ_i values, the transition between low and high index eigen-values will be characterized by strong pixel variation on the axis on which the derivative operator D acts. Since it is assumed that the OA image does not contain such strong pixel variations, the quality of the reconstruction will not be sensitive to the choice of the regularization parameter k. TGSVD can be understood as a variation of TSVD in which the role of the l_2-norm of the solution $\|z\|_2$ and eigen-images is replaced by the l_2-norm of the differentiated images $\|Dz\|_2$. In TSVD, the contribution of eigen-images is truncated, which would require high energy to marginally reduce the residual error, thus effectively, penalizing unnecessary high energy contributions. In contrast, in TGSVD it is the contribution of eigen-images in which a high energy for the differentiated images is required to marginally reduce the residual error which is truncated, thus penalizing unnecessary contributions with strong stripe-like variations [136].

Preconditioned LSQR (PLSQR)

The standard LSQR algorithm minimizes the residual error in (39) under the restriction that the solution lies in the Krylov subspace satisfying

$$K_k(\boldsymbol{M}^T\boldsymbol{M}, \boldsymbol{M}\boldsymbol{p}) \approx span\{\boldsymbol{v}_1, \dots, \boldsymbol{v}_k\}. \tag{59}$$

Hence, the solution after iteration k is similar to the solution of the TSVD method, i.e. early iterations are generally associated with high singular values of $\boldsymbol{M}$ and the late iterations with the low ones. In limited view scenarios, in which $\boldsymbol{M}$ is ill-conditioned, the algorithm approaches the correct solution in early iterations but then diverges to a solution, which significantly deviates from the original image. Stopping the iterations before the artefacts appear can be a way to regularize the inversion. However, similar to the TSVD method, this penalizes high energy values $\|\boldsymbol{z}_k\|_2$ and therefore the LSQR is not particularly adapted to deal with the stripe artefacts.

To improve the sensitivity of the regularization to the stripe artefacts, the preconditioned LSQR algorithm (PLSQR) was investigated [141], [142]. In contrast to the standard LSQR algorithm, in which stopping of iterations penalizes $\|\boldsymbol{z}_k\|_2$, PLSQR penalizes the more general functional $\|\boldsymbol{L}\boldsymbol{z}_k\|_2$ and therefore early iterations of the PLSQR algorithm are characterized by having low $\|\boldsymbol{L}\boldsymbol{z}_k\|_2$ values. By choosing $\boldsymbol{L} = \boldsymbol{D}$, the stripe artefacts appear in later iterations than for the standard LSQR algorithm and consequently, there is a better separation between image relevant information and artefacts, which leads to a better reconstruction accuracy.

More information about the performance evaluation of both regularization techniques on simulated & experimental data can be found in [136].

4. ACOUSTIC HETEROGENEITIES IN OA IMAGE RECONSTRUCTION

As demonstrated in the previous chapters, OA tomography of small animals is emerging as an adept method for optical imaging in tissues; the evident advantage being that of the high resolution achieved within several millimeters to centimeters of tissue with less scattering of light compared to pure optical methods [53], [54], [123]. Common implementations utilize spatially selective absorption of a short-pulsed light radiation, which in turn generates broadband ultrasonic waves due to the instantaneous thermoelastic expansion of the tissue. The ultrasonic waves emitted are measured around the object imaged and used to reconstruct the underlying optical energy absorption in the sample. Using imaging at several wavelengths, multi-spectral OA tomography (MSOT) has further shown the capacity to perform molecular imaging [143].

As shown in chapter 3, and for simplicity of the model, most OA reconstruction algorithms are derived assuming a homogeneous acoustic medium with constant speed of sound [125], [127], [144]–[147]. However, since several tissues have acoustic impedance variations, this assumption may affect the quality of the reconstructions. In general, the speed of sound and the density of the tissue are space-dependent, and different effects occur along the propagation path of the ultrasonic waves depending on the degree of acoustic heterogeneity. For small variations of the speed of sound, the direction of propagation of the ultrasonic waves is barely distorted while the differences in the speed of sound mainly affect the time of arrival of the signals [148], [149], i.e., the propagation of the waves can be modelled considering straight acoustic rays. However, when these variations are higher, the ultrasonic wavefronts curve or bend significantly as the wave propagates,

and so it is convenient to use a model that takes into account the change of direction of the acoustic rays [150]. On the other hand, other acoustic phenomena take place in the interface between two media with different acoustic impedance, such as scattering, reflection, or refraction [151], which can become significant for strong acoustic mismatch.

The variation of the speed of sound in soft tissues is rarely higher than 10% [108]. Under these conditions, several authors proposed reconstruction algorithms based on assuming straight propagation of the acoustic rays [152]–[154]. The bending of the acoustic waves has also been considered [155]. Another approach consists of taking a first-order approximation of the wave equation in the frequency domain for heterogeneous media [126], [156]. However, once the acoustic mismatches become stronger, additional artefacts are produced, e.g., in case of OA wave propagation through an intact skull [157].

In the following sections, we will mainly discuss a method developed previously in our research group that utilizes statistical weighting for the purpose of mitigating artefacts due to the presence of acoustic heterogeneities [158]–[160]. We recently further expanded the capability of this method to perform better in the case of PV scanning geometries [161].

4.1 Statistically-weighted BP (wBP) OA reconstruction

4.1.1 Recap of the basic principle of the BP algorithm

The OA effect refers to the induction of pressure waves due to the thermoelastic expansion caused by the absorption of light energy in a medium. The theoretical basis of the OA generation of

ultrasonic waves inside a tissue is well-known and can be found in the literature and was discussed in chapter 2. To recap; when a pulsed laser is used as the illumination source, the laser pulse duration is usually short enough to neglect thermal diffusion, and the temporal dependence of the light intensity at any point can be effectively expressed as a Dirac delta $\delta(t)$. Under such conditions, the pressure field corresponding to the generated ultrasonic wave in a homogeneous acoustic medium satisfies

$$\frac{\partial^2 p(\boldsymbol{r}, t)}{\partial t^2} - c^2 \nabla^2 p(\boldsymbol{r}, t) = \Gamma H(\boldsymbol{r}) \frac{\partial \delta(t)}{\partial t} \tag{60}$$

where c is the speed of sound in the medium, Γ is the Grüneisen parameter, and $H(r)$ is the optical absorption field, i.e. the amount of energy absorbed in the target per volume unit. The Poisson's solution of (60) can be used to calculate the pressure field at any given location and time instant as

$$p(\boldsymbol{r}, t) = \frac{\Gamma}{4\pi c} \frac{\partial}{\partial t} \int_{S'} \frac{H(\boldsymbol{r}')}{|\boldsymbol{r} - \boldsymbol{r}'|} dS' \tag{61}$$

where S' is a time-dependent spherical surface for which $|\boldsymbol{r} - \boldsymbol{r}'| = ct$. Equation (61) shows that the pressure $p(\boldsymbol{r}, t)$ in a homogeneous acoustic medium is solely due to the optical absorption at locations $\boldsymbol{r}'$ so that the generated waves require time t to reach location $\boldsymbol{r}$.

In OA imaging, the goal is to reconstruct the field $H(\boldsymbol{r}')$ given the value of the pressure recorded at a set of points. In a universal back-projection algorithm for homogeneous acoustic media [125], the optical absorption field is given by

$$H(\boldsymbol{r}') = \frac{1}{\Gamma} \int_{\Omega} \frac{d\Omega}{\Omega} \left[2p(\boldsymbol{r}, t) - 2t \frac{\partial p(\boldsymbol{r}, t)}{\partial(t)} \right] \Bigg|_{t=|\boldsymbol{r}-\boldsymbol{r}'|/c}. \tag{62}$$

In principle, (62) is deduced for a surface S enclosing r', i.e. the solid angle $\Omega = 4\pi$. $d\Omega$ is the solid angle for an element dS and acts as a weighting factor in the reconstruction. The reconstruction procedure consists in projecting the value of the quantity $2p(r,t) - 2t\frac{\partial p(r,t)}{\partial(t)}$ for a given instant t and for a given point r back onto the spherical surface where a wave should be generated to reach the point r at instant t according to (61).

For simplicity, the 2-D case is considered, for which a 2-D cross section of the sample is imaged. To achieve this as shown before, a cylindrically focused ultrasonic transducer can for instance be used to measure the outgoing pressure waves around a circumference of the object. If the slice to be imaged lies in the focal zone of the transducer, the detected pressure corresponds approximately to the waves generated due to the optical absorption in that slice. In this case, an approximate solution for the circular-scan geometry can be obtained by considering the *back-projection* algorithm in a 2-D geometry [128]. Furthermore, if the scanning radius is much larger than the size of the object, the angle covered by each transducer is approximately constant. Under these conditions, a 2-D discretization of (62), in which, for simplicity, all the constants are dropped for the case of qualitative imaging, is given by

$$H(r'_j) = \sum_i \left[p(r_i, t_{ij}) - t_{ij} \frac{\partial p(r_i, t_{ij})}{\partial t} \right] \tag{63}$$

where r_i is the position of ith transducer, r'_j is the position of the jth point of the reconstruction region of interest, and $t_{ij} = |r_i - r'_j|/c$.

4.1.2 Statistical weighting of the BP algorithm to account for acoustic heterogeneities

In back-projection reconstruction, all acoustic transducers contribute equally to the reconstruction of the optical absorption at any given point r'_j (as was shown in (63)). However, when there are acoustic reflectors or scatterers inside the target, the pressure detected at each transducer may not correspond to the wave generated at r'_j, but rather to a reflected or scattered wave generated at a different point. Consequently, some artefacts may appear in the reconstructions obtained with (63) due to the signals that underwent scattering or reflection during their propagation. Therefore, it must be taken into consideration that not all of the signals recorded at different transducers are equally relevant for reconstructing the optical absorption at r'_j. That is; the likelihood of detecting an undistorted signal generated at r'_j depends on the position of the transducer at r_i.

To demonstrate the statistical weighting that was introduced in [158], a 2D imaging domain was assumed in which a closed curve ∂A encloses an area A (the grey area in Figure 4.1) containing all the optical absorbers and all acoustic reflectors and acoustic scatterers. Let $f_E(r')$ be the probability density function corresponding to the location at which a differential of energy is absorbed. That is; if *a priori* knowledge does not exist on the actual distribution of optical absorbers within the imaged target, $f_E(r')$ could be assumed to correspond to a uniform distribution such that

$$\int_B f_E(r')dr' = \frac{B}{A} \tag{64}$$

where B is any subsurface inside A. Equation (64) shows that the probability that a differential of energy is absorbed within B, or, equivalently, the expected fraction of the total energy absorbed in A that is absorbed in the subsurface B.
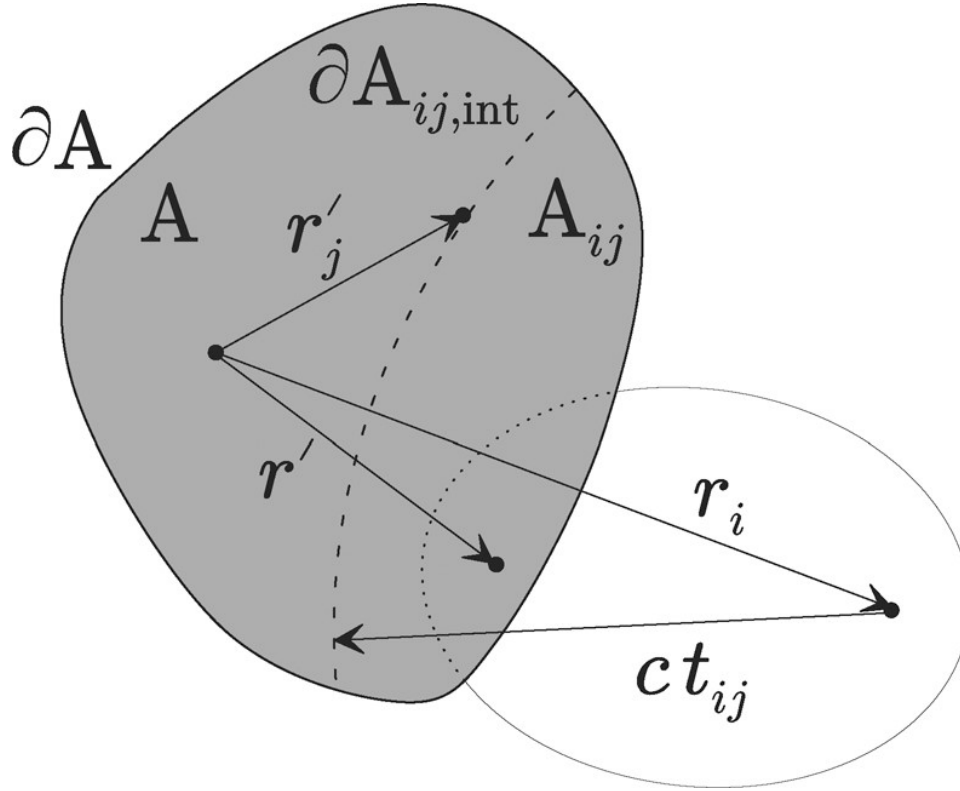
Figure 4.1. Principle underlying the statistical weighting to mitigate reconstruction artefacts due to the presence of acoustic heterogeneities. The closed curve ∂A encloses an area A containing all the optical absorbers and all the acoustic reflectors and scatterers. $\boldsymbol{r}_i$ is the position of the ith transducer and $\boldsymbol{r}'_j$ is the position of the jth point of the reconstruction region of interest. The wave generated at $\boldsymbol{r}'_j$ reaches the point $\boldsymbol{r}_i$ at an instant $t_{ij} = |\boldsymbol{r}_i - \boldsymbol{r}'_j|/c$. The dashed line ($\partial A_{ij,\mathrm{in}}$) contains the points in which a wave detected at $\boldsymbol{r}_i$ at instant t_{ij} was generated in case it propagates directly to the transducer. This wave could have been generated at any point inside the area A_{ij} in case it was reflected or scattered. As an example, a wave can be generated at any given point $\boldsymbol{r}'$, reflected at any point on the dotted line of the ellipse, and reach the transducer located at $\boldsymbol{r}_i$ also at the same instant t_{ij}. *(Source:* [158]*)*

In light of this probabilistic assumption, one can discuss the contribution of the transducer located at $\boldsymbol{r}_i$ to the reconstruction of the optical absorption in a point located at $\boldsymbol{r}'_j$. The back-projection algorithm is deduced assuming a homogeneous acoustic medium, so that according to (61) the pressure measured with the transducer at a given instant $t_{ij} = |\boldsymbol{r}_i - \boldsymbol{r}'_j|/c$ is originated by the

optical absorptions along a branch of the circumference $\partial A_{ij,in}$ with radius equal to ct_{ij} (dashed line in Figure 4.1), centered at the transducer's position. However, when considering acoustically heterogeneous media, one could assume a probability distribution that the OA wave has been generated at any point inside the area A_{ij} (for example, $\boldsymbol{r}'$ in Figure 4.1), and then redirected to the transducer via reflection and/or scattering events. Consequently, it might also be detected at the same instant t_{ij} as a wave that was supposedly generated in $\partial A_{ij,\text{in}}$ and propagated undisturbed directly to the transducer. The probability $P_{\mathrm{r}}^{i}(t_{ij})$ can then be defined such that a "reflected" or scattered wave with unit amplitude is detected by the ith transducer at time t_{ij}. According to Bayes' theorem, this probability can be expressed as

$$P_{\mathrm{r}}^{i}(t_{ij}) = \int_{A_{ij}} P_{\mathrm{r}}^{i}(t_{ij}|\boldsymbol{r}')f_{E}(\boldsymbol{r}')d\boldsymbol{r}' \tag{65}$$

where $P_{\mathrm{r}}^{i}(t_{ij}|\boldsymbol{r}')$ is the conditional probability that a reflected or scattered wave with unit amplitude is detected at t_{ij} given that all the energy absorbed by the sample is entirely absorbed at location $\boldsymbol{r}'$. As $f_{E}(\boldsymbol{r}')$ was assumed to correspond to a uniform distribution, (65) can be further expressed as

$$P_{\mathrm{r}}^{i}(t_{ij}) = \frac{A_{ij}}{A} \int_{A_{ij}} P_{\mathrm{r}}^{i}(t_{ij}|\boldsymbol{r}')d\boldsymbol{r}' = \frac{A_{ij}}{A} \bar{P}_{\mathrm{r}}^{i}(t_{ij}) \tag{66}$$

where $\bar{P}_{\mathrm{r}}^{i}(t_{ij})$ is proportional to the mean value of $P_{\mathrm{r}}^{i}(t_{ij}|\boldsymbol{r}')$ inside A_{ij}. Generally, the estimation of $P_{\mathrm{r}}^{i}(t_{ij}|\boldsymbol{r}')$ is complex. The simplest approximation assumes that $\bar{P}_{\mathrm{r}}^{i}(t_{ij})$ is constant regardless of t_{ij} and $\boldsymbol{r}_{i}$. That is;

$$\bar{P}_{\mathrm{r}}^{i}(t_{ij}) = k_{1}. \tag{67}$$

Another approximation for $P_r^i(t_{ij}|r')$ consists in considering that the wave generated at r' has undergone a single reflection or scattering event. Since the amplitudes of the reflected or scattered waves are generally significantly lower than the amplitude of the original one, this approximation is valid for many practical cases. In such case, the reflection or scattering must take place at a branch of an ellipse whose foci are located in r' and r_i and whose major axis is equal to ct_{ij} (dotted line in Figure 4.1). $\bar{P}_r^i(t_{ij})$ can be expressed according to this approximation as

$$\bar{P}_r^i(t_{ij}) = k_2 \frac{A_{ij}}{A} . \tag{68}$$

We refer the reader to the original publication in which this formula was derived [158]. Both (67) and (68) can be used as first order approximations for $\bar{P}_r^i(t_{ij})$. The simplification used in (67) can also be used in some cases for reflectors or scatterers located outside the area A, so A can be chosen preferably as the area containing the points where optical absorbers exist.

Then, $P_{r,\text{dist}}^i(t_{ij})$ was defined as the probability that the wave measured at the ith transducer at instant t_{ij} is "distorted" by a "reflected" or scattered wave [158]. Practically, the measured wave is distorted when the amplitude of the reflected or scattered wave is above the noise level, so $P_{r,\text{dist}}^i(t_{ij})$ is proportional to $P_r^i(t_{ij})$. Considering that a probability cannot be higher than 1, and in the case that $\bar{P}_r^i(t_{ij})$ is given by (67), then $P_{r,\text{dist}}^i(t_{ij})$ can be expressed as

$$P_{r,\text{dist}}^i(t_{ij}) = \min\left(1, \omega\frac{A_{ij}}{A}\right) \tag{69}$$

where ω is a constant weighting parameter that depends on the internal features of the target and on the sensitivity of the acoustic detectors. In the case that the other approximation of $\bar{P}_r^i(t_{ij})$ as in (68) is employed, $P_{r,\text{dis}}^i(t_{ij})$ can also be written as a function of ω as

$$P_{\mathrm{r,dist}}^{i}(t_{ij}) = \min\left[1, \omega\left(\frac{A_{ij}}{A}\right)^2\right]. \qquad (70)$$

Then, the probability $P_{\mathrm{d}}^{i}(t_{ij})$ that the wave detected by the ith transducer at time instant t_{ij} corresponds to a "direct" propagation (i.e. not distorted particularly by a reflected signal), could be simply given by

$$P_{\mathrm{d}}^{i}(t_{ij}) = 1 - P_{\mathrm{r,dist}}^{i}(t_{ij}). \qquad (71)$$

Therefore, this weighted variant of the back-projection reconstruction algorithm (Henceforward referred to as wBP) that was proposed in [158] was achieved mainly by weighting each detector's contribution to the reconstruction of optical absorption at $\boldsymbol{r}_j'$ with the value of $P_{\mathrm{d}}^{i}(t_{ij})$. To reflect such weighting, (63) was modified as follows:

$$H(\boldsymbol{r}_j') = \sum_i P_{\mathrm{d}}^{i}(t_{ij})\left[p(\boldsymbol{r}_i, t_{ij}) - t_{ij}\frac{\partial p(\boldsymbol{r}_i, t_{ij})}{\partial t}\right]. \qquad (72)$$

The value of ω can be determined heuristically. For example, for a sample in which reflections or scattering are very likely to occur, it has a high value, while in a sample with very few possible reflectors or scatterers it can approach null [158]. If the sample is modelled as a homogeneous medium, the probability that the pressure detected at any transducer is distorted due to reflections or scattering is null (i.e. $\omega = 0$), and consequently the wBP algorithm corresponds back to the conventional BP algorithm.

4.1.3 Experimental validation of the wBP approach

The authors of the wBP algorithm validated its reconstruction results experimentally on tissue-mimicking phantoms and a Zebrafish *post mortem* [158]. The illuminating source of the OA

system utilized in the experimental validation was based on an optical parametric oscillator laser whose wavelength was set to 605 nm for the experiments with tissue-mimicking phantoms, and to 587 nm for experiments with the Zebrafish. The output beam size was changed using variable optics to adapt it to the size of the phantoms or fish, then split into two parts and directed onto the object from two opposite sides to achieve a ring-like uniform illumination around the target. The ultrasonic detection part of that OA system consisted of high-sensitivity ultrasonic immersion piezoelectric transducers with a center frequency of 3.5 MHz for phantom imaging, and 15 MHz for the Zebrafish imaging. For phantom validation, signal acquisition for 180 tomographic projections was obtained by rotating the samples via a high-speed rotation stage with angular steps of 2. For Zebrafish imaging, the authors employed a continuous acquisition method (no averaging) to acquire 800 projections over a full 360° circular rotation. For more information on the details of the experimental setup, the reader is referred to a previous publication [162].

The authors used several phantoms for the experimental validation of the wBP reconstruction algorithm [158]. To illustrate the nature of artefacts produced due to acoustic reflections, they first prepared an agar phantom with no background absorption or scattering (pure agar). That phantom included a cylindrical absorbing inclusion and a hollow cylindrical cavity (straw filled with air). The optical absorption coefficient of the absorbing inclusion was $\mu_a = 1.2 \text{cm}^{-1}$. Additional phantoms were also prepared in which background optical absorption and scattering were added. Such background had an approximate optical absorption coefficient of $\mu_a = 0.2 \text{cm}^{-1}$ and a reduced scattering coefficient of $\mu'_s = 10 \text{cm}^{-1}$ in order to mimic the optical characteristics of biological tissues [100]. Similarly, inclusions with higher optical absorption and hollow cylindrical cavities were included in the tissue-mimicking phantoms. Some of these higher absorbing

inclusions had an optical absorption coefficient of $\mu_a = 1\text{cm}^{-1}$, while other inclusions had $\mu_a = 1.6\text{cm}^{-1}$. The authors also imaged an adult wild-type Zebrafish *post mortem*. The fish contains several mismatched tissues, like small bones and air cavities, which helped further demonstrate the capability of the wBP method to reduce image artefacts produced by acoustic mismatches. The fish was embedded in pure agar in order to make its handling easier while undergoing tomographic imaging.

Results of the first phantom experiment (pure agar phantom with no background absorption nor scattering) are shown in Figure 4.2. In (b) and (c), a dark halo around the reflecting straw is clearly visible, demonstrating the typical OA reconstruction artefacts produced by strong acoustic mismatches in the target. The cause of such halo was indeed due to waves reflected at the surface of the reflecting straw, which were erroneously back-projected assuming they propagate non-disturbed directly toward the ultrasound detector, forming such typical pattern. (c) is a zoomed version of (b), which was the reconstruction obtained with the conventional BP formula (or with
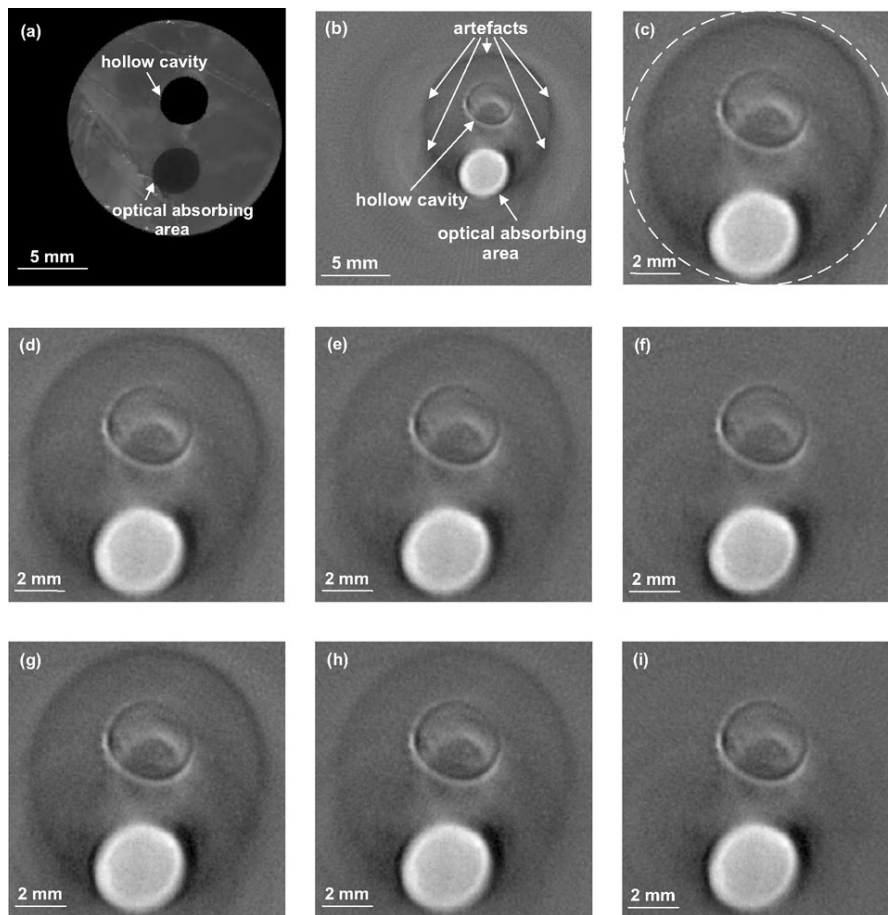

Figure 4.2. Results of wBP reconstruction of the phantom with pure agar background, an absorbing inclusion, and a hollow cylindrical cavity.   (a) Circular cross section of the cylindrical phantom (photograph). (b) and (c) are reconstructions obtained with conventional BP. The halo around the reflector demonstrates the typical reconstruction artefacts due to reflection or scattering of the ultrasonic waves. For this phantom, the area A is delineated by the dotted white circle in (c). (d), (e), and (f) are, respectively, the OA reconstructions generated with wBP in the case that $P^i_{r,\text{dist}}(t_{ij})$ is given by (69) for $\omega = 0.33$, $\omega = 0.66$, and $\omega = 1$. On the other hand, (g), (h), and (i), respectively, are the same reconstructions as in (d), (e), and (f) but when (70) was used as the approximation for $P^i_{r,\text{dist}}(t_{ij})$. *(Source: [158])*

the wBP for $\omega = 0$). For the wBP reconstruction, the area A was taken as the circle delineated by the dotted white circumference in (c). (d), (e), and (f) are, respectively, the OA reconstructions generated with wBP in the case that $P^i_{r,\mathrm{dis}}\left(t_{ij}\right)$ is given by (69) for $\omega = 0.33$, $\omega = 0.66$, and $\omega = 1$. On the other hand, (g), (h), and (i), respectively, are the same reconstructions as in (d), (e), and (f) but when (70) was used as the approximation for $P^i_{r,\mathrm{dist}}(t_{ij})$. In both cases, the reduction of the erroneously reconstructed halo was proportional to the value of ω, without introducing much distortion to the absorbing inclusion. Since the reconstructions obtained using (69) or (70) as the formula for $P^i_{r,\mathrm{dis}}\left(t_{ij}\right)$ were quite similar, the authors decided to proceed with (69) as the one used for further evaluation of their proposed method [158].

The authors proceeded to experiment with tissue-mimicking phantoms (i.e. containing background optical absorption and scattering). For these phantoms, the authors expected more reconstruction artefacts, since the light absorption took place throughout the phantom, and consequently more reflections were generated [158]. They employed four different phantoms with different optical absorbing areas and hollow cavities and with different concentrations of India ink for the absorbers. Here, the results of the OA reconstruction of two of these four tissue-mimicking phantoms obtained with conventional BP and wBP are shown in Figure 4.3. For all of these cases, the area A required for the weighting method corresponds to the circle inscribed in the square-shaped ROI, and $\omega = 1$. It can be clearly observed that the results obtained with wBP show less artefacts compared to the ones obtained with conventional BP, while maintaining minimum distortion in other image regions.
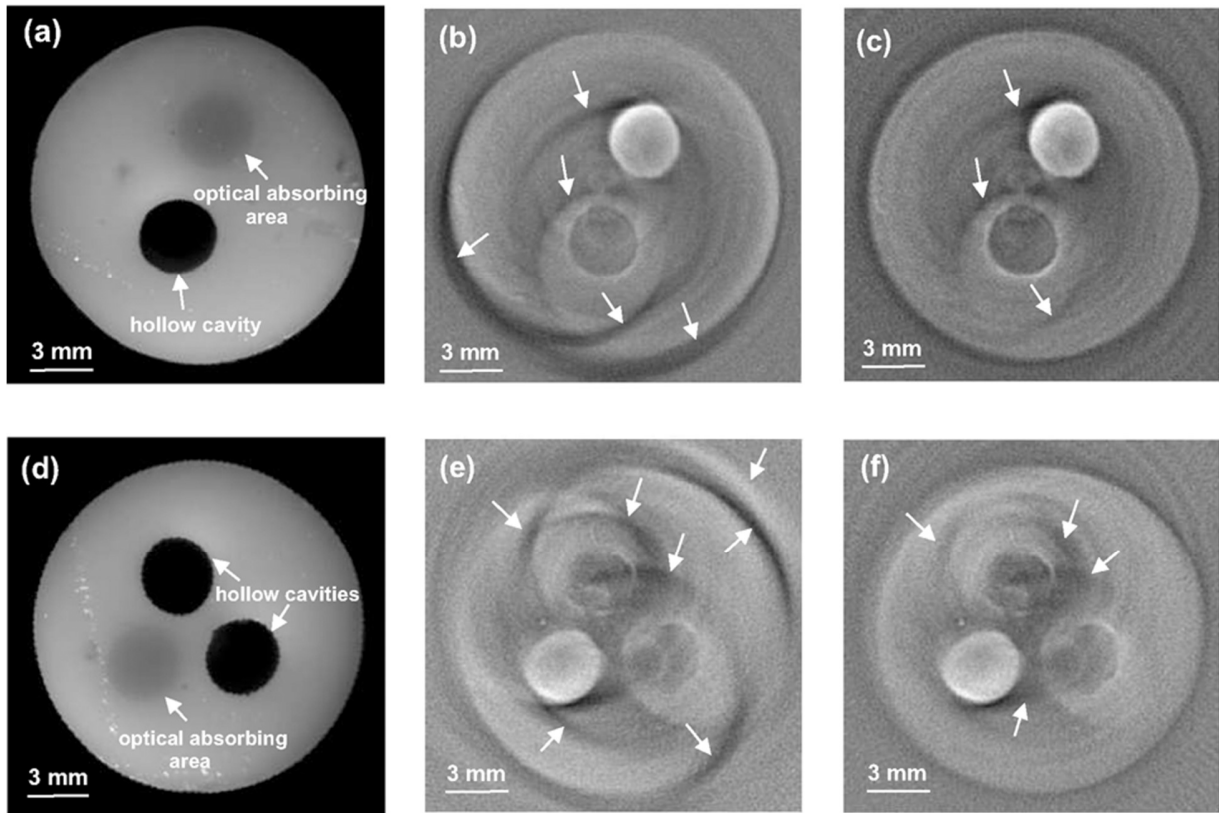
Figure 4.3. Results of two tissue-mimicking phantoms (i.e. absorbing and scattering background) with absorbing inclusions and hollow cylindrical cavities. The first column of the image ((a) and (d)) shows the circular cross sections of the phantoms (photographs). The second column ((b) and (e)) shows reconstructions obtained with conventional BP. The third column ((c) and (f)) shows reconstructions obtained with wBP for $\omega = 1$. The area A was taken as the circle inscribed in the region of interest. Arrows in the second and third columns indicate the artefacts due to reflections or scattering of the acoustic waves, which were significantly reduced with the wBP method (third column). *(Source:* [158]*)*

Further validation of the wBP method was carried out by the authors on Zebrafish *post mortem* [158]. Here, we present the results of their validation in Figure 4.4. The cross-section of the Zebrafish that was the target for their validation corresponded anatomically to the swim bladder, liver and intestines level. Panels (a) and (b) show the OA reconstruction with classical BP and wBP ($\omega = 1$), respectively. By comparing (b) to (a), it was evident that the wBP approach reduced image artefacts both outside the fish (indicated by arrows 1 and 2) and also inside the fish (Arrow 3). Furthermore, the authors noticed an increase in the sharpness of the image boundaries, which
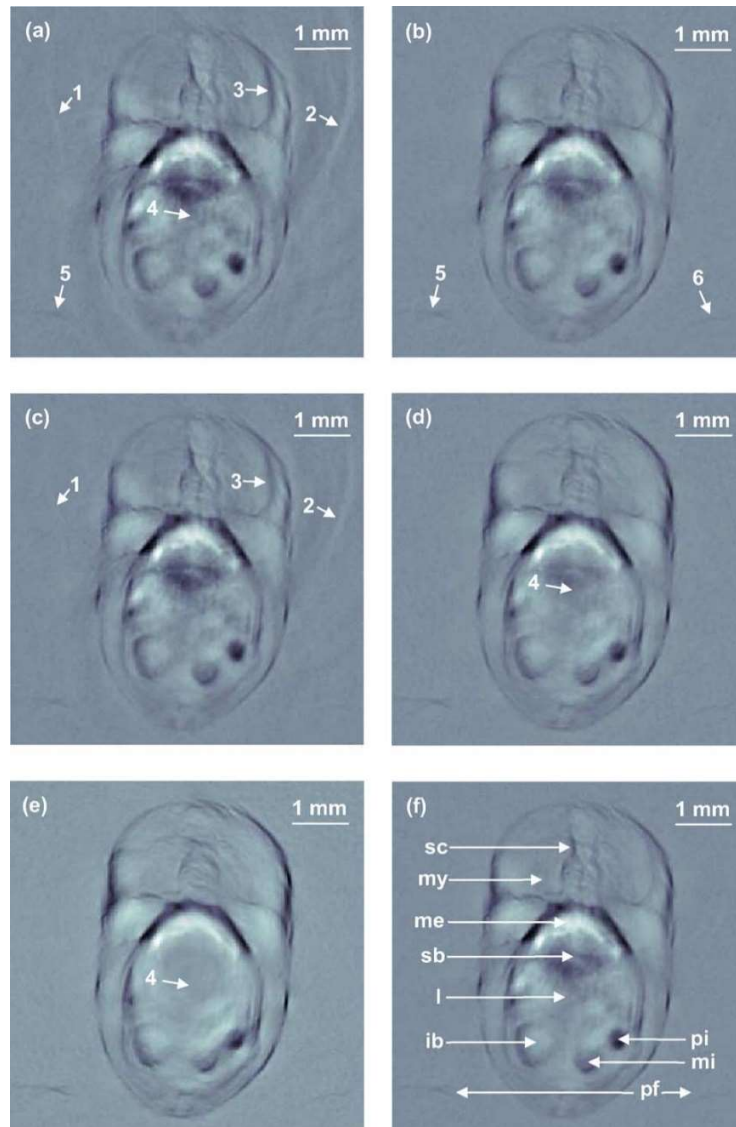
Figure 4.4. Results of OA reconstructions of Zebrafish obtained with the wBP method for $\omega = 0$ (a) (corresponds to conventional BP), $\omega = 1$ (b), $\omega = 0.5$ (c), $\omega = 1.5$ (d), and $\omega = 2$ (e). Arrows 1, 2, and 3 indicate reflection artefacts. Arrow 4 indicates a region around the liver which is smeared for high values of ω. Arrows 5 and 6 correspond to the pectoral fins. Some relevant anatomical structures were labelled in (f): *spinal cord (sc), myotome (my), mesonephros (me), swim bladder (sb), liver (l), intestinal bulb (ib), posterior intestine (pi), midintestine (mi), and pectoral fins (pf). (Source:* [158]*)*

have apparently been blurred by the reflection artefacts. Panels (c), (d) and (e) display the reconstructions generated with the wBP method for ω values of 0.5, 1.5, and 2, respectively. In panel (c), it can be noticed that the artefacts both from inside and outside the fish volume were still present, although they were slightly mitigated in comparison with (a) (obtained with conventional BP). However, in (d) and (e), the inner structures around the liver were smeared (as indicated by

arrow 4). This drawback was significantly apparent for $\omega = 2$. Hence, the authors' conclusion was that the result obtained with $\omega = 1$ had the best quality among the five images obtained with different values of ω [158].

4.2 Introducing acoustic apriori to the wBP approach

4.2.1 Theoretical basis for expanding wBP reconstruction when acoustic apriori are available

In the wBP approach, the authors assumed that no knowledge about the location and distribution of optical absorbers or acoustic heterogeneities is present [158]. In a following publication, they expanded on the wBP approach by assuming that knowledge about the location of acoustic heterogeneities is provided (Henceforward, this modified approach is referred to here as "wBP+apriori") [159]. Mainly, they proposed to utilize the *apriori* info about the acoustic reflectors or scatterers to specifically derive a more precise expression for $P_\mathrm{r}^i(t_{ij}|\boldsymbol{r}')$ (the conditional probability that a reflected or scattered wave with unit amplitude is detected at t_{ij} given that all the energy absorbed by the sample is entirely absorbed at location $\boldsymbol{r}'$).

As shown in Figure 4.5 (which is an expanded version of Figure 4.1), the authors of [159] considered that an area B containing all the reflectors and scatterers could be determined inside
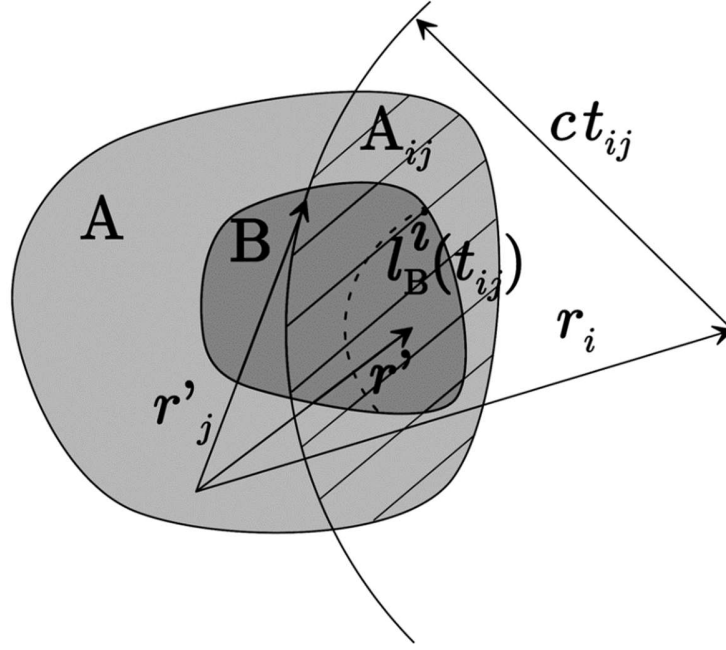
Figure 4.5. Principle underlying the modified wBP+apriori reconstruction approach. This illustration is an expanded version of the illustration in Figure 4.1 (taken from [158]). The area B was taken to contain all the acoustic reflectors and scatterers. $l_B^i(t_{ij})$ is a line inside the area B corresponding to the set of points at which a wave generated at r' must be reflected or scattered to reach the ith transducer at instant t_{ij}. *(Source: [159])*

the area A. The authors also adopted a further practical simplification as in [158], which was the

assumption that an OA wave detected by any given transducer had been reflected or scattered only

once, thus all secondary reflection or scattering events could be safely neglected [163]. Under such

assumptions, $P_r^i(t_{ij}|r')$ could be expressed as

$$P_\mathrm{r}^i(t_{ij}|\boldsymbol{r}') = k \int_B \delta[t_\mathrm{r}^i(\boldsymbol{r}',\boldsymbol{r}'') - t_{ij}] d\boldsymbol{r}'', \qquad \forall\, t_\mathrm{r}^i(\boldsymbol{r}',\boldsymbol{r}'') = \frac{|\boldsymbol{r}' - \boldsymbol{r}''|}{c} + \frac{|\boldsymbol{r}'' - \boldsymbol{r}_i|}{c} \quad (73)$$

where $\delta[\ \ ]$ is the one-dimensional Dirac delta function, $t_\mathrm{r}^i(\boldsymbol{r}',\boldsymbol{r}'')$ is the instant at which a wave

generated at $\boldsymbol{r}'$ (in A) and reflected or scattered at $\boldsymbol{r}''$ (in B) is detected by the ith transducer, and

k is a constant which depends on the particular characteristics of the reflectors or scatterers in the

target undergoing imaging. Equation (73) could also be rewritten as

$$P_\mathrm{r}^i(t_{ij}|\boldsymbol{r}') = k \int_{l_B^i(t_{ij})} dl \qquad\qquad (74)$$

where $l_B^i(t_{ij})$ is a line inside the area B corresponding to the set of points at which a wave generated at $\boldsymbol{r}'$ must be reflected or scattered to reach the ith transducer at instant t_{ij}.

For the modified wBP+apriori approach, the authors assumed no *a priori* knowledge about the location and distribution of optical absorbers was available (similar to their assumption for wBP in [158]). Thus, $f_E(\boldsymbol{r}')$ (the probability density function corresponding to the location at which a differential of energy is absorbed) is also in [159] equivalent to a uniform distribution all over the area A. Thus, substituting (73) in (65) gives

$$P_{\mathrm{r}}^i(t_{ij}) = \frac{k}{A} \int_A \left\{ \int_B \delta[t_{\mathrm{r}}^i(\boldsymbol{r}', \boldsymbol{r}'') - t_{ij}] d\boldsymbol{r}'' \right\} d\boldsymbol{r}' \ . \tag{75}$$

Equation (75) suggested that the two points $\boldsymbol{r}'$ and $\boldsymbol{r}''$ in A and B, respectively, contribute to $P_{\mathrm{r}}^i(t_{ij})$ for $t_{ij} = t_{\mathrm{r}}^i(\boldsymbol{r}', \boldsymbol{r}'')$. Therefore, the authors proposed to estimate the shape of $P_{\mathrm{r}}^i(t_{ij})$ by means of the *Monte Carlo* simulation [159]. This was achieved by generating random n pairs of points $(\boldsymbol{r}', \boldsymbol{r}'')$ in A and B, respectively, and then calculating the corresponding values of $t_{\mathrm{r}}^i(\boldsymbol{r}', \boldsymbol{r}'')$ using the formula in (73). For large values of n, the authors expected that the histogram of $t_{\mathrm{r}}^i(\boldsymbol{r}', \boldsymbol{r}'')$ could faithfully represent the shape of $P_{\mathrm{r}}^i(t_{ij})$. A function $P_{\mathrm{r,hist}}^i(t_{ij})$ was then defined in the centers of the intervals of the histogram as the number of elements N in such intervals. For the rest of points, the value of $P_{\mathrm{r,his}}^i(t_{ij})$ was obtained by linear interpolation. Since $P_{\mathrm{r,dist}}^i(t_{ij})$ is proportional to $P_{\mathrm{r}}^i(t_{ij})$, and probability values should not exceed 1, $P_{\mathrm{r,dis}}^i(t_{ij})$ could be estimated as

$$P_{\mathrm{r,dist}}^i(t_{ij}) = \min\left(1, \omega \frac{P_{\mathrm{r,hist}}^i(t_{ij})}{\max\limits_{i,j}\left[P_{\mathrm{r,hist}}^i(t_{ij})\right]}\right) \qquad (76)$$

where ω is a heuristic weighting parameter that depends on the characteristics of the target under investigation and sensitivity of the detectors (similar to (69) for the wBP reconstruction without acoustic *a priori*). Equation (76) is then used for calculating $P_{\mathrm{d}}^i(t_{ij})$ as in (71) and subsequently for weighting the conventional BP formula as in (72).

4.2.2 Experimental validation of the wBP+apriori approach

The performance of the wBP+apriori method was validated on tissue-mimicking phantoms, in which strong acoustic reflectors (air-filled straws) were introduced. The approximate values of the optical absorption and reduced scattering coefficients for the background were, respectively, $\mu_a = 0.2\ cm^{-1}$ and $\mu_s' = 10\ cm^{-1}$ (similar to the optical properties of biological tissue) [100]. Additionally, higher absorbing areas with $\mu_a = 1.2\ cm^{-1}$ were embedded in the phantoms. The illumination source for the OA scanning apparatus used for this validation consisted mainly of a nanosecond-pulsed laser (605 nm). The output beam was then shaped by variable optics to obtain uniform illumination over the surface of the object under investigation. The generated ultrasonic signals were then detected with a cylindrically-focused piezoelectric transducer with a center frequency of 3.5 MHz. In order to acquire 180 projections, the agar phantom was rotated over 360° with 2° steps with a linear rotation stage. For further technical details about the OA scanning system used for this validation, the reader was referred to a previous publication [162].

For one of the validation phantoms used in [159], a cross-section indicating the position of the higher absorbing inclusion and the air-filled straw is shown in Figure 4.6. The authors assumed that areas A (enclosing the whole target and including all optical absorbers and acoustic heterogeneities) and B (specifically enclosing the strong acoustic reflector) could be uniquely determined (both marked with solid and dashed circles in panel (a), respectively). Subsequently, the shape of $P_r^i(t_{ij})$ was estimated by the previously mentioned Monte Carlo method with $n = 500$ for each position of the transducer. In Figure 4.7 (a) and (b), two examples (i.e. for two different detectors) of the generated histograms for $t_r^i(\boldsymbol{r}', \boldsymbol{r}'')$ are displayed. They were calculated considering 20 intervals for $t_r^i(\boldsymbol{r}', \boldsymbol{r}'') \in [t_1, t_2]$, where $t_1 = |R - R_A|/c$ is the instant for which the first direct wave is measured, $t_2 = |R + 3R_A|/c$ is the instant for which the last possible reflected or scattered wave is measured, R is the distance between the detector and the center of rotation, and R_A is the radius of the area A. For comparison purposes, the authors also generated the respective histograms for $n = 50{,}000$ and 200 intervals for the same two detectors (displayed
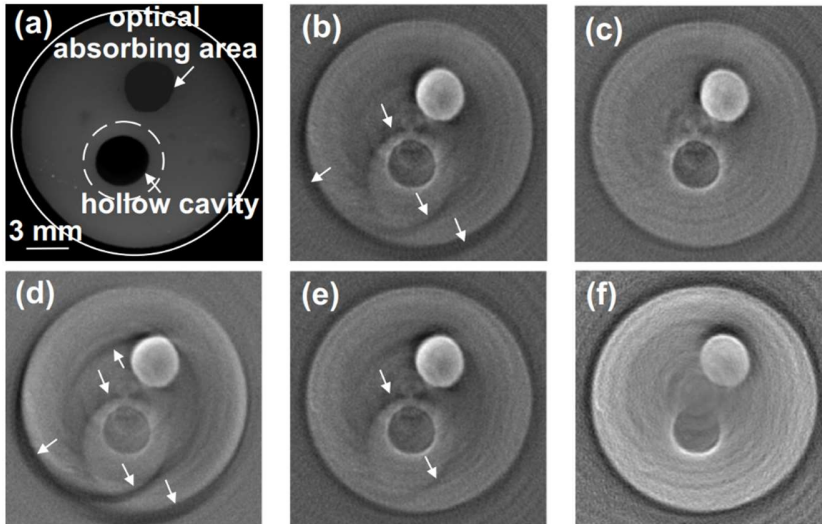

Figure 4.6. Results of validating the wBP+apriori method on a tissue-mimicking phantom. (a) Cross-section of the phantom (photograph). The areas A and B are delineated by the solid and dashed circles, respectively. (b-f) OA reconstructions generated with the wBP+apriori method for (b) $\omega = 1$, (c) $\omega = 2$, (d) with conventional BP, and with wBP (without acoustic *apriori*) for (e) $\omega = 1$, and (f) $\omega = 2$. The white arrows indicate the artefacts due to reflections or scattering of the acoustic waves. *(Source: [159])*

here in (c) and (d), respectively). Due to the good agreement between the respective histograms for $n = 500$ and $n = 50{,}000$, the authors concluded that the values of $P_{\mathrm{r}}^{i}(t_{ij})$ obtained with the Monte Carlo simulation using a relatively small number of iterations were acceptable. The main advantage thereof was that the computational cost of the wBP+apriori method was not significantly increased in comparison with the conventional BP reconstruction [159].
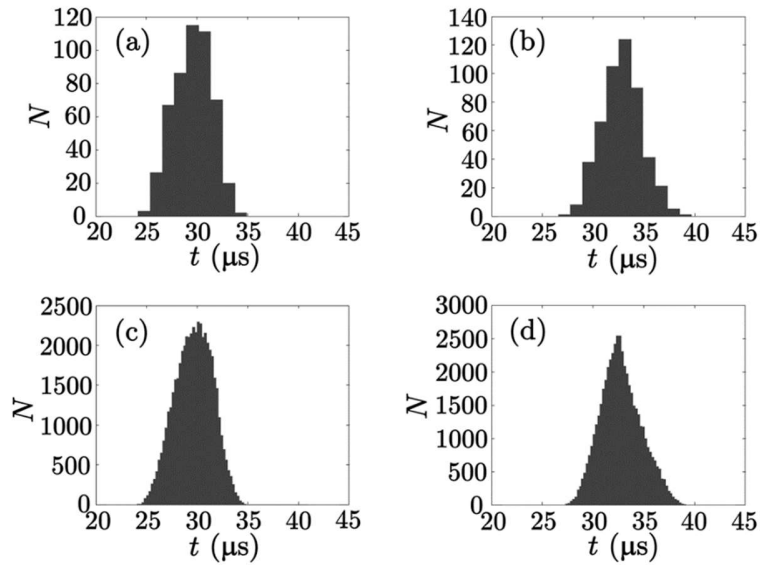

Figure 4.7. Histograms generated by Monte Carlo simulation corresponding to $t_{\mathrm{r}}^{i}(r', r'')$ (the instant of detection of a wave generated at r' and reflected or scattered at r'') for n pairs of points (r', r'') in areas A and B, respectively, for two detector positions. $n = 500$ for (a) and (b), and $n = 50{,}000$ for (c) and (d). The angular positions of the two examined detectors were 46° for (a) and (c), and 270° for (b) and (d). *(Source: [159])*

Coming back to the validation results in Figure 4.6, panels (b) to (f) show a comparison of the tomographic reconstructions yielded with conventional BP and both statistical methods (wBP with and without *a priori*). The optimum ω was estimated heuristically for each case taking into account the trade-off between artefact reduction and image distortion. It could be clearly noticed that the wBP+apriori method was capable of further reducing image artefacts in comparison with the more simplistic wBP without *a priori*, specifically in the region close to the center of the image and for $\omega = 2$ (comparing panel (c) to (f)).

4.3 Statistically-weighted MB (wMB) OA reconstruction

Introducing the aforementioned statistical weighting to BP reconstruction showed promising results regarding the mitigation of reconstruction artefacts due to the presence of strong acoustic heterogeneities in the sample, both when acoustic *a priori* were unknown [158] or available [159]. However, BP OA reconstruction algorithms are generally not adequate for quantitatively estimating the optical absorption distribution [116]. Additionally, BP-based algorithms cannot fully account for the effect of detector geometry on the reconstruction [117]. Consequently, the overall efficiency of the aforementioned statistical approach, applied in combination with BP, was reduced as well. Hence, the authors of this statistical weighting approach decided to introduce the same concept to the MB reconstruction algorithm (Henceforward referred to here as "wMB" reconstruction) [160]. The motivation behind this was that MB reconstruction provides a better quantitative reconstruction performance compared to BP-based methods; which is an important advantage for applications that require accurate image analysis, such as evaluation of biomarker distribution in tissue. Additionally, contrary to other MB reconstruction procedures [126],[164], the IMMI approach (the specific MB reconstruction algorithm to which the authors introduced the statistical weighting, and which was discussed in section 3.2.2) enabled regularization-free reconstruction in the case of full tomographic view, yielding high-resolution images. In such cases, both the signals and the model are weighted so that no additional quantification errors are introduced with this procedure, which is very important if the actual distribution of optical energy must be estimated.

4.3.1 Recap of the basic principle underlying conventional MB reconstruction

In this section we briefly revisit the basics of MB reconstruction (previously discussed in detail in chapter 3), which is based on the discretization of the OA forward model for short-pulsed illumination, given that thermal confinement conditions are fulfilled. In such case, the pressure field due to OA excitation at the initial instant was given by (61) [54]. When cylindrically-focused ultrasonic transducers are utilized, all the OA sources could be assumed to lie in a 2D plane, so that equation (61) could be reduced to a 2D geometry and the integration could be performed over a circumference. The OA reconstruction mainly consists of computing the value of $H(r'_k)$ for pixel positions r'_k in the discrete 2D image. Taking this into account, (61) could be approximated in the discrete domain as

$$p(\boldsymbol{r}_i, t_j) = \sum_{k=1}^{N} a_k^{ij} H(\boldsymbol{r}'_k) \tag{77}$$

where N is the total number of pixels in the reconstructed 2D image. In order to calculate the coefficients a_k^{ij}, $H(r')$ must be calculated in the whole 2D domain by means of interpolation from the values of $H(r'_k)$ at the pixel positions k. Rosenthal et al [116] showed that the coefficients a_k^{ij} can be estimated semi-analytically if the interpolation is performed by tiling the x–y reconstruction plane with right angle triangles with vertices on the pixel positions, so that $H(r')$ could be obtained by linear interpolation inside each triangle (hence the name "interpolated matrix MB inversion" (IMMI)). Dean-Ben et al [165] then proposed a faster method to calculate such coefficients which consisted mainly in approximating the integration circumference by a set of points with equally-spaced angular positions from the detector locations.

The same discretization of equation (61) can be obtained for P positions of the detectors and for I instants, such that a corresponding system of linear equations can be formulated in matrix form as

$$p = A_M H. \tag{78}$$

Equation (78) corresponds to the forward model, in which the theoretical pressure for a set of transducer positions and instants p is calculated as a function of the absorbed energy in the pixel positions H, where A_M is the model matrix with dimensions $PI \times N$. OA inversion is performed by minimizing the mean square difference between the theoretical pressure p and the measured pressure p_m as in the following

$$H_{\mathrm{sol}} = \operatorname*{argmin}_{H} \| p_m - A_M H \|^2 . \tag{79}$$

Equation (79) could be solved by iterative least squares QR decomposition (LSQR) [130], in which the sparsity of A_M could be utilized to make a faster reconstruction. A more comprehensive description of MB inversion can be found in [116].

4.3.2 Statistical weighting of the MB reconstruction algorithm to account for acoustic heterogeneities

Equation (78) was derived assuming that the generated OA waves propagate undisturbed in an acoustically homogeneous medium with constant speed of sound, which is equivalent to direct wave propagation between the OA generation and detection loci. However, if strong heterogeneities are present in the target under investigation, there is a probability that the signal measured at any given detector position and any given instant is distorted by a reflected or scattered acoustic wave.

Similar to the modification of the conventional BP reconstruction algorithm in (72) to introduce the statistical weighting, the authors modified the conventional MB algorithm by weighting each equation of the linear system of equations (77) with the probability $P_{\mathrm{d}}^i(t_{ij})$ (as in (71)) that the signal for the corresponding instant and transducer position is not distorted by reflection or scattering events, in a way that the reconstruction is made preferably with those equations which are more likely to correspond to direct propagation between the excitation and detection points [160]. That is; equation (77) was modified to become

$$P_{\mathrm{d}}^i(t_{ij})p(\boldsymbol{r}_i, t_j) = P_{\mathrm{d}}^i(t_{ij}) \sum_{k=1}^{N} a_k^{ij} H(\boldsymbol{r}'_k) \tag{80}$$

and the matrix form in (78) was correspondingly modified as

$$\boldsymbol{W}\boldsymbol{p} = \boldsymbol{W}\boldsymbol{A}_M\boldsymbol{H} \tag{81}$$

where $\boldsymbol{W}$ is the weighting matrix (with dimensions $PI \times PI$ and with elements $P_{\mathrm{d}}^i(t_{ij})$ on the diagonal and zero otherwise). The OA inversion is then similarly solved by a mean square difference minimization. That is; (79) was modified to become

$$\boldsymbol{H}_{\mathrm{sol}} = \underset{\boldsymbol{H}}{\operatorname{argmin}} \|\boldsymbol{W}\boldsymbol{p}_m - \boldsymbol{W}\boldsymbol{A}_M\boldsymbol{H}\|^2 \ . \tag{82}$$

4.3.3 Experimental validation of wMB reconstruction

The authors of the wMB approach carried out experimental measurements on tissue-mimicking phantoms and a zebrafish *post mortem* in order to evaluate the performance of their proposed modification of the conventional MB approach [160]. The experimental scanner was similar to the setup they used for the validation of the wBP algorithm [158]. Shortly, the illumination source consisted of a short-pulsed laser with tunable wavelength, whose output beam was adapted by

variable optics to generate uniform illumination around the target under investigation. The laser wavelength was set to 605 nm and to 587 nm for phantom and zebrafish measurements, respectively. The generated ultrasonic waves were detected with cylindrically-focused ultrasonic PZT transducers, having 3.5 MHz and 15 MHz central frequencies for the phantom and zebrafish experiments, respectively. In order to acquire 180 projections, the whole sample was rotated over 360° with 2° steps by means of a linear rotation stage. For each projection, the signal was averaged 64 times and band-pass filtered. For further technical details about the OA scanning system used for this validation, the reader was referred to a previous publication [162]. The tissue-mimicking phantoms were also constructed with similar background optical absorption and scattering values to the ones in the wBP publication by means of mixing black India ink and intralipid with an agar solution [158]. Also similarly, regions with higher concentration of ink were included in the phantoms. Air-filled cylindrical straws were also included in the phantoms in order to generate strong acoustic reflections. As for the small-animal imaging, the zebrafish imaged in the experiment (*post mortem*) was 6 months old, and was imaged in a region close to the swim bladder, which contains air gaps and several acoustically mismatched tissues. It was embedded in a pure agar phantom for ease of handling.

The results of the validation of the wMB OA reconstructions of the tissue-mimicking phantoms generated in [160] with conventional MB and the proposed wMB approach (for $\omega = 1$) are shown in the second and third columns of Figure 4.8. The authors as well compared the performance of the wMB algorithm to MB reconstruction based on the half-time methodology, which also have an additional advantage of mitigating reflection artefacts (shown in the fourth column) [166]. For the three phantoms, it could be seen that both methods achieved noticeable reduction of the

reflection artefacts. However, the results produced with half-time MB reconstruction were noisier, and more distortion appeared in the central regions of the images. The authors pointed out that all the images displayed were obtained with no regularization, which could have helped to reduce the noise, but at the expense of some reduction of information in the images, which is generally not desirable for quantification purposes.
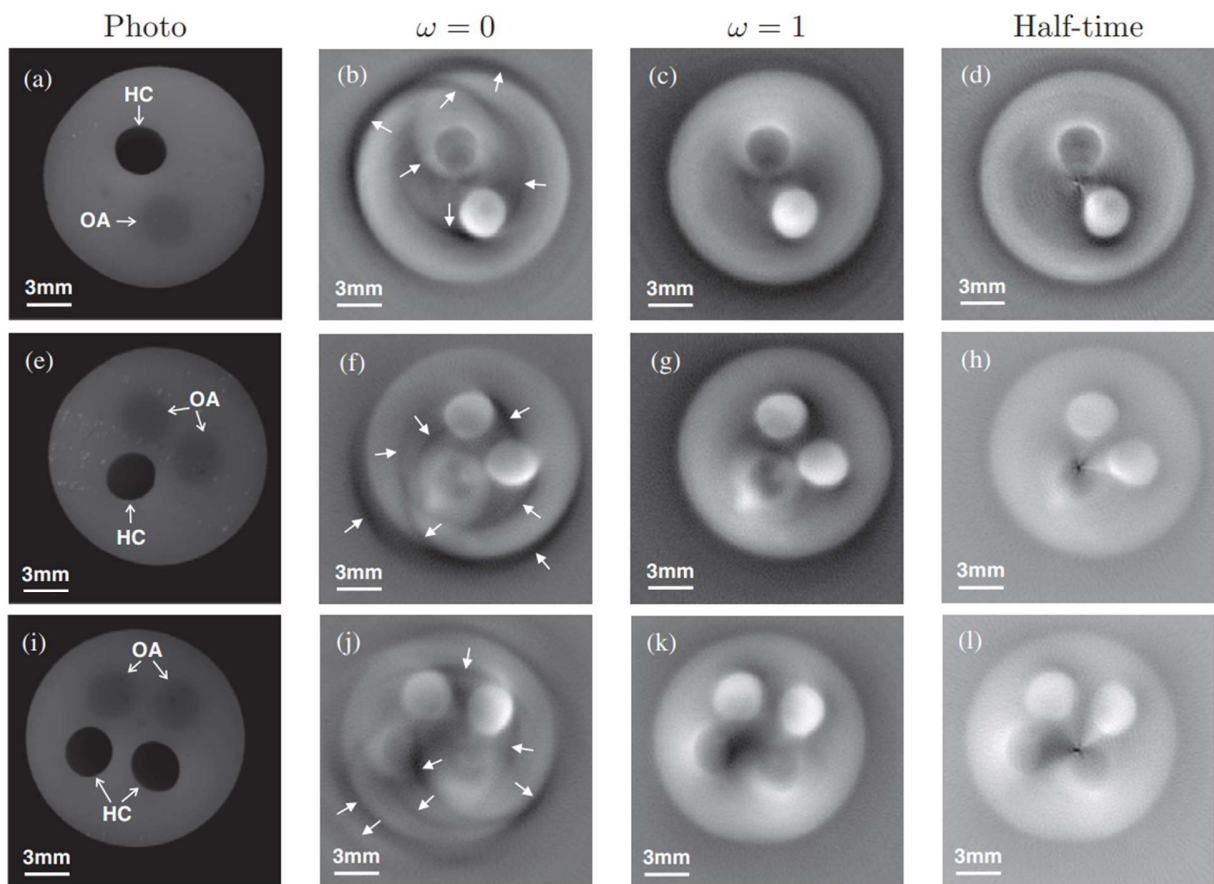

Figure 4.8. Results of the validation of the wMB algorithm on three tissue-mimicking phantoms. The first column of the image shows cross sections of the phantoms (photographs), containing areas with higher optical absorption (OA) and hollow cavities (HC). The second and third columns show OA reconstructions generated with the conventional MB algorithm and with the wMB algorithm, respectively. The fourth column shows the results obtained with MB reconstruction based on the half-time methodology. White arrows indicate reflection artefacts. *(Source: [160])*

As for the validation of the wMB reconstruction in the case of small-animal imaging, the results from [160] of imaging the zebrafish are displayed here in Figure 4.9. Panels (a–c) show the reconstructions obtained with the conventional MB algorithm, (d–f) show the images generated with the wMB algorithm for $\omega = 1$, and (g–i) show the reconstructions obtained with MB reconstruction based on the half-time methodology. The first column show full-view reconstructions, whereas the LV reconstructions obtained by taking into account only a detection
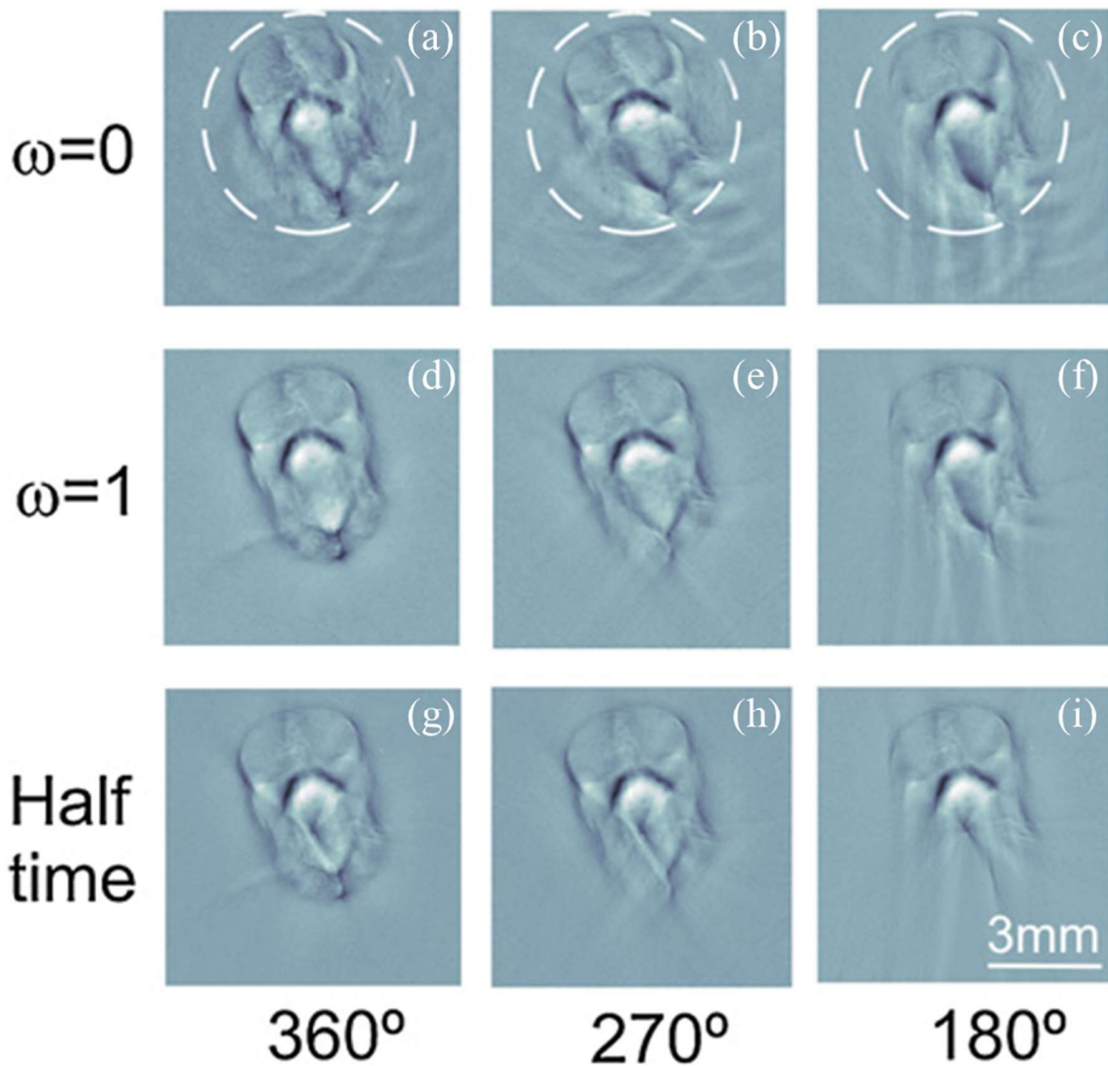

Figure 4.9. Results of the validation of the wMB algorithm on the zebrafish datasets with conventional MB reconstruction (a–c), with wMB reconstruction (d–f), and with MB reconstruction based on the half-time algorithm (g–i). The reconstructions were generated by considering all the measuring locations in a full-view scenario (a), (d), (g), or for a limited view case by taking measuring locations along an arc covering an angle of 270° (b), (e), (h) or 180° (c), (f), (i). The area A was taken as the area inside the dashed circumferences and $\omega = 1$ for all cases. *(Source: [160])*

arc covering an angle of 270° and 180° are displayed in the second and third columns, respectively. Similar to the results of imaging the tissue-mimicking phantoms, both the wMB and the half-time MB algorithms achieved noticeable reduction of reflection artefacts in comparison with conventional MB reconstruction. However, the wMB method performed slightly better for the LV imaging cases (causing less distortion in the lower image areas compared to the half-time MB method).

4.4 statistical approach issues with PV imaging

The statistical weighting discussed in the previous sections showed promising results regarding mitigation of the OA reconstruction artefacts due to presence of strong acoustic heterogeneities in the imaged sample. This potential was apparent when the statistical weighting concept was applied to both BP reconstruction [158], and later to MB reconstruction [160]. The weighted approach was advantageous in comparison with both conventional BP and MB reconstructions particularly in full-view imaging cases. That is; when the detection geometry was fully surrounding the imaged sample in the 2D imaging plane (i.e. total coverage angle = 360°), the weighting approach was able to reduce reflection artefacts without introducing much distortion of its own to the reconstruction results. However, in cases of PV imaging scenarios, where some parts of the imaged sample are not fully covered by the detection geometry, the weighting approach caused distortion in these parts that was noticeable in the reconstruction results.

For example, in [158] where the authors first proposed the statistical weighting principle to BP reconstruction, they also tested it on one of the tissue-mimicking phantoms in the case that the signal was only measured along a trajectory covering less than a 360° arc. Figure 4.10 shows the

resulting reconstructions obtained with conventional BP and modified wBP, where only positions

covering a 180° arc (from 90° to 270°) were considered during solving the acoustic inversion. For

statistical wBP, the weighting parameter $\omega = 1$ and the area A was taken again as the circle

inscribed in the region of interest. It can be seen that in the region located outside the area enclosed

by the detection elements, the amplitude of reconstruction artefacts was reduced with wBP.

However, some distortion was introduced to the right part of the image in (b) which was not well

covered by the detection geometry in this case. Also, later when the authors tested the weighting

principle with MB reconstruction [160] on a zebrafish dataset, some distortion was caused by the

weighting method in the PV cases that was noticeable in the lower part of reconstructed image ((e)
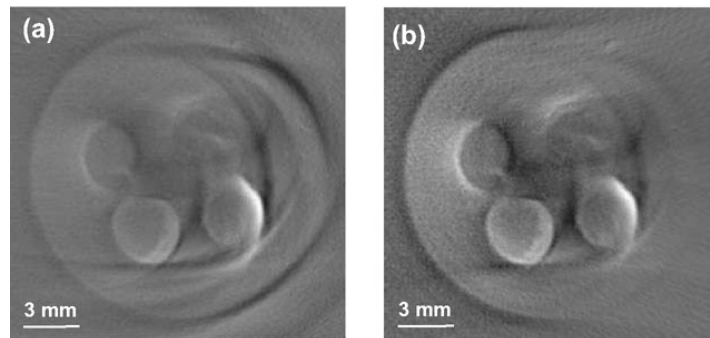
and (f) in Figure 4.9).

Figure 4.10. Results of the validation of the wBP algorithm on a tissue-mimicking phantom in the case of partial-view detection.   The reconstruction was obtained with conventional BP (a) and with wBP ($\omega = 1$)(b). For both cases, only the positions of the transducers from 90° to 270° were considered. *(Source:* [158]*)*

In the following sections, we will discuss a modification that we recently introduced to the

statistical weighting principle in order to address the aforementioned distortion issue in PV

imaging scenarios. Basically, we hypothesized that by suitably manipulating the statistical

weighting scheme to take into account the PV detection geometry, we could enhance the quality

of PV reconstructions using the same weighting principle [161]. As this correction was mainly

targeted for PV imaging cases and we validated for MB reconstruction, we refer to it henceforward as "PVc-wMB" (partial-view-corrected weighted MB) reconstruction.

4.5 PVc-wMB reconstruction

As was demonstrated in the previous sections, the wMB technique mitigates artefacts due to acoustic reflections in tissue-mimicking phantoms and small-animal imaging cases for full-view cross-sectional geometries [158], [160]. For PV geometries however, due to the nature of the weighting scheme, areas in the image that are not fully covered by the detection geometry tend to be severely underweighted. Consequently, the reconstruction at these areas is distorted.

To further illustrate the underweighting problem, we assumed that the PV imaging domain can be represented by the region covered by the 2D detection arc ∂D as in Figure 4.11(a). This circular detection arc is covering only 270° of the 2D imaging plane to resemble the preclinical MSOT system used in this study. The weighting function $P_{\mathrm{d}}^i(t_j)$ could be graphically represented as in (b). For the wMB algorithm, the signal at detector i is multiplied by the weight $P_{\mathrm{d}}^i(t_j)$. Specifically for detectors in the section ∂D_u (indicated by the red bold section of the detection arc ∂D), this weighting approach underweights the detected samples indicated by the red dotted segment for transducer i (corresponding spatially to OA signals originating at locations farther than the center
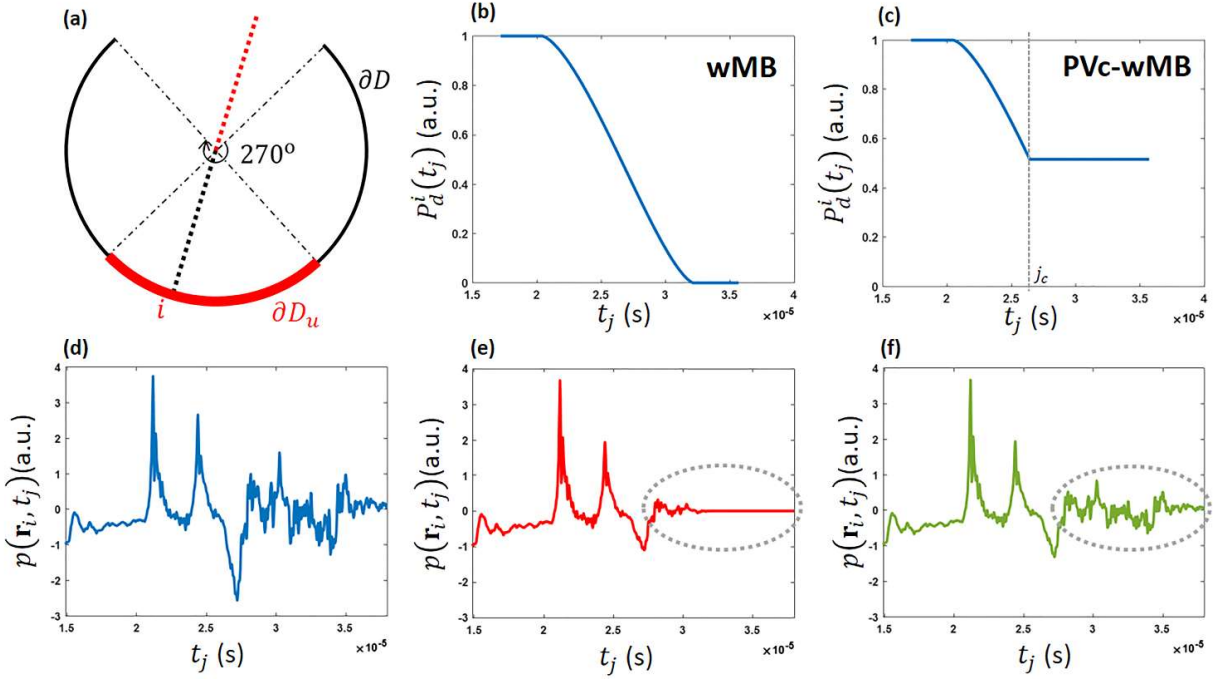
Figure 4.11. Illustrative figures for the theoretical basis of the proposed PVc-wMB algorithm. (a) A diagram of the 270°-PV detection geometry investigated. (b-c) $P_\mathrm{d}^i(t_j)$ plots for transducer i for (b) the wMB, and (c) the proposed PVc-wMB reconstruction algorithms. (d) Detected OA signal for transducer i with no weighting (used in the conventional MB reconstruction). (e-f) The same detected signal for transducer i in (d) after being weighted by $P_\mathrm{d}^i(t_j)$ for (e) the wMB, and (f) the proposed PVc-wMB algorithms.

of the detection circular aperture ∂D). Consequently, image parts corresponding to these underweighted samples are relatively distorted in the final reconstruction. This underweighting can be justified due to two reasons. First, there are no detectors on the opposite side to ∂D_u to compensate for such underweighting. Second, and commonly for such OA scanners, the acoustic detectors and illumination sources are on the same circular aperture (i.e. both the detection and illumination geometries are the same). This leads to a relatively weaker illumination in areas not fully covered by the geometry, aggravating the underweighting problem.

To circumvent the underweighting problem of the wMB algorithm for transducers in ∂D_u, we introduced a modification to the weighting function $P_\mathrm{d}^i(t_j)$ that takes into account the PV geometry

128

[161]. In principle, we manipulated a part of $P_\mathrm{d}^i(t_j)$ to counteract this underweighting effect. That is; we proposed to modify (71) particularly for the affected detectors to become:

$$P_\mathrm{d}^i(t_j) = \begin{cases} \max\left(0, 1 - \omega\left(\dfrac{A_{ij}}{A}\right)\right), & j < j_c \\[2ex] 1 - \omega\left(\dfrac{A_{ij_c}}{A}\right), & j \geq j_c \end{cases} \tag{83}$$

where the instant j_c can be chosen to correspond spatially to the center of the detection circular aperture ∂D. This value for j_c was also the choice for the half-time reconstruction approach published before [166]. This choice was reasonable because the imaged sample is almost always placed in the center of the scanning aperture in order to maintain the homogeneity of both illumination and detection as much as possible for the part covered by the detection geometry. For transducers in ∂D_u, this modification changes the temporal profile of the weighting function $P_\mathrm{d}^i(t_j)$ as in Figure 4.11 from (b) to (c).

To demonstrate how the weighting term $P_\mathrm{d}^i(t_j)$ affects the temporal profile of the detected signals for detectors in ∂D_u for both the wMB and PVc-wMB algorithms, we assumed that the raw detected signal by transducer i in (a) was as shown in (d). If the original wMB weighting (without PVc; as in (b)) is applied to this raw signal, the signal changes to the curve shown in (e). However, if the same weighting, but with the proposed PVc (as in (c)), is applied to the raw signal, it changes to the curve shown in (f). It can be noticed that the detected samples corresponding spatially to OA signals originating at locations farther than the center of the detection circular aperture (indicated by the dotted grey ellipse) are much less flattened in (f) compared to (e). This demonstrated how incorporating the proposed PVc in the wMB algorithm can alleviate the aforementioned underweighting issue in PV OA imaging scenarios.

4.5.1 Experimental Setup and Datasets to evaluate the proposed PVc-wMB method

In order to evaluate the performance of the proposed PVc-wMB reconstruction algorithm, both phantom and *in vivo* experiments were carried out using a commercial preclinical MSOT scanner (MSOT256-TF, iTheraMedical GmbH, Munich, Germany). In this system, a wavelength-tunable Nd:Yag pump optical parametric oscillator-based laser provides pulsed excitation between 680-980 nm with a pulse width of about 10 ns, repetition rate of 10 Hz, and per-pulse energy of about 90 mJ. The optical output is shaped by means of a fiber bundle to provide a 2D ring-like cross-sectional illumination. The acoustic detection part of this system consists of a 256-element concave array of cylindrically-focused piezoelectric transducers with a central frequency of 5 MHz, a radius of curvature of 40 mm and an angular coverage of approximately 270° (hence the PV problem) [86], [167].

Phantom Dataset

A tissue-mimicking phantom was prepared to illustrate the nature of the artefacts produced due to the presence of a strong acoustic heterogeneity. To achieve this purpose, a cylindrically-shaped absorbing inclusion and a hollow cylindrical cavity are included in the phantom. The optical absorption of the absorbing inclusion was obtained by adding India ink to an agar solution (corresponding approximately to an optical absorption coefficient μ_a of 1.2 cm^{-1} at 680 nm). The background optical absorption and scattering were achieved by mixing India ink and intralipid with an agar solution. This corresponded to an approximate optical absorption coefficient μ_a of 0.1 cm^{-1} at 680 nm and an approximate reduced scattering coefficient $\mu_s^{'}$ of 7 cm^{-1}. These values

were chosen to approximate average light fluence attenuation in biological soft tissues [168]–[170]. This phantom was imaged at several optical wavelengths between 680 and 980 nm.

in vivo Datasets

All animal handling protocols were performed under supervision of trained personnel in accordance with institutional and local guidelines and with the approval of the Government of Upper Bavaria, Germany. Mice were housed in an animal housing facility (21±2 °C, 36%±2% humidity) on a 12/12-h light/dark cycle at the Institute of Biological and Medical Imaging, Helmholtz Zentrum München (Munich, Germany). During the experiments, the mice were sedated (1.8% isoflurane in 100% O_2 at 0.81 ml/min) and immersed in a water bath kept at approximately 33 °C using a specialized mouse holder (iThera Medical GmbH, Munich, Germany).

To investigate the performance of the proposed PVc-wMB reconstruction algorithm *in vivo* when the acoustic reflector is localized within the same region as the optical chromophores, we used a dataset (hereinafter referred to as "dataset 1") acquired previously by our research group from a BALB/c nude mouse (Charles River Laboratories, Boston, MA, USA) bearing a mammary tumor xenograft. The animal was injected in its backside with 4T1 cells (8×10^5 cells; CRL-2539, American Type Cell Culture Collection, Manassas, VA, USA), and the xenograft was allowed to grow for several days, until it reached a size of 100 mm³. Then the animal was injected intravenously with Rhodobacter sphaeroides (1×10^9 CFU) [171], [172]. At 24 h later, the torso region was imaged at 25 wavelengths between 680 and 920 nm. This anatomical section was chosen because the spine acts as a strong source of acoustic reflections within the chromophore region.

In order to investigate the performance of the PVc-wMB algorithm when the acoustic reflector surrounds the chromophores, we tested it on a dataset (hereinafter referred to as "dataset 2") which our research group had previously acquired from the intact brain of a young adult mouse (Hsd:Athymic Nude-Foxn1nu/nu) at 805 nm. This wavelength was chosen because it is close to the isosbestic point for hemoglobin. In this case, the intact skull provided a strong acoustic reflector that surrounds the chromophores inside the brain. Further details about the experimental procedure can be found in the previous publication [173].

To demonstrate the additional advantage of the PVc-wMB algorithm of suppressing streaking artefacts arising from strong OA generation in the case of PV detection scenarios, we tested it on a dataset (hereinafter referred to as "dataset 3") that we acquired from an 8-week-old female athymic Nude-Foxn1-/- mouse (Envigo, Huntingdon, UK) bearing a 4T1 tumor. 4T1 cells (American Type Culture Collection) were cultured in RPMI-1640 medium (Sigma) supplemented with 10% fetal bovine serum (Gibco) and 1% penicillin-streptomycin (Sigma). Cells (0.25×10^6) were inoculated orthotopically into the right third thoracic mammary fat pad of the mouse, and allowed to grow for 15 days, until the tumor reached a diameter of 1 cm (~0.5 cm^3 in volume). The transversal section of the tumor with the longest diameter, corresponding to its anatomical center, was imaged on the last day (day 15) at 27 wavelengths between 700 and 960 nm. The skin on the tumor ulcerated on the day of imaging and consequently, coagulated blood on the surface of the ruptured skin produced a very strong OA signal, causing a severe streaking artefact. Although this ulceration was unintentional, it provided a good opportunity to evaluate the proposed

PVc-wMB algorithm. It is important to note that this streaking artefact was not due to the presence of acoustic heterogeneities in the imaged sample, but rather due to the PV geometry itself.

Quantitative and Multispectral Data Analysis

As contrast is an important factor of determining whether a region can be differentiated from the background, we used the CNR measure to quantify the improvement achieved by the PVc-wMB reconstruction in the contrast of the upper boundary of the phantom that was particularly distorted by the wMB algorithm due to the PV detection geometry. The CNR is defined as follows [174]:

$$CNR = \frac{|\mu_{ROI} - \mu_{BGD}|}{\sqrt{\sigma_{ROI}^2 + \sigma_{BGD}^2}} \tag{84}$$

where μ_{ROI}, μ_{BGD} and σ_{ROI}, σ_{BGD} are the means and standard deviations of a given ROI and BGD, respectively, both with homogenous intensities.

To demonstrate the spectral performance of the proposed PVc-wMB reconstruction algorithm, spectral unmixing was performed after acoustic reconstruction using linear least-squares spectral fitting for *in vivo* datasets 1 and 3 [143], [175]. This is a conventional spectral unmixing model in the OA literature, in which the measured spectrum at any pixel is assumed to be a linear combination of distinctive spectral components [68], [176]. For the multispectral datasets 1 and 3, oxy- and deoxy-hemoglobin spectral components were unmixed in image areas where reflection and streaking artefacts, respectively, were apparent. Then, oxygen saturation (sO_2) values at the respective pixels were calculated based on the unmixed spectra.

4.5.2 Results of the experimental validation of the proposed PVc-wMB algorithm

The performance of the proposed PVc-wMB reconstruction algorithm was compared to that of the conventional MB algorithm and the unmodified wMB algorithm, first for the simplified case of the tissue-mimicking phantom, and then for the three *in vivo* datasets. Before investigating the results, it is important to know that the value of the heuristic parameter ω was kept at 1 for all datasets investigated in this paper, as it maintained the best compromise between mitigating artefacts (as will be shown later) and avoiding smearing the overall reconstruction for most cases, and also to focus more on studying the effect of the introduced PVc. Additionally for the *in vivo* dataset 3, we investigated the effect of reducing ω on the smearing of structures in the center of the image that was induced by the weighting scheme.

Phantom Validation

The three algorithms were compared with regard to their ability to reconstruct the phantom shown in Figure 4.12(a), containing an optical chromophore and a strong acoustic reflector. Panel (b) shows the OA reconstruction using the conventional MB algorithm, where typical arc-like reflection artefacts (indicated by the red arrows) are noticeable. Panel (c) shows the OA reconstruction with the unmodified wMB algorithm, which mitigated the reflection artefacts but also caused severe distortion in the upper boundary of the phantom (enclosed by the dotted ellipse), which was not fully covered by the detection geometry. Panel (d) shows the reconstruction with the proposed PVc-wMB algorithm, which recovered the upper distorted boundary of the phantom without compromising the capability of the wMB algorithm to mitigate the arc-like reflection artefacts. Panel (e) shows the intensity profile along the line l_1 across the arc-like artefact in (b). The wMB weighting scheme by itself mitigated this artefact, and the proposed PVc-wMB
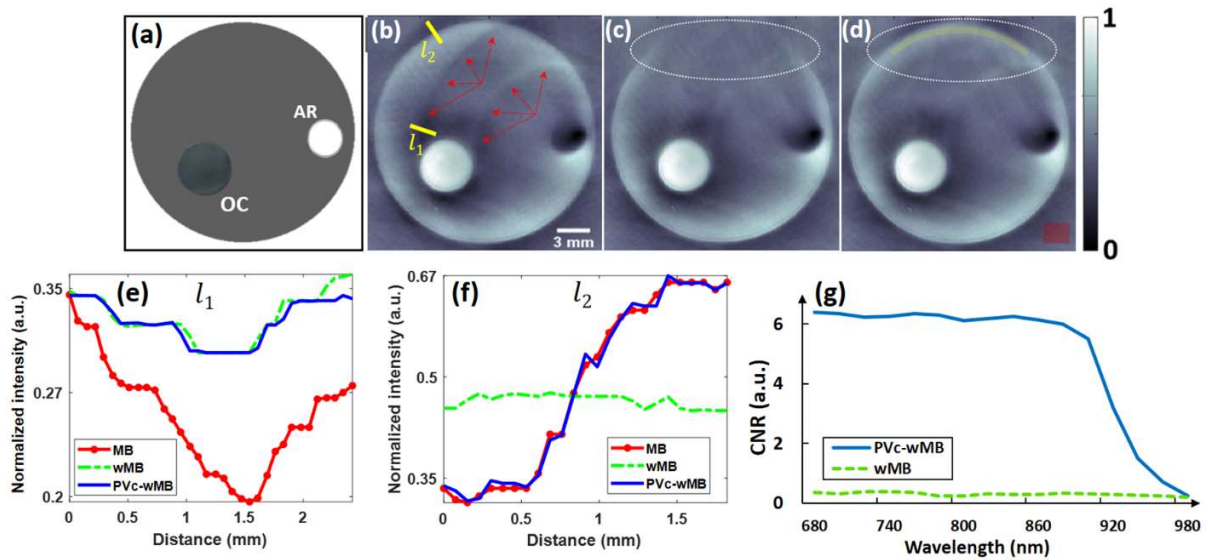

Figure 4.12. Anatomical performance of the PVc-wMB algorithm for the tissue-mimicking phantom. *Upper row:* (a) A schematic cross-section of the phantom. OC, optical chromophore; AR, acoustic reflector. (b-d) OA reconstruction of the phantom using (b) MB, (c) wMB, and (d) PVc-wMB algorithms. Red arrows in (b) indicate typical arc-like reflection artefacts. l_1 and l_2 are lines taken for intensity profile analysis in (e) and (f), respectively. Dotted ellipses in (c) and (d) indicate the area not fully covered by the detection geometry. Light-yellow arc and light-red square in (d) indicate the ROI and BGD regions, respectively, used for CNR calculation in (g). *Lower row:* (e-f) Intensity profiles for lines (e) l_1 and (f) l_2 from (b). (g) CNR plots based on the ROI & BGD regions indicated in (d).

algorithm maintained this mitigation as well. Panel (f) shows the intensity profile along the line l_2 across the upper edge of the phantom in (b). The proposed PVc recovered this edge of the phantom that was visible in the conventional MB reconstruction in (b), reversing the distortion caused by the wMB algorithm in (c). Panel (g) shows the CNR values for the wMB and PVc-wMB reconstructions acquired with different illumination wavelengths. The CNR was calculated taking into account that the ROI and BGD regions are those indicated by the light-yellow arc and light-red square, respectively, in (d). This ROI was particularly chosen because it represents the region with homogenous intensity (theoretically) that is particularly distorted by the wMB algorithm, but recovered by the PVc-wMB algorithm. As shown in (g), the PVc-wMB algorithm maintains a considerably higher CNR for most of the wavelength range, compared to the wMB algorithm alone. The steep drop of the CNR for the PVc-wMB reconstructions starting around 890 nm is due to the fact that the increasing optical absorption of water surrounding the imaged sample starts to significantly affect the overall reconstruction quality as the image becomes much noisier and contrast is lost all over the image.

in vivo Validation

Next, we compared the performance of the PVc-wMB algorithm with that of the conventional MB algorithm for reconstructing OA *in vivo* data. Figure 4.13 shows the three datasets, each presenting a different challenge for accurate OA reconstruction.
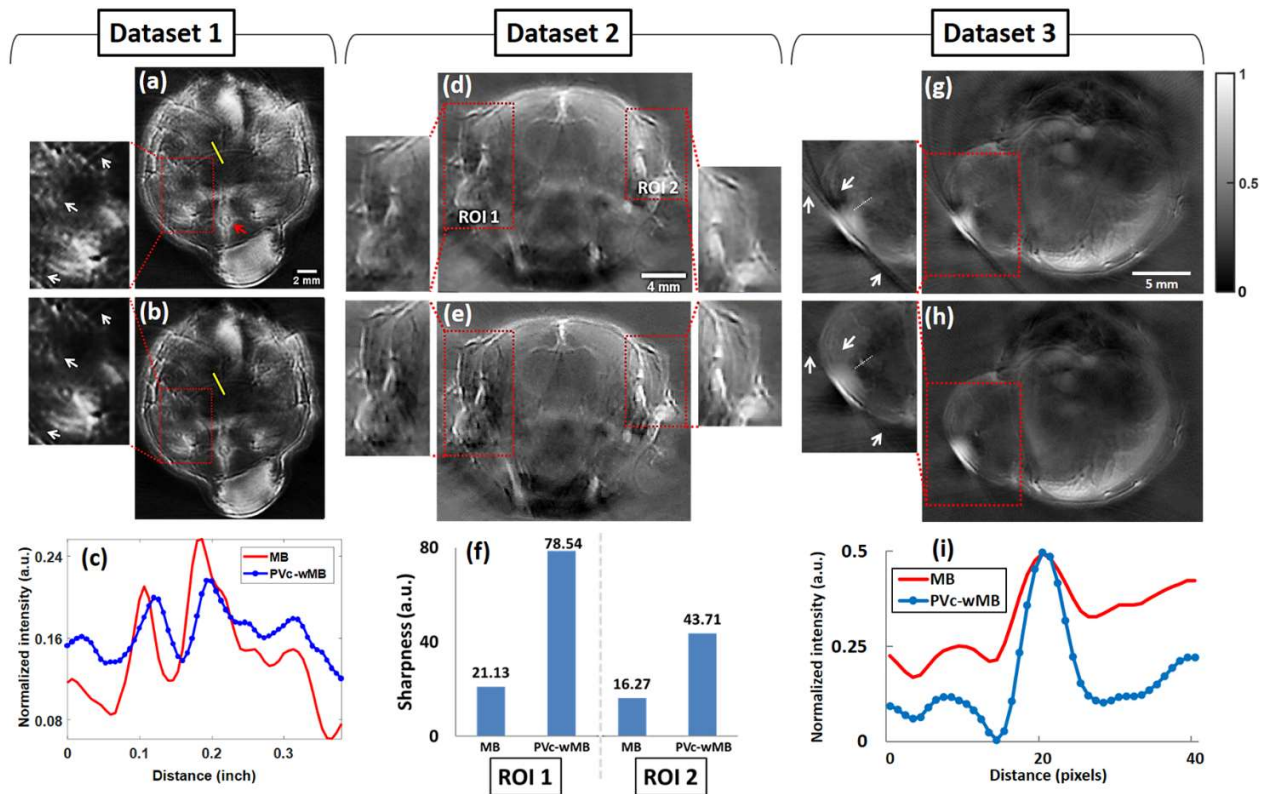
Figure 4.13. Anatomical performance of the PVc-wMB algorithm for the three *in vivo* datasets. *First column:* OA reconstructions of dataset 1 using (a) MB and (b) PVc-wMB algorithms. The red arrow in (a) indicates the spine. White arrows in the side insets of (a) and (b) indicate typical reflection artefacts. (c) Intensity profile along the yellow line taken across the reflection artefact in (a) and (b). *Second column:* OA reconstructions of dataset 2 using (d) MB and (e) PVc-wMB algorithms. The side insets indicate two ROIs used for further sharpness analysis. (f) Sharpness measures of the two ROIs in (d) and (e). *Third column:* OA reconstructions of dataset 3 using (g) MB and (h) PVc-wMB algorithms. White arrows in the side insets indicate typical streaking artefacts due to the very strong OA generation by coagulated blood. (i) Intensity profile along the dotted line taken across the small vessel in the side insets of (g) and (h).

In dataset 1, the spine (indicated with the red arrow in (a)) acted as a strong acoustic reflector inside the mouse. Comparison of the magnified insets of (a) and (b) shows that the proposed PVc-wMB algorithm mitigates the reflection artefact (indicated by the white arrows). Panel (c) confirms this mitigation by showing less intensity variations along the yellow profile line across the reflection artefact in (a) and (b). This mitigation of the reflection artefact was achieved without causing distortion of the upper part of the image, which was not fully covered by the detection geometry.

137

In the case of dataset 2, the skull acted as a strong acoustic reflector surrounding the OA chromophores. Visual inspection of (d) and (e) and the two magnified ROIs demonstrates that the PVc-wMB reconstruction has qualitatively a higher overall sharpness. Panel (f) confirms this increase of sharpness quantitatively based on the Brenner's gradient of sharpness [177].

In dataset 3, a blood vessel within the tumor ruptured near the skin and released blood that coagulated, creating a strongly absorbing chromophore that gave rise to streaking artefacts in the subsequent OA reconstruction. Although such streaking artefacts arise from the PV detection geometry itself and not from acoustic heterogeneities, the proposed PVc-wMB algorithm was able to suppress them as well. Comparison of (g) and (h) demonstrates that the proposed algorithm significantly suppressed the streaking artefacts around the coagulated blood (indicated with the white arrows), again without introducing distortion in the upper image part which was not fully covered by the detection geometry. This streaking suppression led to enhancing the delineation of the tumor boundary. Panel (i) shows the intensity profile across a blood vessel within the tumor (indicated with the small dotted line in the magnified insets of panels (g) and (h)), further demonstrating the ability of the proposed algorithm to reproduce fine anatomical details with relatively higher contrast.

For dataset 3, however, we noticed that the PVc-wMB reconstruction for $\omega = 1$ caused slight smearing of some of the image parts in the center. This smearing can be better visualized in Figure 4.14(d), which shows the absolute difference image between the MB reconstruction (from Figure 4.13(g)) and the PVc-wMB reconstruction for $\omega = 1$ (Figure 4.13(h), also shown in Figure 4.14 (a)). A similar smearing of some of the image parts in the center for the small animal imaging

results was also reported in [158] (where the statistical weighting scheme was first introduced to BP reconstruction). There, the smearing started to become noticeable with values of ω more than 1. Reducing the value of ω could reduce such smearing. For our *in vivo* dataset 3, and in comparison with (d), this reduction of smearing can be noticed in (e) and (f), which are the difference images between the MB reconstruction and the PVc-wMB reconstructions for $\omega = 0.8$ (b) and $\omega = 0.5$ (c), respectively. This reduction of smearing for ω values less than 1 was attained while still maintaining acceptable suppression of the streaking artefact around the ulceration area. It has to be pointed out that because ω is a heuristic parameter, and also due to the statistical nature of the weighting scheme, it is up to the user to select the value of ω that achieves the best compromise between mitigating artefacts and maintaining minimal smearing of true image information for any given dataset.
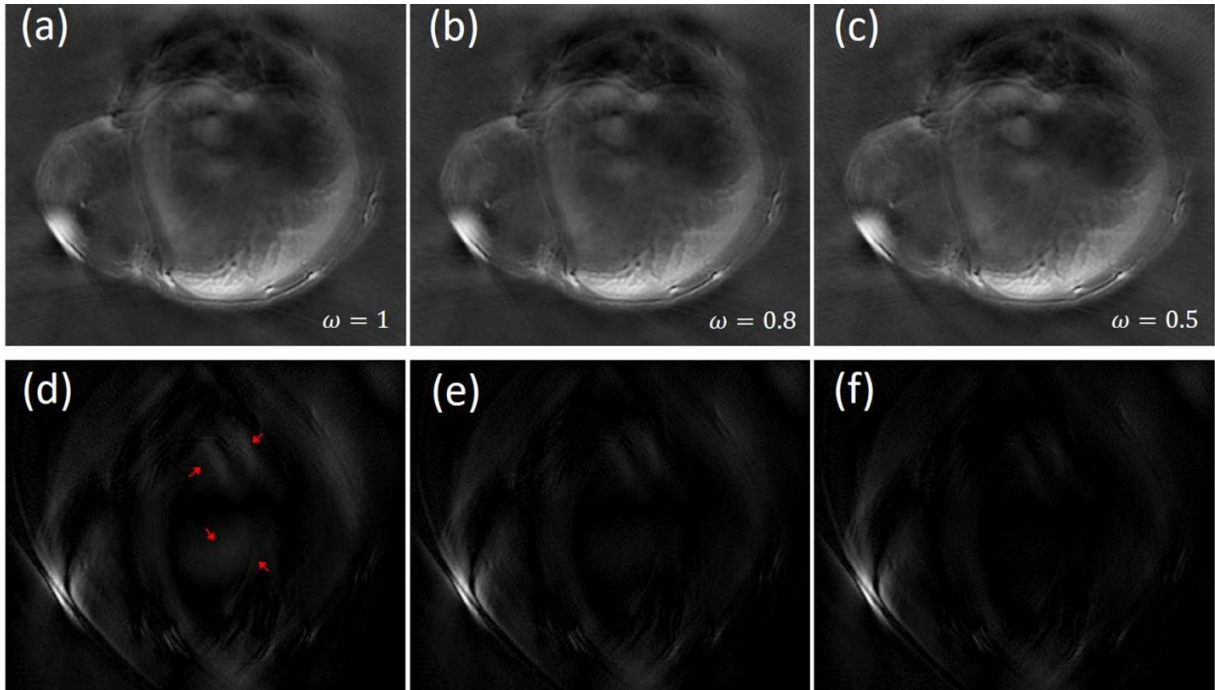
Figure 4.14. Effect of reducing ω on the appearance of internal parts for the *in vivo* dataset 3. *Upper row:* PVc-wMB reconstructions at (a) $\omega = 1$, (b) $\omega = 0.8$, and (c) $\omega = 0.5$. *Lower row:* Absolute difference images between the MB reconstruction (Figure 4.13(g)) and the PVc-wMB reconstructions at (d) $\omega = 1$, (e) $\omega = 0.8$, and (f) $\omega = 0.5$. Red arrows in (d) indicate internal parts that were slightly smeared in (a). Such smearing was reduced by reducing ω as can be noticed in (e) and (f).

Validation of spectral unmixing

The results for *in vivo* reconstruction suggest that the PVc-wMB algorithm can improve the anatomical quality of reconstructed images. We further investigated whether the proposed method could improve spectral unmixing results in order to generate more reliable mapping of functional measures such as the sO_2. Hence, we compared the spatial estimation of sO_2 in areas of the abovementioned mouse tumor images showing a reflection artefact (dataset 1) and a streaking artefact (dataset 3) as shown in Figure 4.15. Comparison of (a) and (b) indicates that the PVc-wMB mitigated the spectral signature of the reflection artefact observed in the conventional MB reconstruction (indicated by the black arrows in the side insets). Similarly, comparison of (c) and (d) shows that the PVc-wMB also suppressed the spectral signature of the streaking artefact

(indicated by the black arrows in the side insets), thus enhancing the delineation of the spectral signature of the tumor, similar to what was observed anatomically in Figure 4.13(h).
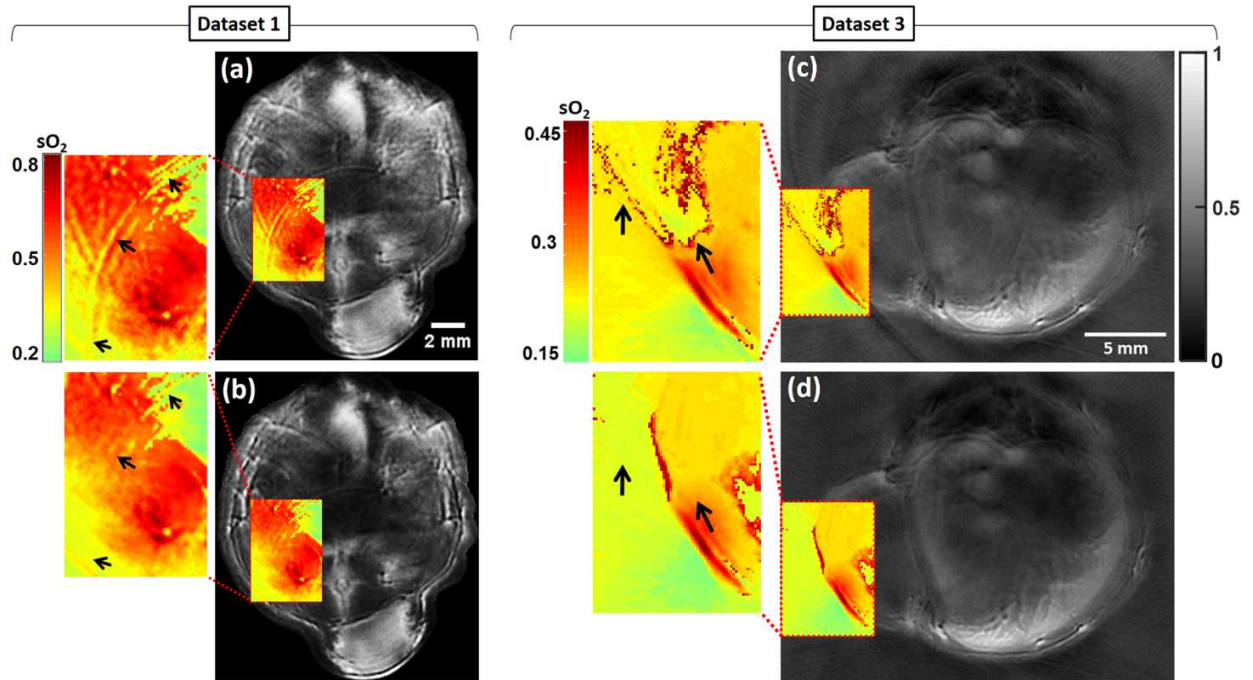

Figure 4.15. Spectral unmixing performance of the PVc-wMB reconstruction for two *in vivo* datasets.   *Left column:* Overlay of spectral unmixing (sO_2 map) of an ROI on reconstructions of dataset 1 using (a) MB, and (b) PVc-wMB algorithms. The side insets show zoomed images of the ROI affected by the reflection artefact. Black arrows in the insets indicate sO_2 signatures of reflection artefacts.   *Right column:* Overlay of spectral unmixing (sO_2 map) of an ROI on reconstructions of dataset 3 using (c) MB, and (d) PVc-wMB algorithms. The side insets show zoomed images of the ROI affected by the streaking artefact. Black arrows in the insets indicate sO_2 signatures of the streaking artefacts.

5.   SUMMARY & OUTLOOK

In chapter 1, we overviewed a couple of mainstream imaging modalities like X-ray, MRI, and ultrasound. Such modalities proved themselves as the go-to diagnostic tools for the clinician. Afterwards, we briefly overviewed other modalities under the general category of optical imaging that cover spatial resolutions both in the microscopic and tomographic scales, such as optical diffuse imaging, confocal microscopy, two-photon microscopy, and optical coherence tomography. Then, we went through single-wavelength and multispectral OA tomography, two of the OA image acquisition methods, and how they could be utilized in preclinical and clinical imaging applications.

In chapter 2, the physical and technical hardware aspects for OA imaging were presented. Starting with a discussion of light and ultrasound behavior in biological tissue, it was further explained how OA signals are generated, as well as properties of OA signals and directivity effects due to diffraction. It was also specified that in OA imaging contrast is based on optical absorption, whereas resolution stems from the emitted ultrasound waves and thus is independent of light scattering. Moreover, an analytical estimate for OA signal strength expected in a small animal imaging scenario was given, being in the range of several tens of Pascals, depending on their locations, size and absorption coefficient. Then, general aspects of OA instrumentation were discussed. Since OA signals are weak, signal-to-noise ratio is a crucial factor. For whole-body

mouse imaging, it is therefore important to maximize light delivery to deep tissue structures, which can be achieved by an optimized illumination scheme, high pulse energies (within the laser safety standards), and wavelengths in the NIR. Nanosecond pulsed lasers with OPO based wavelength tuning are particularly suited for that, since they provide high pulse energies and fast wavelength change. With respect to signal detection, piezocomposite transducer arrays have the advantage that they can be produced in arbitrary shapes adapted to the specific imaging task and parallelized for high frame-rate imaging. It was also shown that the detection system distorts the shape of the detected OA signal by its electrical (EIR) and spatial impulse response (SIR). Thus it is important that the detection device is sufficiently broadband to avoid signal distortion, sensitive and with a sufficiently large dynamic range to capture both the weak OA signals from deep inside tissue and the stronger signals close to the illuminated surface.

In chapter 3, algorithmic & technical aspects of OA image formation were discussed. OA images can be obtained by using focused transducers & tomographic reconstruction methods. For OA image reconstruction, the BP algorithm and the 2D MB inversion scheme were reviewed, followed by a discussion of the spatial resolution and the artefacts due to limited views with the goal of providing an understanding of the effects associated with the different detection parameters. Consequently, it is necessary to match the bandwidth of the detection system to the targeted resolution and the dimensions of the target features to be scanned when designing an imaging system. In addition, it was shown that 2D MB reconstructions suffer from stripe-like artefacts in LV scenarios. In this chapter, their physical underpinning was explained, and a direct and an iterative regularization approach were reviewed that help mitigate such artefacts in OA reconstructions utilizing LV imaging scanners.

The consequences of acoustic heterogeneities in the imaged sample on the reconstructed OA image and how to mitigate such effects were the key topics of chapter 4. We examined a statistical weighting technique that was first applied to BP reconstruction and then to MB reconstruction previously by colleagues in our research group with the goal of reducing artefacts in the OA reconstruction result caused by the existence of strong acoustic heterogeneities in the target under investigation. Next, we examined the challenge of applying such statistical technique in PV imaging cases. Then, in order to improve the applicability of this statistical weighting approach in PV detection geometries in the context of MB image reconstruction, we discussed a corrective technique that we recently published to address such artefacts.

Moving forward, there are a couple of points that can be addressed in future work, building on our adaptation of the statistically-weighted reconstruction approach for PV imaging. Overall, the proposed PVc-wMB algorithm achieved better reconstruction results in comparison with the conventional MB algorithm by mitigating reflection and/or streaking artefacts. This enhancement was achieved without sacrificing reconstruction quality and causing distortions in image sections not fully enclosed by the PV detection geometry, in comparison with the unmodified wMB algorithm. Additionally, the proposed PVc-wMB algorithm maintains the inherent advantage of the wMB algorithm of not requiring prior knowledge of the exact locations or distribution of OA chromophores or acoustic heterogeneities, thus giving it a wide variety of applications. However, it may be possible to further improve its reconstruction performance by including such priors. As shown in chapter 4, the same statistical weighting scheme applied in the wMB algorithm was previously integrated into BP reconstruction taking into account the locations of strong acoustic

heterogeneities as acoustic priors. The inclusion of such priors enhanced the mitigation of reflection artefacts compared to the case where no priors were integrated, especially in the central regions of the image. Therefore, we expect that the proposed PVc-wMB algorithm may also benefit from taking into account optical and acoustic priors in order to mitigate reflection and/or streaking artefacts more effectively. Specifically, the inclusion of acoustic priors (e.g. loci of strong acoustic reflectors) can be facilitated by means of pure ultrasound imaging in recent MSOT machines in which both US & OA imaging are achieved using the same transducer array (aka. hybrid OA & UltraSound (OPUS) imaging systems) [178]. Another potential issue for future investigation is to compare the PVc-wMB algorithm with other non-negative reconstruction approaches [179], [180] particularly for the ability to suppress streaking artefacts in PV detection geometries.

Also, as shown in chapter 4, the improvement achieved by PVc-wMB reconstruction in anatomical imaging performance was accompanied by enhanced spectral unmixing results for *in vivo* datasets, potentially leading to more reliable sO_2 estimates and better differentiation between normal and malignant tissue. However, for a more rigorous analysis of the effect of the proposed algorithm on spectral unmixing, tissue-mimicking phantom experiments with dyes having unique spectral signatures (e.g. Indocyanine green) would be required so that a "ground-truth" spectral map can be established, to which results can be reliably compared. Such analysis is worthy to be considered for future work.

In conclusion, the augmented PVc-wMB algorithm, that was recently published and was discussed in the end of chapter 4, has the potential to increase the quality of preclinical and clinical MSOT

applications, such as tumor imaging and non-invasive brain imaging. The ability of the proposed algorithm to improve the reconstruction of not only anatomical but also functional information can further support the integration of OA imaging into research and clinical workflows that widely utilize PV imaging scanners.

LIST OF FIGURES

150

BIBLIOGRAPHY

[1]   Gordon H Guyatt, "Evidence-based medicine," *ACP Journal Club*, vol. 114, no. 2, p. A16, 1991, doi: 10.7326/ACPJC-1991-114-2-A16.

[2]   D. M. Eddy, "Evidence-based medicine: a unified approach," *Health Aff (Millwood)*, vol. 24, no. 1, pp. 9–17, Jan. 2005, doi: 10.1377/HLTHAFF.24.1.9.

[3]   J. D. Enderle and J. D. Bronzino, "Introduction to Biomedical Engineering," *Introduction to Biomedical Engineering*, pp. 1–1253, 2011, doi: 10.1016/C2009-0-19716-7.

[4]   N Barrie Smith and A Webb, *Introduction to medical imaging: physics, engineering, and clinical applications*, no. 5. 2010.

[5]   W. G. Bradley, "History of Medical Imaging," in *Proceedings of the American Philosophical Society*, 2008, vol. 152, no. 3, pp. 349–361.

[6]   R. A. Robb, *Biomedical imaging, visualization, and analysis*. John Wiley & Sons, Inc., 1999.

[7]   B. Natt, H. M. Szerlip, and L. L. Hamm, "The Lost Art of the History and Physical," *The American Journal of the Medical Sciences*, vol. 348, no. 5, pp. 423–425, Nov. 2014, doi: 10.1097/MAJ.0000000000000326.

[8]   J. F. G. Boo, "Auscultation of the heart: an art on the road to extinction," *Gaceta Médica de México*, vol. 151, no. 2, pp. 260–265, Mar. 2015, Accessed: Aug. 14, 2022. [Online]. Available: www.anmm.org.mx

[9]   W. C. Röntgen, "Ueber eine neue Art von Strahlen," *Ann Phys*, vol. 300, no. 1, pp. 12–17, Jan. 1898, doi: 10.1002/ANDP.18983000103.

[10] Clyde A. Brant and William E.; Helms, *Fundamentals of diagnostic radiology*, no. 2. Philadelphia: Lippincott Williams & Wilkins, 2007.

[11] D. S. Evangelopoulos, S. Deyle, H. Zimmermann, and A. K. Exadaktylos, "Personal experience with whole-body, low-dosage, digital X-ray scanning (LODOX-Statscan) in trauma," *Scandinavian Journal of Trauma, Resuscitation and Emergency Medicine*, vol. 17, no. 1, pp. 1–5, Sep. 2009, doi: 10.1186/1757-7241-17-41/FIGURES/3.

[12] E. C. Beckmann, "CT scanning the early days," *Br J Radiol*, vol. 79, no. 937, pp. 5–8, Jan. 2006, doi: 10.1259/BJR/29444122.

[13] Johann Radon, "Über die Bestimmung von Funktionen durch ihre Integralwerte längs gewisser mannigfaltigkeiten," *Ber. Sächs. Akad. Wiss*, pp. 262–277, 1917.

[14] H. Wang *et al.*, "Improving soft-tissue contrast in four-dimensional computed tomography images of liver cancer patients using a deformable image registration method," *Int J Radiat Oncol Biol Phys*, vol. 72, no. 1, pp. 201–209, Sep. 2008, doi: 10.1016/J.IJROBP.2008.04.054.

[15] W. R. Webb, W. E. Brant, and N. M. Major, *Fundamentals of body CT*. Elsevier Health Sciences, 2014.

[16] A. B. de González and S. Darby, "Risk of cancer from diagnostic X-rays: Estimates for the UK and 14 other countries," *Lancet*, vol. 363, no. 9406, pp. 345–351, Jan. 2004, doi: 10.1016/S0140-6736(04)15433-0.

[17] D. J. Brenner and E. J. Hall, "Computed tomography--an increasing source of radiation exposure," *N Engl J Med*, vol. 357, no. 22, pp. 2277–2284, Nov. 2007, doi: 10.1056/NEJMRA072149.

[18]   E. Odeblad and G. Lindstrom, "Some preliminary observations on the proton magnetic resonance in biologic samples," *Acta radiol*, vol. 43, no. 6, pp. 469–476, Jun. 1955, doi: 10.3109/00016925509172514.

[19]   P. C. Lauterbur, "Image Formation by Induced Local Interactions: Examples Employing Nuclear Magnetic Resonance," *Nature 1973 242:5394*, vol. 242, no. 5394, pp. 190–191, 1973, doi: 10.1038/242190a0.

[20]   "ANSI/ASA Standard Acoustical & Bioacoustical Terminology Database," 1994. https://asastandards.org/working-groups-portal/asa-standard-term-database/ (accessed Aug. 14, 2022).

[21]   R. S. C. Cobbold, *Foundations of biomedical ultrasound*. Oxford University Press, 2006.

[22]   M. Häggström, "Medical gallery of Mikael Häggström 2014," *WikiJournal of Medicine*, vol. 1, no. 2, 2014, doi: 10.15347/WJM/2014.008.

[23]   A. Carovac, F. Smajlovic, and D. Junuzovic, "Application of Ultrasound in Medicine," *Acta Informatica Medica*, vol. 19, no. 3, p. 168, 2011, doi: 10.5455/AIM.2011.19.168-171.

[24]   F. Stuart Foster *et al.*, "Principles and applications of ultrasound backscatter microscopy," *IEEE Trans Ultrason Ferroelectr Freq Control*, vol. 40, no. 5, pp. 608–617, 1993, doi: 10.1109/58.238115.

[25]   J. Flammer, M. Mozaffarieh, and H. Bebie, "The Interaction Between Light and Matter," *Basic Sciences in Ophthalmology*, pp. 21–39, 2013, doi: 10.1007/978-3-642-32261-7_2.

[26]   S. L. Jacques, "Optical properties of biological tissues: a review," *Phys Med Biol*, vol. 58, no. 11, Jun. 2013, doi: 10.1088/0031-9155/58/11/R37.

[27]   Peter Osypka, "Fiber optic endoscope," 1997

[28] M. Cutler, "Transillumination as an aid in the diagnosis of breast lesions," *Annals of Surgery*, vol. 93, no. 1, p. 223, Jan. 1931, doi: 10.1097/00000658-193101000-00032.

[29] F. F. Jöbsis, "Noninvasive, infrared monitoring of cerebral and myocardial oxygen sufficiency and circulatory parameters," *Science*, vol. 198, no. 4323, pp. 1264–1266, 1977, doi: 10.1126/SCIENCE.929199.

[30] B. Monsees, J. M. Destouet, and D. Gersell, "Light scan evaluation of nonpalpable breast lesions," *Radiology*, vol. 163, no. 2, pp. 467–470, 1987, doi: 10.1148/RADIOLOGY.163.2.3031728.

[31] G. Strangman, D. A. Boas, and J. P. Sutton, "Non-invasive neuroimaging using near-infrared light," *Biological Psychiatry*, vol. 52, no. 7, pp. 679–693, Oct. 2002, doi: 10.1016/S0006-3223(02)01550-0.

[32] B. Chance *et al.*, "Comparison of time-resolved and -unresolved measurements of deoxyhemoglobin in brain," *Proc Natl Acad Sci U S A*, vol. 85, no. 14, pp. 4971–4975, 1988, doi: 10.1073/PNAS.85.14.4971.

[33] D. A. Benaron and D. K. Stevenson, "Optical Time-of-Flight and Absorbance Imaging of Biologic Media," *Science (1979)*, vol. 259, no. 5100, pp. 1463–1466, 1993, doi: 10.1126/SCIENCE.8451643.

[34] M. A. Franceschini, V. Toronov, M. E. Filiaci, E. Gratton, and S. Fantini, "On-line optical imaging of the human brain with 160-ms temporal resolution," *Opt Express*, vol. 6, no. 3, p. 49, Jan. 2000, doi: 10.1364/OE.6.000049.

[35] H. Jiang, B. W. Pogue, M. S. Patterson, K. D. Paulsen, and U. L. Osterberg, "Simultaneous reconstruction of optical absorption and scattering maps in turbid media from near-infrared

frequency-domain data," *Optics Letters*, vol. 20, no. 20, p. 2128, Oct. 1995, doi: 10.1364/OL.20.002128.

[36] C. L. Smithpeter, A. K. Dunn, A. J. Welch, and R. Richards-Kortum, "Penetration depth limits of in vivo confocal reflectance imaging," *Applied Optics, Vol. 37, Issue 13, pp. 2749-2754*, vol. 37, no. 13, pp. 2749–2754, May 1998, doi: 10.1364/AO.37.002749.

[37] Colin J. R. Sheppard and David M. Shotton, *Confocal Laser Scanning Microscopy*. Bios Scientific Publisher Limited, 1997. Accessed: Aug. 14, 2022. [Online]. Available: https://link.springer.com/book/9789813083417

[38] A. Diaspro, P. Bianchini, G. Vicidomini, M. Faretta, P. Ramoino, and C. Usai, "Multi-photon excitation microscopy," *BioMedical Engineering Online*, vol. 5, no. 1, pp. 1–14, Jun. 2006, doi: 10.1186/1475-925X-5-36/TABLES/3.

[39] W. Denk, J. H. Strickler, and W. W. Webb, "Two-photon laser scanning fluorescence microscopy," *Science*, vol. 248, no. 4951, pp. 73–76, 1990, doi: 10.1126/SCIENCE.2321027.

[40] F. Helmchen and W. Denk, "Deep tissue two-photon microscopy," *Nat Methods*, vol. 2, no. 12, pp. 932–940, Dec. 2005, doi: 10.1038/NMETH818.

[41] J. M. Schmitt, "Optical Coherence Tomography (OCT): a review," *IEEE Journal on Selected Topics in Quantum Electronics*, vol. 5, no. 4, pp. 1205–1215, Jul. 1999, doi: 10.1109/2944.796348.

[42] B. I. Gramatikov, "Modern technologies for retinal scanning and imaging: an introduction for the biomedical engineer," *BioMedical Engineering OnLine 2014 13:1*, vol. 13, no. 1, pp. 1–35, Apr. 2014, doi: 10.1186/1475-925X-13-52.

[43] Z. Yaqoob, J. Wu, and C. Yang, "Spectral domain optical coherence tomography: a better OCT imaging strategy," *Biotechniques*, vol. 39, no. 6 Suppl, 2005, doi: 10.2144/000112090.

[44] T. E. de Carlo, A. Romano, N. K. Waheed, and J. S. Duker, "A review of optical coherence tomography angiography (OCTA)," *International Journal of Retina and Vitreous*, vol. 1, no. 1, pp. 1–15, Jul. 2015, doi: 10.1186/S40942-015-0005-8/FIGURES/14.

[45] J. G. Fujimoto, M. Wojtkowski, and R. Huber, "Fourier Domain Mode Locking (FDML): A new laser operating regime and applications for optical coherence tomography," *Optics Express, Vol. 14, Issue 8, pp. 3225-3237*, vol. 14, no. 8, pp. 3225–3237, Apr. 2006, doi: 10.1364/OE.14.003225.

[46] L. v. Wang and S. Hu, "Photoacoustic tomography: in vivo imaging from organelles to organs," *Science*, vol. 335, no. 6075, pp. 1458–1462, Mar. 2012, doi: 10.1126/SCIENCE.1216210.

[47] V. Ntziachristos, "Going deeper than microscopy: the optical imaging frontier in biology," *Nat Methods*, vol. 7, no. 8, pp. 603–614, 2010, doi: 10.1038/NMETH.1483.

[48] L. v. Wang, "Multiscale photoacoustic microscopy and computed tomography," *Nat Photonics*, vol. 3, no. 9, p. 503, Aug. 2009, doi: 10.1038/NPHOTON.2009.157.

[49] P. Beard, "Biomedical photoacoustic imaging," *Interface Focus*, vol. 1, no. 4, pp. 602–631, 2011, doi: 10.1098/RSFS.2011.0028.

[50] A. G. Bell, "On the production and reproduction of sound by light," *American Journal of Science*, vol. s3-20, no. 118, pp. 305–324, Oct. 1880, doi: 10.2475/AJS.S3-20.118.305.

[51] V. Ntziachristos, J. Ripoll, L. v. Wang, and R. Weissleder, "Looking and listening to light: the evolution of whole-body photonic imaging," *Nat Biotechnol*, vol. 23, no. 3, pp. 313–320, Mar. 2005, doi: 10.1038/NBT1074.

[52] L. v. Wang, "Tutorial on photoacoustic microscopy and computed tomography," *IEEE Journal on Selected Topics in Quantum Electronics*, vol. 14, no. 1, pp. 171–179, Jan. 2008, doi: 10.1109/JSTQE.2007.913398.

[53] V. Ntziachristos and D. Razansky, "Molecular imaging by means of multispectral optoacoustic tomography (MSOT)," *Chem Rev*, vol. 110, no. 5, pp. 2783–2794, May 2010, doi: 10.1021/CR9002566.

[54] L. v. Wang, *Photoacoustic imaging and spectroscopy*. CRC Press, 2009.

[55] A. Taruttis and V. Ntziachristos, "Advances in real-time multispectral optoacoustic imaging and its applications," *Nature Photonics 2015 9:4*, vol. 9, no. 4, pp. 219–227, Mar. 2015, doi: 10.1038/nphoton.2015.29.

[56] L. v. Wang and J. Yao, "A practical guide to photoacoustic tomography in the life sciences," *Nature Methods 2016 13:8*, vol. 13, no. 8, pp. 627–638, Jul. 2016, doi: 10.1038/nmeth.3925.

[57] S. A. Ermilov *et al.*, "Laser optoacoustic imaging system for detection of breast cancer," *J Biomed Opt*, vol. 14, no. 2, p. 024007, 2009, doi: 10.1117/1.3086616.

[58] X. L. Den-Ben, D. Razansky, and V. Ntziachristos, "The effects of acoustic attenuation in optoacoustic signals," *Physics in Medicine and Biology*, vol. 56, no. 18, pp. 6129–6148, Sep. 2011, doi: 10.1088/0031-9155/56/18/021.

[59] M. Omar, D. Soliman, J. Gateau, and V. Ntziachristos, "Ultrawideband reflection-mode optoacoustic mesoscopy," *Opt Lett*, vol. 39, no. 13, p. 3911, Jul. 2014, doi: 10.1364/OL.39.003911.

[60] A. Mandelis, "Bioacoustophotonic depth-selective imaging of turbid media and tissues: instrumentation and measurements," *Proceedings of the 6th Wseas International Conference on Signal Processing Computational Geometry Artificial Vision*, Jan. 2006,

Accessed: Aug. 16, 2022. [Online]. Available: https://www.academia.edu/75859819/Bioacoustophotonic_depth_selective_imaging_of_tu rbid_media_and_tissues_instrumentation_and_measurements

[61]   S. Telenkov, A. Mandelis, B. Lashkari, and M. Forcht, "Frequency-domain photothermoacoustics: Alternative imaging modality of biological tissues," *Journal of Applied Physics*, vol. 105, no. 10, pp. 1–8, May 2009, doi: 10.1063/1.3116136.

[62]   D. Queirós, G. Sergiadis, N. C. Deliolanis, S. Kellnberger, and V. Ntziachristos, "In vivo frequency domain optoacoustic tomography," *Optics Letters, Vol. 37, Issue 16, pp. 3423-3425*, vol. 37, no. 16, pp. 3423–3425, Aug. 2012, doi: 10.1364/OL.37.003423.

[63]   D. Razansky, C. Vinegoni, and V. Ntziachristos, "Multispectral photoacoustic imaging of fluorochromes in small animals," *Opt Lett*, vol. 32, no. 19, p. 2891, Oct. 2007, doi: 10.1364/OL.32.002891.

[64]   R. Ma, A. Taruttis, V. Ntziachristos, and D. Razansky, "Multispectral optoacoustic tomography (MSOT) scanner for whole-body small animal imaging," *Opt Express*, vol. 17, no. 24, p. 21414, Nov. 2009, doi: 10.1364/OE.17.021414.

[65]   L. v. Wang and H. Wu, *Biomedical optics : principles and imaging*. Wiley-Interscience, 2007.

[66]   L. A. Sordillo *et al.*, "Third therapeutic spectral window for deep tissue imaging," in *Proceedings Optical Biopsy XII*, Mar. 2014, vol. 8940, pp. 128–134. doi: 10.1117/12.2040604.

[67]   D. Razansky *et al.*, "Multispectral Optoacoustic Tomography of Matrix Metalloproteinase Activity in Vulnerable Human Carotid Plaques," *Molecular Imaging and Biology*, vol. 14, no. 3, p. 277, Jun. 2012, doi: 10.1007/S11307-011-0502-6.

[68] S. Tzoumas *et al.*, "Eigenspectra optoacoustic tomography achieves quantitative blood oxygenation imaging deep in tissues," *Nature Communications*, vol. 7, no. May, pp. 1–10, Jun. 2016, doi: 10.1038/ncomms12121.

[69] P. Kruizinga *et al.*, "Photoacoustic imaging of carotid artery atherosclerosis," *J Biomed Opt*, vol. 19, no. 11, p. 110504, Nov. 2014, doi: 10.1117/1.JBO.19.11.110504.

[70] T. J. Allen, A. Hall, A. P. Dhillon, J. S. Owen, and P. C. Beard, "Spectroscopic photoacoustic imaging of lipid-rich plaques in the human aorta in the 740 to 1400 nm wavelength range," *J Biomed Opt*, vol. 17, no. 6, p. 061209, 2012, doi: 10.1117/1.JBO.17.6.061209.

[71] N. C. Deliolanis *et al.*, "Deep-tissue reporter-gene imaging with fluorescence and optoacoustic tomography: a performance overview," *Mol Imaging Biol*, vol. 16, no. 5, pp. 652–660, Oct. 2014, doi: 10.1007/S11307-014-0728-1.

[72] G. S. Filonov, A. Krumholz, J. Xia, J. Yao, L. v. Wang, and V. v. Verkhusha, "Deep-Tissue Photoacoustic Tomography of a Genetically Encoded Near-Infrared Fluorescent Probe," *Angewandte Chemie International Edition*, vol. 51, no. 6, pp. 1448–1451, Feb. 2012, doi: 10.1002/ANIE.201107026.

[73] M. L. Li *et al.*, "Simultaneous molecular and hypoxia imaging of brain tumors in vivo using spectroscopic photoacoustic tomography," *Proceedings of the IEEE*, vol. 96, no. 3, pp. 481–489, 2008, doi: 10.1109/JPROC.2007.913515.

[74] N. Beziere *et al.*, "Dynamic imaging of PEGylated indocyanine green (ICG) liposomes within the tumor microenvironment using multi-spectral optoacoustic tomography (MSOT)," *Biomaterials*, vol. 37, pp. 415–424, Jan. 2015, doi: 10.1016/J.BIOMATERIALS.2014.10.014.

[75] R. A. Kruger, W. L. Kiser, D. R. Reinecke, G. A. Kruger, and K. D. Miller, "Thermoacoustic molecular imaging of small animals," *Mol Imaging*, vol. 2, no. 2, pp. 113–123, Apr. 2003, doi: 10.1162/153535003322331993.

[76] X. Wang, G. Ku, M. A. Wegiel, D. J. Bornhop, G. Stoica, and L. v. Wang, "Noninvasive photoacoustic angiography of animal brains in vivo with near-infrared light and an optical contrast agent," *Opt Lett*, vol. 29, no. 7, p. 730, Apr. 2004, doi: 10.1364/OL.29.000730.

[77] G. Ku and L. v. Wang, "Deeply penetrating photoacoustic tomography in biological tissues enhanced with an optical contrast agent," *Opt Lett*, vol. 30, no. 5, p. 507, Mar. 2005, doi: 10.1364/OL.30.000507.

[78] R. Nagaoka, T. Tabata, S. Yoshizawa, S. ichiro Umemura, and Y. Saijo, "Visualization of murine lymph vessels using photoacoustic imaging with contrast agents," *Photoacoustics*, vol. 9, pp. 39–48, Mar. 2018, doi: 10.1016/J.PACS.2018.01.001.

[79] A. de La Zerda *et al.*, "Carbon nanotubes as photoacoustic molecular imaging agents in living mice," *Nature Nanotechnology 2008 3:9*, vol. 3, no. 9, pp. 557–562, Aug. 2008, doi: 10.1038/nnano.2008.231.

[80] H. Aoki, M. Nojiri, R. Mukai, and S. Ito, "Near-infrared absorbing polymer nano-particle as a sensitive contrast agent for photo-acoustic imaging," *Nanoscale*, vol. 7, no. 1, pp. 337–343, Dec. 2014, doi: 10.1039/C4NR04724A.

[81] J. v. Jokerst, D. van de Sompel, S. E. Bohndiek, and S. S. Gambhir, "Cellulose Nanoparticles are a Biodegradable Photoacoustic Contrast Agent for Use in Living Mice," *Photoacoustics*, vol. 2, no. 3, pp. 119–127, 2014, doi: 10.1016/J.PACS.2014.07.001.

[82] A. Taruttis, D. Razansky, E. Herzog, and V. Ntziachristos, "Real-time imaging of cardiovascular dynamics and circulating gold nanorods with multispectral optoacoustic

tomography," *Optics Express, Vol. 18, Issue 19, pp. 19592-19602*, vol. 18, no. 19, pp. 19592–19602, Sep. 2010, doi: 10.1364/OE.18.019592.

[83]   J. v. Jokerst, A. J. Cole, D. van de Sompel, and S. S. Gambhir, "Gold nanorods for ovarian cancer detection with photoacoustic imaging and resection guidance via Raman imaging in living mice," *ACS Nano*, vol. 6, no. 11, pp. 10366–10377, Nov. 2012, doi: 10.1021/NN304347G.

[84]   S. Tzoumas, A. Nunes, N. C. Deliolanis, and V. Ntziachristos, "Effects of multispectral excitation on the sensitivity of molecular optoacoustic imaging," *Journal of Biophotonics*, vol. 8, no. 8, pp. 629–637, Aug. 2015, doi: 10.1002/JBIO.201400056.

[85]   J. Xia and L. v. Wang, "Small-animal whole-body photoacoustic tomography: a review," *IEEE Trans Biomed Eng*, vol. 61, no. 5, p. 1380, 2014, doi: 10.1109/TBME.2013.2283507.

[86]   D. Razansky, A. Buehler, and V. Ntziachristos, "Volumetric real-time multispectral optoacoustic tomography of biomarkers," *Nature Protocols*, vol. 6, no. 8, pp. 1121–1129, Jul. 2011, doi: 10.1038/nprot.2011.351.

[87]   A. Dima, N. C. Burton, and V. Ntziachristos, "Multispectral optoacoustic tomography at 64, 128, and 256 channels," *Journal of Biomedical Optics*, vol. 19, no. 3, p. 036021, Mar. 2014, doi: 10.1117/1.jbo.19.3.036021.

[88]   I. Stoffels *et al.*, "Metastatic status of sentinel lymph nodes in melanoma determined noninvasively with multispectral optoacoustic imaging," *Sci Transl Med*, vol. 7, no. 317, Dec. 2015, doi: 10.1126/SCITRANSLMED.AAD1278.

[89]   K. S. Valluru and J. K. Willmann, "Clinical photoacoustic imaging of cancer," *Ultrasonography*, vol. 35, no. 4, pp. 267–280, Oct. 2016, doi: 10.14366/USG.16035.

[90]   K. S. Valluru, K. E. Wilson, and J. K. Willmann, "Photoacoustic Imaging in Oncology: Translational Preclinical and Early Clinical Experience," *Radiology*, vol. 280, no. 2, pp. 332–349, Aug. 2016, doi: 10.1148/RADIOL.16151414.

[91]   A. Garcia-Uribe *et al.*, "Dual-Modality Photoacoustic and Ultrasound Imaging System for Noninvasive Sentinel Lymph Node Detection in Patients with Breast Cancer," *Sci Rep*, vol. 5, Oct. 2015, doi: 10.1038/SREP15748.

[92]   F. Knieling *et al.*, "Multispectral Optoacoustic Tomography for Assessment of Crohn's Disease Activity," *N Engl J Med*, vol. 376, no. 13, pp. 1292–1294, Mar. 2017, doi: 10.1056/NEJMC1612455.

[93]   J. Jo *et al.*, "A Functional Study of Human Inflammatory Arthritis Using Photoacoustic Imaging," *Scientific Reports 2017 7:1*, vol. 7, no. 1, pp. 1–9, Nov. 2017, doi: 10.1038/s41598-017-15147-5.

[94]   J. Reber *et al.*, "Non-invasive Measurement of Brown Fat Metabolism Based on Optoacoustic Imaging of Hemoglobin Gradients," *Cell Metab*, vol. 27, no. 3, pp. 689-701.e4, Mar. 2018, doi: 10.1016/J.CMET.2018.02.002.

[95]   A. Chekkoury *et al.*, "High-Resolution Multispectral Optoacoustic Tomography of the Vascularization and Constitutive Hypoxemia of Cancerous Tumors," *Neoplasia*, vol. 18, no. 8, pp. 459–467, Aug. 2016, doi: 10.1016/J.NEO.2016.06.004.

[96]   A. Taruttis, A. C. Timmermans, P. C. Wouters, M. Kacprowicz, G. M. van Dam, and V. Ntziachristos, "Optoacoustic Imaging of Human Vasculature: Feasibility by Using a Handheld Probe," *Radiology*, vol. 000, no. 0, p. 152160, Oct. 2016, doi: 10.1148/radiol.2016152160.

[97] M. Toi *et al.*, "Visualization of tumor-related blood vessels in human breast by photoacoustic imaging system with a hemispherical detector array," *Scientific Reports 2017 7:1*, vol. 7, no. 1, pp. 1–11, Feb. 2017, doi: 10.1038/srep41970.

[98] C. Li and L. v Wang, "Photoacoustic tomography and sensing in biomedicine.," *Phys Med Biol*, vol. 54, no. 19, pp. R59-97, Oct. 2009, doi: 10.1088/0031-9155/54/19/R01.

[99] Vasilis. Ntziachristos, Anne. Leroy-Willig, and Bertrand. Tavitian, *Textbook of in vivo imaging in vertebrates*. J. Wiley, 2007.

[100] D. Razansky and V. Ntziachristos, "Hybrid photoacoustic fluorescence molecular tomography using finite-element-based inversion," *Med Phys*, vol. 34, no. 11, pp. 4293–4301, 2007, doi: 10.1118/1.2786866.

[101] Bjorn. Angelsen, *Ultrasound imaging : waves, signals, and signal processing*. Trondheim: Emantec, 2000.

[102] A. G. Bell, "The Production of Sound by Radiant Energy," *Science (1979)*, vol. os-2, no. 48, pp. 242–253, May 1881, doi: 10.1126/SCIENCE.OS-2.48.242.

[103] D. Razansky, "Multispectral optoacoustic tomography-volumetric color hearing in real time," *IEEE Journal on Selected Topics in Quantum Electronics*, vol. 18, no. 3, pp. 1234–1243, 2012, doi: 10.1109/JSTQE.2011.2172192.

[104] M. Ángel Araque Caballero, "Optoacoustic Imaging with Full-Knowledge of Sensor Properties, PhD Thesis," Technical University of Munich, 2012.

[105] C. G. A. Hoelen and F. F. M. de Mul, "A new theoretical approach to photoacoustic signal generation," *J Acoust Soc Am*, vol. 106, no. 2, p. 695, Jul. 1999, doi: 10.1121/1.427087.

[106] D. Razansky, J. Baeten, and V. Ntziachristos, "Sensitivity of molecular target detection by multispectral optoacoustic tomography (MSOT)," *Med Phys*, vol. 36, no. 3, pp. 939–945, 2009, doi: 10.1118/1.3077120.

[107] R. Paschotta, *Encyclopedia of Laser Physics and Technology*. Weinheim: Wiley-VCH Verlag GmbH, 2001.

[108] T. L. Szabo, *Diagnostic Ultrasound Imaging: Inside Out*. Elsevier Inc., 2004. doi: 10.1016/C2011-0-07261-7.

[109] K. K. Shung and M. J. Zipparo, "Ultrasonic transducers and arrays," *IEEE Engineering in Medicine and Biology Magazine*, vol. 15, no. 6, pp. 20–30, Nov. 1996, doi: 10.1109/51.544509.

[110] R. Nuster *et al.*, "Full field detection in photoacoustic tomography," *Optics Express, Vol. 18, Issue 6, pp. 6288-6299*, vol. 18, no. 6, pp. 6288–6299, Mar. 2010, doi: 10.1364/OE.18.006288.

[111] A. Rosenthal, D. Razansky, and V. Ntziachristos, "High-sensitivity compact ultrasonic detector based on a pi-phase-shifted fiber Bragg grating," *Optics Letters, Vol. 36, Issue 10, pp. 1833-1835*, vol. 36, no. 10, pp. 1833–1835, May 2011, doi: 10.1364/OL.36.001833.

[112] E. Z. Zhang, J. G. Laufer, R. B. Pedley, and P. C. Beard, "In vivo high-resolution 3D photoacoustic imaging of superficial vascular anatomy," *Phys Med Biol*, vol. 54, no. 4, pp. 1035–1046, 2009, doi: 10.1088/0031-9155/54/4/014.

[113] V. Kozhushko, T. Khokhlova, A. Zharinov, I. Pelivanov, V. Solomatin, and A. Karabutov, "Focused array transducer for two-dimensional optoacoustic tomography," *J Acoust Soc Am*, vol. 116, no. 3, pp. 1498–1506, Sep. 2004, doi: 10.1121/1.1781710.

[114] A. Rosenthal, V. Ntziachristos, and D. Razansky, "Optoacoustic methods for frequency calibration of ultrasonic sensors," *IEEE Trans Ultrason Ferroelectr Freq Control*, vol. 58, no. 2, pp. 316–326, Feb. 2011, doi: 10.1109/TUFFC.2011.1809.

[115] T. D. Khokhlova, I. M. Pelivanov, V. v. Kozhushko, A. N. Zharinov, V. S. Solomatin, and A. A. Karabutov, "Optoacoustic imaging of absorbing objects in a turbid medium: ultimate sensitivity and application to breast cancer diagnostics," *Appl Opt*, vol. 46, no. 2, pp. 262–272, Jan. 2007, doi: 10.1364/AO.46.000262.

[116] A. Rosenthal, D. Razansky, and V. Ntziachristos, "Fast semi-analytical model-based acoustic inversion for quantitative optoacoustic tomography," *IEEE Transactions on Medical Imaging*, vol. 29, no. 6, pp. 1275–1285, 2010, doi: 10.1109/TMI.2010.2044584.

[117] A. Rosenthal, V. Ntziachristos, and D. Razansky, "Model-based optoacoustic inversion with arbitrary-shape detectors," *Medical Physics*, vol. 38, no. 7, pp. 4285–4295, 2011, doi: 10.1118/1.3589141.

[118] Jφ. A. Jensen and N. B. Svendsen, "Calculation of Pressure Fields from Arbitrarily Shaped, Apodized, and Excited Ultrasound Transducers," *IEEE Transactions on Ultrasonics, Ferroelectrics, and Frequency Control*, vol. 39, no. 2, pp. 262–267, 1992, doi: 10.1109/58.139123.

[119] H. F. Zhang, K. Maslov, M.-L. Li, G. Stoica, and L. v. Wang, "In vivo volumetric imaging of subcutaneous microvasculature by photoacoustic microscopy," *Opt Express*, vol. 14, no. 20, p. 9317, Oct. 2006, doi: 10.1364/OE.14.009317.

[120] K. Maslov, G. Stoica, and L. v. Wang, "In vivo dark-field reflection-mode photoacoustic microscopy," *Opt Lett*, vol. 30, no. 6, p. 625, Mar. 2005, doi: 10.1364/OL.30.000625.

[121] H.-P. Brecht, R. Su, M. Fronheiser, S. A. Ermilov, A. Conjusteau, and A. A. Oraevsky, "Whole-body three-dimensional optoacoustic tomography system for small animals," *J Biomed Opt*, vol. 14, no. 6, p. 064007, 2009, doi: 10.1117/1.3259361.

[122] J. Laufer *et al.*, "In vivo photoacoustic imaging of mouse embryos," *J Biomed Opt*, vol. 17, no. 6, p. 061220, 2012, doi: 10.1117/1.JBO.17.6.061220.

[123] M. Xu and L. v. Wang, "Photoacoustic imaging in biomedicine," *Review of Scientific Instruments*, vol. 77, no. 4, p. 041101, Apr. 2006, doi: 10.1063/1.2195024.

[124] K. P. Köstli, M. Frenz, H. Bebie, and H. P. Weber, "Temporal backward projection of optoacoustic pressure transients using fourier transform methods," *Phys Med Biol*, vol. 46, no. 7, pp. 1863–1872, 2001, doi: 10.1088/0031-9155/46/7/309.

[125] M. Xu and L. v. Wang, "Universal back-projection algorithm for photoacoustic computed tomography," *Phys Rev E Stat Nonlin Soft Matter Phys*, vol. 71, no. 1 Pt 2, Jan. 2005, doi: 10.1103/PHYSREVE.71.016706.

[126] H. Jiang, Z. Yuan, and X. Gu, "Spatially varying optical and acoustic property reconstruction using finite-element-based photoacoustic tomography," *Journal of the Optical Society of America A*, vol. 23, no. 4, p. 878, Apr. 2006, doi: 10.1364/JOSAA.23.000878.

[127] G. Paltauf, J. A. Viator, S. A. Prahl, and S. L. Jacques, "Iterative reconstruction algorithm for optoacoustic imaging," *J Acoust Soc Am*, vol. 112, no. 4, p. 1536, Sep. 2002, doi: 10.1121/1.1501898.

[128] X. Wang, Y. Xu, M. Xu, S. Yokoo, E. S. Fry, and L. v. Wang, "Photoacoustic tomography of biological tissues with high cross-section resolution: reconstruction and experiment," *Med Phys*, vol. 29, no. 12, pp. 2799–2805, Dec. 2002, doi: 10.1118/1.1521720.

[129] G. H. Golub and C. F. Van Loan, *Matrix Computations*. John Hopkins University Press, 1996.

[130] C. C. Paige and M. A. Saunders, "LSQR: An Algorithm for Sparse Linear Equations and Sparse Least Squares," *ACM Transactions on Mathematical Software (TOMS)*, vol. 8, no. 1, pp. 43–71, Mar. 1982, doi: 10.1145/355984.355989.

[131] M. Xu and L. v. Wang, "Analytic explanation of spatial resolution related to bandwidth and detector aperture size in thermoacoustic or photoacoustic reconstruction," *Phys Rev E Stat Nonlin Soft Matter Phys*, vol. 67, no. 5 Pt 2, p. 15, 2003, doi: 10.1103/PHYSREVE.67.056605.

[132] J. A. Jensen, "Field: A Program for Simulating Ultrasound Systems," *Medical & Biological Engineering & Computing*, vol. 34, no. sup. 1, pp. 351–353, 1997, doi: 10.2/JQUERY.MIN.JS.

[133] T. D. Khokhlova, I. M. Pelivanov, and A. A. Karabutov, "Optoacoustic tomography utilizing focused transducers: The resolution study," *Applied Physics Letters*, vol. 92, no. 2, p. 024105, Jan. 2008, doi: 10.1063/1.2834855.

[134] Y. Xu, L. v. Wang, G. Ambartsoumian, and P. Kuchment, "Reconstructions in limited-view thermoacoustic tomography," *Med Phys*, vol. 31, no. 4, pp. 724–733, 2004, doi: 10.1118/1.1644531.

[135] B. E. Treeby and B. T. Cox, "k-Wave: MATLAB toolbox for the simulation and reconstruction of photoacoustic wave fields," *J Biomed Opt*, vol. 15, no. 2, p. 021314, 2010, doi: 10.1117/1.3360308.

[136] A. Buehler, A. Rosenthal, T. Jetzfellner, A. Dima, D. Razansky, and V. Ntziachristos, "Model-based optoacoustic inversions with incomplete projection data," *Med Phys*, vol. 38, no. 3, pp. 1694–1704, 2011, doi: 10.1118/1.3556916.

[137] P. C. Hansen, "Truncated Singular Value Decomposition Solutions to Discrete Ill-Posed Problems with Ill-Determined Numerical Rank," *SIAM J. Sci. Stat. Comput*, vol. 11, no. 3, pp. 503–518, 1990, doi: 10.1137/0911028.

[138] C. Hansen, C. Brezinski, and M. Redivo Zaglia, "REGULARIZATION TOOLS: A Matlab package for analysis and solution of discrete ill-posed problems," *Numerical Algorithms*, vol. 6, no. 1, pp. 1–35, Mar. 1994, doi: 10.1007/BF02149761.

[139] P. C. Hansen, "Regularization, GSVD and truncated GSVD," *BIT Numerical Mathematics*, vol. 29, no. 3, pp. 491–504, Sep. 1989, doi: 10.1007/BF02219234.

[140] S. Morigi, L. Reichel, and F. Sgallari, "A truncated projected SVD method for linear discrete ill-posed problems," *Numerical Algorithms*, vol. 43, no. 3, pp. 197–213, Jan. 2007, doi: 10.1007/S11075-006-9053-3.

[141] P. C. Hansen, "Rank-Deficient and Discrete Ill-Posed Problems," *SIAM*, 1998, doi: 10.1137/1.9780898719697.

[142] P. C. Hansen, "Regularization Tools version 4.0 for Matlab 7.3," *Numerical Algorithms*, vol. 46, no. 2, pp. 189–194, Nov. 2007, doi: 10.1007/S11075-007-9136-9.

[143] D. Razansky *et al.*, "Multispectral opto-acoustic tomography of deep-seated fluorescent proteins in vivo," *Nature Photonics*, vol. 3, no. 7, pp. 412–417, Jul. 2009, doi: 10.1038/nphoton.2009.98.

[144] R. A. Kruger, P. Liu, Y. "Richard" Fang, and C. R. Appledorn, "Photoacoustic ultrasound (PAUS)-Reconstruction tomography," *Medical Physics*, vol. 22, no. 10, pp. 1605–1609, Oct. 1995, doi: 10.1118/1.597429.

[145] K. P. Köstli, D. Frauchiger, J. J. Niederhauser, G. Paltauf, H. P. Weber, and M. Frenz, "Optoacoustic imaging using a three-dimensional reconstruction algorithm," *IEEE Journal on Selected Topics in Quantum Electronics*, vol. 7, no. 6, pp. 918–923, Nov. 2001, doi: 10.1109/2944.983294.

[146] S. J. Norton and T. Vo-Dinh, "Optoacoustic diffraction tomography: analysis of algorithms," *J Opt Soc Am A Opt Image Sci Vis*, vol. 20, no. 10, p. 1859, Oct. 2003, doi: 10.1364/JOSAA.20.001859.

[147] Y. Xu and L. v. Wang, "Time Reversal and Its Application to Tomography with Diffracting Sources," *Physical Review Letters*, vol. 92, no. 3, p. 033902, Jan. 2004, doi: 10.1103/PhysRevLett.92.033902.

[148] J. F. Greenleaf, S. A. Johnson, S. L. Lee, G. T. Herman, and E. H. Wood, "Algebraic reconstruction of spatial distributions of acoustic absorption within tissue from their two-dimensional acoustic projections," *Acoust. Holography*, pp. 591–603, 1974, doi: 10.1007/978-1-4757-0827-1_34/COVER.

[149] A. C. Kak and M. Slaney, *Principles of Computerized Tomographic Imaging*. Society for Industrial and Applied Mathematics, 1999. doi: 10.1137/1.9780898719277.

[150] R. Snieder and D. F. Aldridge, "Perturbation theory for travel times," *J Acoust Soc Am*, vol. 98, no. 3, p. 1565, Jun. 1998, doi: 10.1121/1.413422.

[151] J. D. N. Cheeke, *Fundamentals and applications of ultrasonic waves*. CRC Press, 2002.

[152] Y. Xu and L. v. Wang, "Effects of acoustic heterogeneity in breast thermoacoustic tomography," *IEEE Trans Ultrason Ferroelectr Freq Control*, vol. 50, no. 9, pp. 1134–1146, Sep. 2003, doi: 10.1109/TUFFC.2003.1235325.

[153] X. Jin and L. v. Wang, "Thermoacoustic tomography with correction for acoustic speed variations," *Phys Med Biol*, vol. 51, no. 24, pp. 6437–6448, Dec. 2006, doi: 10.1088/0031-9155/51/24/010.

[154] C. Zhang and Y. Wang, "A reconstruction algorithm for thermoacoustic tomography with compensation for acoustic speed heterogeneity," *Phys Med Biol*, vol. 53, no. 18, pp. 4971–4982, Sep. 2008, doi: 10.1088/0031-9155/53/18/008.

[155] D. Modgil, M. A. Anastasio, and P. J. la Rivière, "Image reconstruction in photoacoustic tomography with variable speed of sound using a higher-order geometrical acoustics approximation," *Journal of Biomedical Optics*, vol. 15, no. 2, p. 021308, 2010, doi: 10.1117/1.3333550.

[156] Z. Yuan, Q. Zhang, and H. Jiang, "Simultaneous reconstruction of acoustic and optical properties of heterogeneous media by quantitative photoacoustic tomography," *Opt Express*, vol. 14, no. 15, p. 6749, 2006, doi: 10.1364/OE.14.006749.

[157] X. Jin, C. Li, and L. v. Wang, "Effects of acoustic heterogeneities on transcranial brain imaging with microwave-induced thermoacoustic tomography," *Medical Physics*, vol. 35, no. 7Part1, pp. 3205–3214, Jun. 2008, doi: 10.1118/1.2938731.

[158] X. L. Deán-Ben, R. Ma, D. Razansky, and V. Ntziachristos, "Statistical approach for optoacoustic image reconstruction in the presence of strong acoustic heterogeneities," *IEEE Transactions on Medical Imaging*, vol. 30, no. 2, pp. 401–408, Feb. 2011, doi: 10.1109/TMI.2010.2081683.

[159] X. L. Deán-Ben, V. Ntziachristos, and D. Razansky, "Statistical optoacoustic image reconstruction using a-priori knowledge on the location of acoustic distortions," *Applied Physics Letters*, vol. 98, no. 17, p. 171110, 2011, doi: 10.1063/1.3564905.

[160] X. L. Deán-Ben, R. Ma, A. Rosenthal, V. Ntziachristos, and D. Razansky, "Weighted model-based optoacoustic reconstruction in acoustic scattering media," *Physics in Medicine and Biology*, vol. 58, no. 16, pp. 5555–5566, Aug. 2013, doi: 10.1088/0031-9155/58/16/5555.

[161] M. Muhammad, J. Prakash, E. Liapis, V. Ntziachristos, and D. Jüstel, "Weighted model-based optoacoustic reconstruction for partial-view geometries," *Journal of Biophotonics*, vol. 15, no. 6, p. e202100334, Jun. 2022, doi: 10.1002/JBIO.202100334.

[162] R. Ma *et al.*, "Multispectral optoacoustic tomography (MSOT) scanner for whole-body small animal imaging," *Optics Express, Vol. 17, Issue 24, pp. 21414-21426*, vol. 17, no. 24, pp. 21414–21426, Nov. 2009, doi: 10.1364/OE.17.021414.

[163] B. T. Cox and B. E. Treeby, "Artifact trapping during time reversal photoacoustic imaging for acoustically heterogeneous media," *IEEE Transactions on Medical Imaging*, vol. 29, no. 2, pp. 387–396, Feb. 2010, doi: 10.1109/TMI.2009.2032358.

[164] J. Provost and F. Lesage, "The application of compressed sensing for photo-acoustic tomography," *IEEE Transactions on Medical Imaging*, vol. 28, no. 4, pp. 585–594, Apr. 2009, doi: 10.1109/TMI.2008.2007825.

[165] X. L. L. Deán-ben, V. Ntziachristos, and D. Razansky, "Acceleration of optoacoustic model-based reconstruction using angular image discretization," *IEEE Transactions on Medical Imaging*, vol. 31, no. 5, pp. 1154–1162, 2012, doi: 10.1109/TMI.2012.2187460.

[166] M. A. Anastasio, J. Zhang, X. Pan, Y. Zou, G. Ku, and L. v. Wang, "Half-Time Image Reconstruction in Thermoacoustic Tomography," *IEEE Transactions on Medical Imaging*, vol. 24, no. 2, pp. 199–210, 2005, doi: 10.1109/TMI.2004.839682.

[167] A. Dima, N. C. Burton, and V. Ntziachristos, "Multispectral optoacoustic tomography at 64, 128, and 256 channels," *Journal of Biomedical Optics*, vol. 19, no. 3, p. 036021, 2014, doi: 10.1117/1.jbo.19.3.036021.

[168] S. L. Jacques, "Optical properties of biological tissues: A review," *Physics in Medicine and Biology*, vol. 58, no. 11, pp. 37–61, 2013, doi: 10.1088/0031-9155/58/11/R37.

[169] P. Di Ninni, F. Martelli, and G. Zaccanti, "The use of India ink in tissue-simulating phantoms," *Optics Express*, vol. 18, no. 26, pp. 26854–26865, Dec. 2010, doi: 10.1364/OE.18.026854.

[170] P. Lai, X. Xu, and L. V Wang, "Dependence of optical scattering from Intralipid in gelatin-gel based tissue-mimicking phantoms on mixing temperature and time," *Journal of Biomedical Optics*, vol. 19, no. 3, p. 035002, Mar. 2014, doi: 10.1117/1.JBO.19.3.035002.

[171] T. D. Paustian and R. S. Kurtz, "Transposon mutagenesis of Rhodobacter sphaeroides.," in *Proc. 15th Work. Assoc. Biol. Lab. Educ. 15*, 1994, pp. 45–61.

[172] J. F. Imhoff, H. G. Trüper, and N. Pfennig, "Rearrangement of the Species and Genera of the Phototrophic 'Purple Nonsulfur Bacteria,'" *International Journal of Systematic Bacteriology*, vol. 34, no. 3, pp. 340–343, 1984, doi: 10.1099/00207713-34-3-340.

[173] I. Olefir, E. Mercep, N. C. Burton, S. V. Ovsepian, and V. Ntziachristos, "Hybrid multispectral optoacoustic and ultrasound tomography for morphological and physiological brain imaging," *Journal of Biomedical Optics*, vol. 21, no. 8, p. 086005, 2016, doi: 10.1117/1.jbo.21.8.086005.

[174] F. Timischl, "The contrast-to-noise ratio for image quality evaluation in scanning electron microscopy," *Scanning*, vol. 37, no. 1, pp. 54–62, Jan. 2015, doi: 10.1002/SCA.21179.

[175] E. Herzog, A. Taruttis, N. Beziere, A. A. Lutich, D. Razansky, and V. Ntziachristos, "Optical Imaging of Cancer Heterogeneity with Multispectral Optoacoustic Tomography," *Radiology*, vol. 263, no. 2, pp. 461–468, May 2012, doi: 10.1148/radiol.11111646.

[176] S. Tzoumas, N. Deliolanis, S. Morscher, and V. Ntziachristos, "Un-mixing Molecular Agents from Absorbing Tissue in Multispectral Optoacoustic Tomography.," *IEEE Trans Med Imaging*, vol. 33, no. 1, pp. 48–60, 2013, doi: 10.1109/TMI.2013.2279994.

[177] B. E. Treeby, T. K. Varslot, E. Z. Zhang, J. G. Laufer, and P. C. Beard, "Automatic sound speed selection in photoacoustic image reconstruction using an autofocus approach," *Journal of Biomedical Optics*, vol. 16, no. 9, p. 090501, Sep. 2011, doi: 10.1117/1.3619139.

[178] E. Merčep, G. Jeng, S. Morscher, P. C. Li, and D. Razansky, *Hybrid Optoacoustic Tomography and Pulse–Echo Ultrasonography Using Concave Arrays*, vol. 62, no. 9. 2015. doi: 10.1109/TUFFC.2015.007058.

[179] J. Prakash, S. Mandal, D. Razansky, and V. Ntziachristos, "Maximum entropy based non-negative optoacoustic tomographic image reconstruction," *IEEE Transactions on Biomedical Engineering*, pp. 1–1, 2019, doi: 10.1109/TBME.2019.2892842.

[180] L. Ding, X. Luís Deán-Ben, C. Lutzweiler, D. Razansky, and V. Ntziachristos, "Efficient non-negative constrained model-based inversion in optoacoustic tomography," *Physics in Medicine and Biology*, vol. 60, no. 17, pp. 6733–6750, Sep. 2015, doi: 10.1088/0031-9155/60/17/6733.